Evolution of clusters and large-scale structures of galaxies

Chervin F. P. Laporte

München 2014

Evolution of clusters and large-scale structures of galaxies

Chervin F. P. Laporte

Dissertation
an der Fakultät für Physik
der Ludwig–Maximilians–Universität
München

vorgelegt von
Chervin F. P. Laporte
aus Versailles, Yvelines, France

München, den 28. Februar 2014

Erstgutachter: Prof. Dr. Simon D. M. White
Zweitgutachter: Prof. Dr. Andreas Burkert
Tag der mündlichen Prüfung: 28. April 2014

Contents

Zusammenfassung **xiii**

I Overview **1**

1 Background Cosmology & Structure Formation **5**
- 1.1 Background Friedman Robertson-Walker Cosmology 5
  - 1.1.1 Inflation 8
- 1.2 A word on thermal history of the Universe 9
- 1.3 Growth of Structure in the linear regime and the large-scale structures . . 9
  - 1.3.1 Collisional fluid 10
- 1.4 Growth of matter and dark matter perturbations after recombination . . . 12
  - 1.4.1 Primordial Power spectrum and its relation to the Post-recombination one 12

2 Dark Matter **17**
- 2.1 Observational evidence 17
  - 2.1.1 Galactic scales 17
  - 2.1.2 Galaxy Cluster scales 18
  - 2.1.3 Cosmological scales 18
  - 2.1.4 Collisionless Cold Dark matter 19
- 2.2 Dark matter as a particle 20
  - 2.2.1 WIMPs 20
  - 2.2.2 axions 21

3 Collisionless systems and the N-body method **23**
- 3.1 Dynamics of collisionless systems 23
- 3.2 N-body method 23
- 3.3 Force calculation and algorithms 24
  - 3.3.1 Particle mesh method 24
  - 3.3.2 Tree method 25
  - 3.3.3 TreePM method 26
- 3.4 Cosmological Simulations 26
- 3.5 Initial Conditions 26

3.5.1 The Zel'dovich Approximation 27
3.5.2 Use in cosmological N-body simulations 28
3.6 The State of the Art 28

II Brightest Cluster Galaxies and the distribution of dark matter in galaxy 31

4 Shallow Dark Matter Cusps in Galaxy Clusters 33
4.1 abstract 33
4.2 Introduction 33
4.3 Numerical Methods 35
4.3.1 Simulation 35
4.3.2 Weighting Scheme 36
4.3.3 Results for the BCG evolution 40
4.4 Evolution of the dark matter slope 42
4.4.1 Methodology 42
4.4.2 Results for the original RS09 simulations 42
4.4.3 Dark matter slope evolution for other BCG stellar mass profiles . . 44
4.5 Conclusions 46

5 The Growth in Size and Mass of Cluster Galaxies 49
5.1 Introduction 49
5.2 Methods 51
5.2.1 Simulations 51
5.2.2 A Weighting scheme for cosmological dark matter simulations . . . 52
5.2.3 Initial Conditions 53
5.3 Structural Properties of BCGs 55
5.3.1 Surface Brightness and Density Profiles 55
5.4 Evolution of BCGs and Ellipticals in Clusters 58
5.5 Discussion 63
5.6 Conclusions 66

6 Dark Matter and Stars in Galaxy Clusters 67
6.1 Introduction 68
6.2 Numerical methods 69
6.2.1 Simulations 69
6.2.2 Generating the stellar components and compound galaxies 70
6.2.3 Stability Tests 70
6.2.4 Initial conditions 71
6.2.5 Cluster simulations 76
6.3 Structure of galaxy clusters 76
6.3.1 Density profiles 76

6.4 Mergers, mass re-shuffling & dark matter heating 79
6.5 On the contribution of super-massive black-holes 81
6.6 Discussion 83
6.7 Conclusion 85

7 Mass profile slopes for dSphs 87
7.1 Introduction 87
7.2 Numerical Methods 89
  7.2.1 Dark matter haloes 89
  7.2.2 Generating Tracers 89
7.3 Mass modelling: multi-component method 90
  7.3.1 The bias in the WP mass-estimator: systematics 90
  7.3.2 Why triaxality does not matter so much? 92
7.4 Discussion and conclusions 95

Danksagung 105

List of Figures

1.1 CMB Planck 2013 Map 6
1.2 Large Scale Structures: 2FGRS 6
1.3 Thermal History of Universe 14
1.4 Transfer Functions 15

2.1 Temperature Power Spectrum as measured by Planck 2013 19
2.2 Cold Dark Matter vs. Hot Dark Matter & the CfA survey 20
2.3 The Bullet Cluster 22

3.1 Barnes & Hut 1983: Oct-Tree illustration 25
3.2 Cosmological N-body simulations: The *Millennium* run 29

4.1 Differential energy distributions for rescaled galaxies 37
4.2 Density profiles of rescaled galaxies 38
4.3 Normalised radial stellar mass distribution in BCG at $z = 0$ 43
4.4 Total and dark matter slopes for original runs and rescaled versions. 45

5.1 Triaxial tracer weighting scheme: example density profile 53
5.2 Triaxial tracer weighting scheme: stability test 54
5.3 Stellar-to-halo mass relations at $z = 2$ and $z = 0$: BCGs and cluster ellipticals 56
5.4 $z = 0$ surface brightness profiles of BCGs 57
5.5 $z = 1$ surface brightness profiles of BCGs 59
5.6 Stellar density profiles of BCGs: in-situ, accreted and total 60
5.7 BCG cluster mass evolution: $z = 1$, $z = 0.3$ and $z = 0$ 62
5.8 Mass-size evolution for cluster galaxies: $z = 2$, $z = 1$, $z = 0.3$ and $z = 0$ . . 64

6.1 Stability test: stellar density profile evolution 72
6.2 Stability test: stellar, dark and total density profile 73
6.3 Stability test: x-y projection of stars 74
6.4 The $z = 2$ mass-size relation 75
6.5 Distribution of central $z = 0$ 10 kpc DM particles at $z = 2$ 77
6.6 Final density profiles for stars, dark matter and total matter. 78
6.7 Slopes of the density profiles for stars, dark matter and total matter 80

7.1 Projected number density and L.O.S.V.D profiles for dSph host subhalo . . 91
7.2 Stacked bias distribution of DM slope inferences: correct method 93
7.3 Stacked bias distribution of DM slope inferences: incorrect method 94
7.4 Effect of triaxality: variations in R_e, σ and $M(r_e)$ 96

List of Tables

4.1 Rescaled simulations: size and stellar mass growth factors 42

5.1 BCG stellar mass accretion 63
5.2 BCG merger counts 65

6.1 Phoenix Clusters Properties 76
6.2 Black hole masses and mass deficits 83

Zusammenfassung

Diese Doktorarbeit befasst sich mit der Bildung und Entwicklung der Hellsten Haufengalaxien (Brightest Cluster Galaxies, BCGs) und mit der zentralen Verteilung von Dunkler Materie (DM) in Galaxienhaufen in kosmologischen N-Körper Simulationen im Rahmen des ΛCDM Paradigmas. Dabei werden folgende Fragen behandelt: Wachsen BCGs durch dissipationsfreie Merger innerhalb der letzten 10 Gigajahre? Wenn ja, was sind ihre strukturellen Eigenschaften? Sind die vorhergesagten Massenwachstumsraten der BCGs in den letzten 10 Gigajahren in Übereinstimmung mit Beobachtungen? Welche Bedeutung hat die dissipationsfreie Bildung von BCGs für die zentrale Verteilung der DM in Galaxienhaufen? Legen die Beobachtungsdaten der Verteilung der DM in Galaxienhaufen tatsächlich nahe, dass die Vorstellung der DM als kalt und kollisionsfrei überdacht werden muss?

Die ersten drei Kapitel dieser Arbeit geben einen Überblick über Kosmologie, Strukturbildung, die Natur der Dunklen Materie und über numerische Techniken in kosmologischen N-Körper Simulationen.

In Kapitel 4 wird anhand eines Sets von kosmologischen N-Körper Simulationen und mehreren reskalierten Versionen dieser Simulationen untersucht, wie sich zentral schwach konzentrierte Verteilungen von Dunkler Materie (shallow DM cusps) durch dissipationsfreie Verschmelzungen von Galaxien (Merger) bilden können. Es wird die Abhängigkeit der Mischung von DM und Sternen im Zentrum der Haufen zu späteren Zeiten von der ursprünglichen stellaren Struktur untersucht. Es stellt sich heraus, dass qualitativ flache DM cusps im Zentrum von Galaxienhaufen natürlicherweise zu erwarten sind, falls die Bildung der BCGs in erster Linie durch dissipationsfreie Merger abläuft.

In Kapitel 5 wird ein allgemeines Gewichtungsschema entwickelt, um Gleichgewichtsverteilungsfunktionen der Form $f(E)$ in triaxialen Potentialen zu generieren. Dieses Schema wird auf eine Reihe von neun hochaufgelösten DM Simulationen zur Halobildung von Haufengalaxien angewendet, um die Zusammensetzung von BCGs und von elliptischen Haufen zu verfolgen. Dafür werden die neuesten, durch Beobachtungen gewonnenen Beschränkungen für galaktische Strukturen sowie für die Relationen zwischen Sternen und DM verwendet. Es wird gezeigt, dass dissipationsfreie Merger in ΛCDM in Übereinstimmung mit Beobachtungen stellare Massenzusammensetzungen von BCGs mit Wachstumsraten von ~ 2.1 im Bereich $0.3 < z < 1.0$ und von ~ 1.4 im Bereich $0.0 < z < 0.3$ vorhersagen. Desweiteren sind die produzierten stellaren Oberflächenhelligkeitsprofile konsistent mit realen BCGs ähnlicher Massen bei Rotverschiebung $z = 0$ und $z = 1$. Außerdem wird gezeigt, dass die ΛCDM Kosmologie tatsächlich kleinere und größere Merger in Haufengalaxien vorher-

sagt, und zwar mit der Häufigkeit und Massenverteilungsrate, die benötigt wird, um die beobachteten Wachstumsraten von passiven Galaxien seit $z = 2$ zu erklären.

In Kapitel 6 wird die Frage nach der Verteilung der DM im Zentrum von Haufengalaxien wieder aufgegriffen. Es wird eine Methode entwickelt, um selbst-gravitative Gleichgewichtverteilungsfunktionen in die in den kosmologischen Simulationen gebildeten DM Halos einzufügen.Es stellt sich heraus, dass das Gesamtdichteprofil unter Hinzunahme von Baryonen bei $z = 2$ durch die hohe Zahl an Mergern im Zentrum von Haufengalaxien wieder nahe an dem der ursprünglichen reinen DM Simulationen liegt (mit Ausnahme der innersten Bereiche, $\sim 5\,\mathrm{kpc}$). Diese Ergebnisse legen die Existenz einer Attraktor-Lösung für kollisionsfreie Systeme nahe, ungeachtet der Hinzunahme von Baryonen, bei denen Mischvorgänge effektiv sind. Die Dichteprofile von DM in den Resimulationen sind flacher als die in den reinen DM Simulationen mit einem Unterschied von $\Delta\gamma \equiv \Delta(\frac{d\ln\rho}{d\mathrm{lnr}}) \sim 0.3 - 0.4$. Die Skala, auf der dieser Übergang geschieht, ähnelt der von Beobachtungen um $r/r_{200} \sim 0.01 - 0.02$ suggerierten Skala. Es wird außerdem vermutet, dass der Effekt der Erhitzung durch dynamische Reibung von einfallenden Schwarzen Löchern die weitere zentrale Massenverteilung innerhalb von $r \sim 5\,\mathrm{kpc}$ beeinflussen kann. Die berechneten Massendefizite könnten eine natürliche Erklärung für einige der größten zentralen Sternkonzentrationen innerhalb von $r_c \sim 3\,\mathrm{kpc}$ darstellen, die in BCGs beobachtet werden.

Der letzte Teil dieser Arbeit konzentriert sich auf die systematischen Effekte, die durch die Triaxialität in der sphärischen Modellierung der dSphs mit Hilfe von N-Körper Galaxiemodellen innerhalb von DM Halos aus dem finalen Zustand von kosmologischen Simulationen in ΛCDM entstehen. Nach aktuellem Forschungsstand sind die Dichteprofile der DM von zwei der hellsten dSphs (Sculptor und Fornax) zentral abgeflacht (DM cores), was möglicherweise eine Herausforderung für die Physik der Galaxienbildung darstellt oder sogar die Natur der DM Teilchen in Frage stellt (nämlich dass diese kollisionsfrei und bei Entkopplung nichtrelativistisch sind). In diesem Kapitel wird geprüft, ob die komplexe Struktur von CDM DM Halos Beobachter dazu verleiten kann, von DM cores auszugehen, wenn eigentlich DM cusps vorliegen. Es stellt sich heraus, dass dies nicht der Fall ist. Es bleibt abzuwarten, ob die gefolgerte Verteilung von DM in Zwerggalaxien tatsächlich zentral abgeflacht ist, oder ob eine allgemeine Klasse von Verteilungsfunktionen existiert, die mit den Beobachtungsdaten für zentral abgeflachte DM Halos übereinstimmt. In jedem Fall scheint dieses Resultat Thesen von Seiten der beobachtenden Astrophysik zu unterstützen.

Summary

This thesis is concerned with the formation and evolution of the Brightest Cluster Galaxies (BCGs) and the central distribution of matter in galaxy clusters within the ΛCDM paradigm through cosmological N-body simulations. It addresses the following questions: Do BCGs grow from dissipationless mergers in the last 10 Gyrs? If so, what would their structural properties look like? Do the predicted mass growth rates of BCGs in ΛCDM agree with those observed? What is the impact of this purely dissipationless formation channel for BCGs on the central distribution of dark matter in galaxy clusters? Do observations of the matter distribution in galaxy clusters really suggest/imply that the idea that dark matter is cold and collisionless needs to be reconsidered? The first three chapters serve as a review of cosmology, structure formation, the nature of dark matter and numerical techniques used in cosmological N-body simulations. In Chapter 4, we study the formation of shallow dark matter cusps through dissipationless mergers using a set of cosmological N-body simulations and several rescaled versions. We study the dependence of initial stellar structure on the internal mixing between dark matter and stars at the centre of clusters at late times. We find that qualitatively shallow dark matter cusps at the centre of galaxy clusters are naturally expected if the formation of BCGs is primarily driven by dissipationless mergers. In Chapter 5, we develop a general weighting scheme to generate equilibrium tracer distribution functions of the form $f(E)$ in triaxial potentials. We apply this scheme to a suite of nine high-resolution dark matter only simulations of galaxy clusters halo formation to follow the assembly of BCGs and cluster ellipticals using the latest observational constraints on galactic structure combined with stellar-to-dark matter relations. We show that the dissipationless merger channel in ΛCDM is consistent with predicting the stellar mass assembly of BCGs with growth rates of ~ 2.1 in the range $0.3 < z < 1.0$ and by a factor of ~ 1.4 in the range $0.0 < z < 0.3$, consistent with observations. Furthermore, the stellar surface brightness profiles produced are consistent with real BCGs for similar mass clusters at $z = 0$ and $z = 1$. We also demonstrate that the ΛCDM cosmology does indeed predict minor and major mergers to occur in galaxy clusters with the frequency and mass ratio distribution required to explain the observed growth in size of passive galaxies since $z = 2$. In Chapter 6 we return to the question of the distribution of matter at the centre of galaxy clusters. We develop a method to directly insert self-gravitating equilibrium distribution functions inside dark matter haloes formed in cosmological simulations. It is found that after baryonic loading at $z = 2$, the high number of mergers occurring at the centre of the galaxy clusters take the total

density profile back to a solution closely resembling that of the original dark matter only runs (except in the inner-most regions below $6 - 4\,\mathrm{kpc}$). This suggests the existence of an attractor solution for collisionless systems, irrespective of the baryonic loading where mixing is effective. The dark matter density profiles in these re-simulaitons as a result are shallower than those in the dark matter only runs with a difference of $\Delta\gamma \sim 0.3 - 0.4$. The scale at which the transition occurs is exactly similar with that inferred by observations around $r/r_{200} \sim 0.01 - 0.02$. We further estimate that the effect of dynamical friction heating impeded by infalling black holes can affect further the central mass distribution below $r \sim 4 - 6\,\mathrm{kpc}$. Our calculated mass-deficits would provide a natural explanation for some of the largest stellar cores of $r_c \sim 3\,\mathrm{kpc}$ observed in BCGs. The final part of the thesis focusses on the systematics introduced by triaxality in the spherical modelling of dSphs using N-body galaxy models within dark matter haloes from the end state of cosmological N-body simulations in ΛCDM. The current claim is that the dark matter density profiles for two of the most luminous dSphs (Sculptor and Fornax) are cored and this may be a challenge for galaxy formation physics or maybe even put into question the very nature of the dark matter particle (the facts that it is a non-relativistic particle at decoupling and that it is collisionless). This chapter tests whether the complicated structure of CDM dark matter haloes can fool observers in their inference for cores in the actual presence of cusps. It is found that this is not the case. It remains to be seen whether the inferred distribution of dark matter in dwarfs is indeed cored, or whether there exists a general family of distribution functions which are consistent with the observational data for dark matter haloes which are cored. In any case, this result seems to further credit observational claims.

Part I

Overview

Pour Marie-Amélie Laporte (1956-2012),
To my cousin Pierre Demarque,
Für alle meine Münchner Freunden,

Chapter 1

Background Cosmology & Structure Formation

While it is difficult to give a rigorous overview of all subfields of astrophysics that make the basis of this thesis - this should be the topic of a textbook - I shall discuss a few selected salient aspects of physics which form the backbone to understanding structure formation in its full cosmological context. I shall focus more specifically on our currently most favoured cosmological model, the ΛCDM paradigm which is at the heart of the work presented in this thesis. In passing, I will point out the relevant references which go in further details on each subject.

1.1 Background Friedman Robertson-Walker Cosmology

The description of the standard cosmological model is based on two fundamental observations about the Universe. Firstly, on large scale the Universe is *homogeneous* and *isotropic*. That is to say, there is no preferred observing position and the Universe looks the same in every direction. This is the *Copernican* principle. Second, space expands such that the physical distance between any two fundamental observers (i.e. one at rest with respect to the matter field around it) must have the form:

$$\mathbf{r} = \mathbf{x}a(t), \tag{1.1}$$

where we have introduced the scale factor which connects co-moving coordinate $\mathbf{x}$ to the physical one $\mathbf{r}$. This is known as Hubble's law of expansion.

Observation of the Cosmic Microwave Background (CMB) confirm homogeneity to the level of $\frac{\Delta T}{T} \sim \mathcal{O}(10^{-5})$ (Smoot et al., 1992). This is shown in Figure 1.1. Observations of the large scale structures (LSS) also confirm isotropy when smoothing the density field on scales of $100\,h^{-1}\,\mathrm{Mpc}$ (Figure 1.2).

From Einstein's theory of General Relativity, it is possible to derive the equations governing the evolution of such a Universe. This is done by specifying the metric tensor

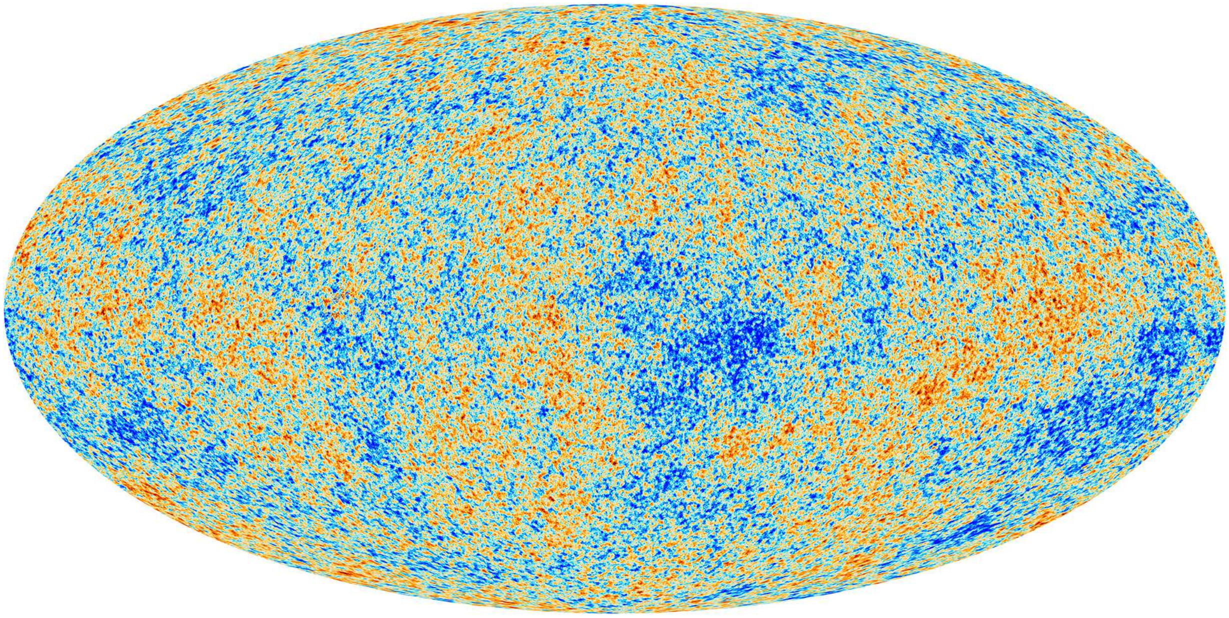

Figure 1.1: Cosmic Microwave Background from the Planck 2013 collaboration. The temperature fluctuations are so small $\frac{\Delta T}{T} \sim \mathcal{O}(10^{-5})$, supporting the idea that the Universe is homogeneous on large scales.

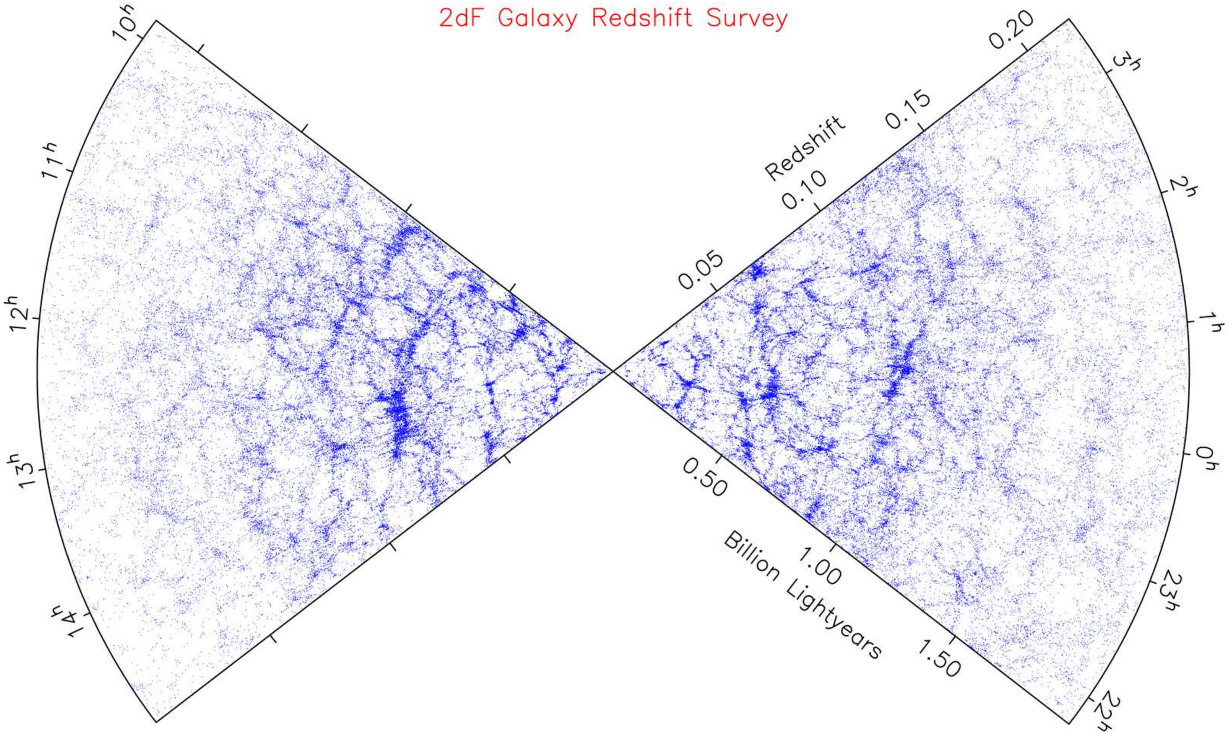

Figure 1.2: The large-scale structures as seen by the 2 degree Field Galaxy Redshift Survey (2dFGRS) (Peacock et al., 2001). The Universe on scales of $\sim 100\,h^{-1}$Mpc is isotropic

$g_{\mu\nu}$ for which the line element is:

$$ds^2 = g_{\mu\nu}dx^{\mu}dx^{\nu}. \tag{1.2}$$

The most general metric for an isotropic and homogeneous Universe is given by the Robertson-Walker metric:

$$ds^2 = c^2dt^2 - a^2(t)\left(\frac{dr^2}{1-kr^2} + r^2(d\theta^2 + sin^2\phi^2)\right), \tag{1.3}$$

where (r, θ, ϕ) are comoving coordinates in spherical coordinates (i.e., $r^2 = x^2 + y^2 + z^2$) and k is the spatial curvature (which can take values of -1, 0 and 1).

The equations governing the evolution of the Universe can be derived by manipulating the Einstein field equation:

$$R_{\mu\nu} - \frac{1}{2}g_{\mu\nu}R - g_{\mu\nu}\Lambda = \frac{8\pi G}{c^4}T_{\mu\nu}, \tag{1.4}$$

Where $T_{\mu\nu}$ is the energy momentum tensor, R the curvature scalar and $R_{\mu\nu}$ the Ricci tensor.The Ricci tensor and curvature scalar can be calculated from the metric. For a perfect fluid (one with no viscous stress), the energy-momentum tensor is entirely specified by the rest frame density ρ and isotropic rest frame pressure P and so $T_{\mu\nu}$ is diagonal. The general form in any frame is given by:

$$T^{\mu\nu} = (\rho + P)U^{\mu}U^{\nu} + Pg^{\mu\nu} \tag{1.5}$$

For a uniform ideal fluid in the rest frame this reduces to $T_{\mu\nu} = \text{diag}(\rho, -g_{ii}P)$. Solving for the $_{00}$ and $_{ii}$ components one recovers two equations fully specifying the evolution of the cosmological background.

These are the Raychaudhuri equation

$$\frac{\ddot{a}}{a} = -\frac{4\pi G}{3}\left(\rho + 3\frac{P}{c^2}\right) + \frac{\Lambda c^2}{3} \tag{1.6}$$

and the Friedmann equation

$$\left(\frac{\dot{a}}{a}\right)^2 = \frac{8\pi G}{3}\rho - \frac{kc^2}{a^2} + \frac{\Lambda c^2}{3}. \tag{1.7}$$

Observations of the CMB and the LSS find that the Universe is flat and composed of radiation, matter (in the form of baryons and dark matter) and dark energy (represented by a cosmological constant Λ) causing an accelerated rate of expansion at late times.

The Pressure term can be written in a general form $P = w\rho c^2$. Substituting this into the continuity equation we see that the density evolves as:

$$\rho \propto a^{-3(1+w)} \tag{1.8}$$

Substituting ρ into the Friedmann equation gives the evolution of the scale factor with time:

$$a \propto t^{2/3(1+w)}, \forall\, w \neq -1 \tag{1.9}$$

We now need to define some quantities.

Hubble parameter: This defines the expansion rate of the Universe $H(t) = \frac{\dot{a}}{a}$. The expansion rate at the present time is the Hubble constant $H(t_0) = H_0 = 100h\,\mathrm{km/s/Mpc}$, where h is a dimensionless number ($h \sim 0.7$).

Redshift: As a consequence of the expansion of the Universe, light signals (which follow null geodesics $ds = 0$) get cosmologically redshifted. We define redshift as $1+z \equiv \frac{\lambda_0}{\lambda e} = \frac{a(t_0)}{a(t_e)}$, where λ_0, λ_e, $a(t_0)$, $a(t_e)$ are the wavelengths and scale factors of the light as observed by an observer today and at emission respectively. In cosmology we generally normalise the scale factor such that at the present time $a(t_0) = 1$. This gives the following relation for redshift $1 + z = a^{-1}$. Redshift can also be translated into time due to its dependence on a.

Density parameter: This defines the energy density of all constituents in the Universe $\Omega = \frac{8\pi G}{3H^2}\rho = \frac{\rho}{\rho_{crit}}$, where ρ_{crit} is the critical density of the Universe and changes with time due to its dependency on the Hubble parameter.

Thus we can re-write the Friedmann equation as:

$$\Omega(a)^{-1} - 1 = -\frac{3kc^2}{8\pi G\rho a^2} \tag{1.10}$$

1.1.1 Inflation

When looking at the CMB it is puzzling to see that homogeneity is validated even on patches where according to the classical Big Bang theory there could not have been any causal contacts between them. This is generally referred to as the horizon problem. Moreover, when looking at the Friedmann equation (for non-zero matter and radiation content), the value $\Omega = 1$ is an attractor solution when going back at high redshifts. Given the that the Universe is very close to flat (with Ω only deviating mildly from unity) requires great fine-tuning at earlier times. This is called the flatness problem. These problems are solved altogether by invoking a period of accelerated expansion at early times. This is called *inflation* is generally implemented using a scalar field with special dynamical properties. Because during an accelerated period of expansion, the comoving horizon decreases ($\frac{\mathrm{d}}{\mathrm{d}t}\left(\frac{1}{aH}\right) < 0$) and thus regions which were actually in causal contact can no longer communicate. One of the most important predictions from inflation is the primordial form of the matter power-spectrum (an important quantity for the study of the growth of structure) for which we quote the final result.

$$P(k) = Ak^n, \tag{1.11}$$

where n is the spectral index and A is the normalisation. At the end of inflation, the Universe goes through a period of re-heating giving rise to the Hot Big Bang which starts during the radiation era. For an account on inflation we recommend the reader the following textbooks (Liddle & Lyth, 2000; Mukhanov, 2005).

1.2 A word on thermal history of the Universe

At early times, during the radiation era, the temperature of the Universe is so high that it consists of a hot plasma of relativistic particles ($\nu_e, \nu_{\bar{e}}, e, \bar{e}$) and photons in thermal equilibrium (e.g. via Compton scattering). This is guaranteed as long as the interaction rate, Γ, of the species with the photon fluid is higher than the expansion of the Universe (i.e. $\Gamma \gg H$). As the Universe expands the temperature drops, the interaction rate decreases and species gradually come out of equilibrium and decouple from the photon fluid. Eventually, matter-domination takes over and at a temperature of $T \sim 3000$K, the photon energies are too low to keep the Universe ionised. This is the time of *recombination* when the primordial plasma coalesces to produce neutral hydrogen and the mean free path of photons has increased to the size of the observable universe, giving rise to CMB that we can observe today. The physics of this period is generally quite well understood in terms of the thermodynamics and particle physics involved up to a certain point where classical theories break down. Accounts on this can be found in Kolb & Turner (1990). Figure 1.3 shows a timeline summary of the history of the Universe according to the new Planck Collaboration et al. (2013) cosmology.

1.3 Growth of Structure in the linear regime and the large-scale structures

On scales smaller than $100\,h^{-1}\,$Mpc, the observed Universe is nothing but isotropic and homogeneous. The galaxies which trace the matter density field are grouped in clusters, filaments and empty regions known as voids (see Figure 1.2). Growth of structure needs to be seeded by fluctuations in the matter density field $\rho(\mathbf{x}, t)$, leading to a density contrast:

$$\delta(\mathbf{x}, t) = \frac{\rho(\mathbf{x}, t) - \bar{\rho}(t)}{\bar{\rho}(t)}, \tag{1.12}$$

where $\rho(\mathbf{x}, t)$ is the density field at position $\mathbf{x}$ and ρ is the background density.

The primordial fluctuations in the density field are thought to originate from quantum fluctuations (related to Heisenberg's uncertainty principle) in the very early Universe which later got stretched during inflation giving rise to a Gaussian random density field with a characteristic power spectrum (as discussed in the previous section). This random Gaussian field evolves through the action of gravity and we generally identify two regimes in the growth of perturbations. The linear regime where $\delta \ll 1$ (i.e. the amplitude of the perturbations are small) and the non-linear one where the $\delta \gg 1$.

A rigorous treatment of growth of structure in the linear regime requires perturbing the FRW metric, solving the perturbed Einstein equations and study how the various perturbations in the complex fluid (made up of collisionless dark matter, photons, neutrinos, and collisional baryonic matter) evolve by solving the Boltzmann equation and at different times (radiation domination and matter domination) and taking account of dissipation effects such as Silk damping (the damping of small-scale oscillations in the baryons due to photon diffusion which occurs at decoupling between matter and radiation) and damping from the streaming velocities of collisionless particles (which introduces a cut-off in the power spectrum). The behaviour for the growth of perturbations for each species is different on scales outside and inside the horizon and at different epochs (during radiation domination and matter domination). We shall not discuss relativistic perturbation theory but refer the reader to Ma & Bertschinger (1995) which covers this in appropriate details and for two different choices of gauges (synchronous and conformal Newtonian). Instead we shall only quote the final results from such calculations.

It is interesting to note that, the GR solutions are equivalent to the Newtonian treatment on scales within the horizon for cold dark matter and baryons after decoupling. Furthermore, in the current cosmological model, the most dominant form of matter is a non-relativistic collisionless fluid (cold dark matter) which is the main actor in structure formation so we shall instead spend more time discussing the evolution of this component.

1.3.1 Collisional fluid

Consider a fluid with pressure P, density ρ and velocity field $\mathbf{u}$ in an expanding Universe and a potential $\Phi(\mathbf{x}, t)$. The equations of motion of the fluid are:

$$\text{Continuity} \;\; \partial_t \rho + \nabla_{\mathbf{r}} \cdot (\rho \mathbf{u}) = 0, \tag{1.13}$$

$$\text{Euler} \;\; \partial_t \mathbf{u} + (\mathbf{u} \cdot \nabla_{\mathbf{r}})\mathbf{u} = -\frac{1}{\rho}\nabla_{\mathbf{r}} P - \nabla_{\mathbf{r}} \Phi, \tag{1.14}$$

$$\text{Poisson} \;\; \nabla^2_{\mathbf{r}} \Phi = 4\pi G \rho. \tag{1.15}$$

If we now work in comoving coordinates $\mathbf{x}$ defined as $\mathbf{r} = a(t)\mathbf{x}$ (the proper velocity $\mathbf{u} = \dot{\mathbf{r}} = \dot{a}(t)\mathbf{x} + \mathbf{v}$, $\mathbf{v} \equiv a\dot{\mathbf{x}}$), the time and spatial derivatives transform as

$$\nabla_{\mathbf{r}} \to \frac{1}{a}\nabla_{\mathbf{x}}; \;\; \frac{\partial}{\partial t}\Big|_{\mathbf{r}} \to \frac{\partial}{\partial t}\Big|_{\mathbf{x}} + \frac{\partial x}{\partial t}\Big|_{\mathbf{r}} \cdot \nabla_{\mathbf{x}} = \frac{\partial}{\partial t} - \frac{\dot{a}}{a}\mathbf{x} \cdot \nabla_{\mathbf{x}}. \tag{1.16}$$

Perturbing ρ, $\mathbf{u}$ and Φ about their background values:

$$\rho \to \bar{\rho}(t) + \delta\rho \equiv \bar{\rho}(t)(1 + \delta) \tag{1.17}$$

$$P \to \bar{P}(t) + \delta P \tag{1.18}$$

$$\mathbf{u} \to a(t)H(t)\mathbf{x} + \mathbf{v} \tag{1.19}$$

$$\Phi \to \bar{\Phi}(\mathbf{x}, t) + \phi \tag{1.20}$$

If one substitutes these back into the evolution equations of the fluid and keep only the terms up to linear order we obtain the following linearised equations:

$$\partial_t \delta + \frac{1}{a}\nabla \cdot \mathbf{v} = 0 \tag{1.21}$$

$$\partial_t \mathbf{v} + H\mathbf{v} = -\frac{1}{a\rho}\nabla \delta P - \frac{1}{a}\nabla \phi \tag{1.22}$$

$$\nabla^2 \phi = 4\pi G a^2 \bar{\rho}\delta \tag{1.23}$$

If we now take the time derivative of the perturbed continuity equation and combine it with the perturbed Euler and Poisson equations we obtained the fundamental equation for the growth of structure in Newtonian theory, which illustrates the competition between infall by gravitational attraction and pressure support:

$$\partial_t^2 \delta - 2H\partial_t \delta - 4\pi G\bar{\rho}\delta - \frac{1}{a^2\bar{\rho}}\nabla^2 \delta P = 0 \tag{1.24}$$

If we additionally consider a barotropic fluid ($P = P(\rho)$) then $\delta P = \frac{\partial P}{\partial \rho}\bar{\rho}\delta$ and if we Fourier expand so that $\nabla^2 \to -k^2$ we arrive at:

$$\ddot{\delta}_{\mathbf{k}} + 2H\dot{\delta}_{\mathbf{k}} + (\frac{c_s^2 k^2}{a^2} - 4\pi G\bar{\rho})\delta_{\mathbf{k}} = 0 \tag{1.25}$$

This is the equation for a damped oscillator provided that $\frac{c_s^2 k^2}{a^2} > 4\pi G\bar{\rho}$, giving rise to acoustic oscillations in the fluid. For $c_s^2 k^2/a^2 < 4\pi G\bar{\rho}$ the system is unstable and undergoes gravitational collapse. The characteristic scale of importance here is the Jeans length

$$\lambda_J \equiv \frac{2\pi a}{k_J} = c_s\sqrt{\frac{\pi}{G\bar{\rho}}}, \tag{1.26}$$

which is the distance a sound wave can travel in a gravitational free-fall time. Only perturbations with $k < k_J$ can grow.

The equivalent equation for a collisionless collisionless fluid with no velocity stress reduces is equivalent to that of a collisional fluid with zero pressure. Thus the equation governing the growth of perturbations for dark matter in the linear regime is the same as that for the baryons but omitting the pressure term. The fluid treatment for dark matter becomes invalid in the regime where the velocity dispersion of the collisionless gas is non-negligible and the particles can stream away. In those instances one needs to follow the evolution of the full distribution function (using perturbation theory). This will not be discussed here but the reader can find a discussion in Ma & Bertschinger (1995).

We summarise here the main results from the GR analysis of the growth and evolution of the perturbations, quoting only results within the horizon:

- **radiation domination era inside the horizon**: Cold dark matter grows $\delta \propto \log(t)$. This growth is due to the effect of radiation causing a more rapid expansion, slowing down the growth of dark matter perturbations (Meszaros effect). Baryons and radiation are still in the tight coupling regime thus $\delta_b \propto \delta_r$ and baryons undergo acoustic oscillations.

- **baryon decoupling/ recombination inside the horizon**: Cold dark matter grows as $\delta_c \propto t^{2/3}$ as the Universe is very close to an Einstein de Sitter spacetime. Baryons are no longer coupled to radiation, thus they are able to catch up with cold dark matter.

1.4 Growth of matter and dark matter perturbations after recombination

After matter-radiation equality, on scales of cosmological interest which are larger than the Jeans scale of baryons, both fluctuations in CDM and the baryons have the same dynamical equation. Quickly after recombination, the overdensity in baryons δ_b follows that of cold dark matter δ_c and the matter behaves as a single collisionless fluid for which $\delta_m = \frac{\bar{\rho}_b\delta_b+\bar{\rho}_c\delta_c}{\bar{\rho}_b+\bar{\rho}_c} \approx \delta_c$. Furthermore the Universe in this regime is close to an Einstein de-Sitter Universe (with zero curvature and no dark energy terms).

In this case the perturbation growth equation can be simplified to

$$\ddot{\delta}_m + \frac{4}{3t}\dot{\delta}_m - \frac{2}{3t^2}\delta_m = 0, \tag{1.27}$$

where we used the facts that $H^2 \propto \bar{\rho} \propto a^{-3}$, $a \propto t^{2/3}$ so $H = 2/(3t)$ and $4\pi G\bar{\rho} = 2/(3t^2)$.

If we try solutions of the form $\delta \propto t^{\beta}$, we find that this equation admits two independent solutions: a growing $D_+ \propto t^{2/3}$ and decaying mode $D_- \propto t^{-1}$, thus general solution is given by their linear combination:

$$\delta_m = AD_+(t) + BD_-(t), \tag{1.28}$$

where A and B are constants. The growing modes eventually take over the decaying ones and we can write the solution as $\delta \propto D_+(t) = D(t)$. For a general cosmology, the growing mode is given by:

$$D(t) = H(t)\int_0^t \frac{\mathrm{d}t'}{a^2(t')H^2(t')} = H(t)\int_0^a \frac{\mathrm{d}a}{\dot{a}^3} \tag{1.29}$$

1.4.1 Primordial Power spectrum and its relation to the Post-recombination one

It is important to note that as the perturbations grow, the shape of the primordial power-spectrum changes as the Universe evolves from the end of inflation down to the post-recombination era. One thus needs to relate the history of the growth of the perturbation of all modes to the time of post-recombination. This can be all encapsulated in the transfer function $T(k)$ which relates the power spectrum in the post-recombination era to that of initial conditions from inflation. In a way, the $T(k)$ contains all of the relevant physics of the early Universe which affected the primordial density field $\delta_i(\mathbf{x})$.This is given by

$$P(k,t) = \langle | \, \delta(\mathbf{k},t)\delta^*(\mathbf{k}',t) \, | \rangle = P_i(k)D(t)^2 T^2(k,t) \tag{1.30}$$

The computation of transfer functions for different kinds of cosmological models can be done with codes such as CMBFast (Seljak & Zaldarriaga, 1996) or CAMB (Lewis et al., 2000) in order to set up initial conditions of random gaussian fields for cosmological N-body simulations. Examples of transfer functions are shown in Figure 1.4.

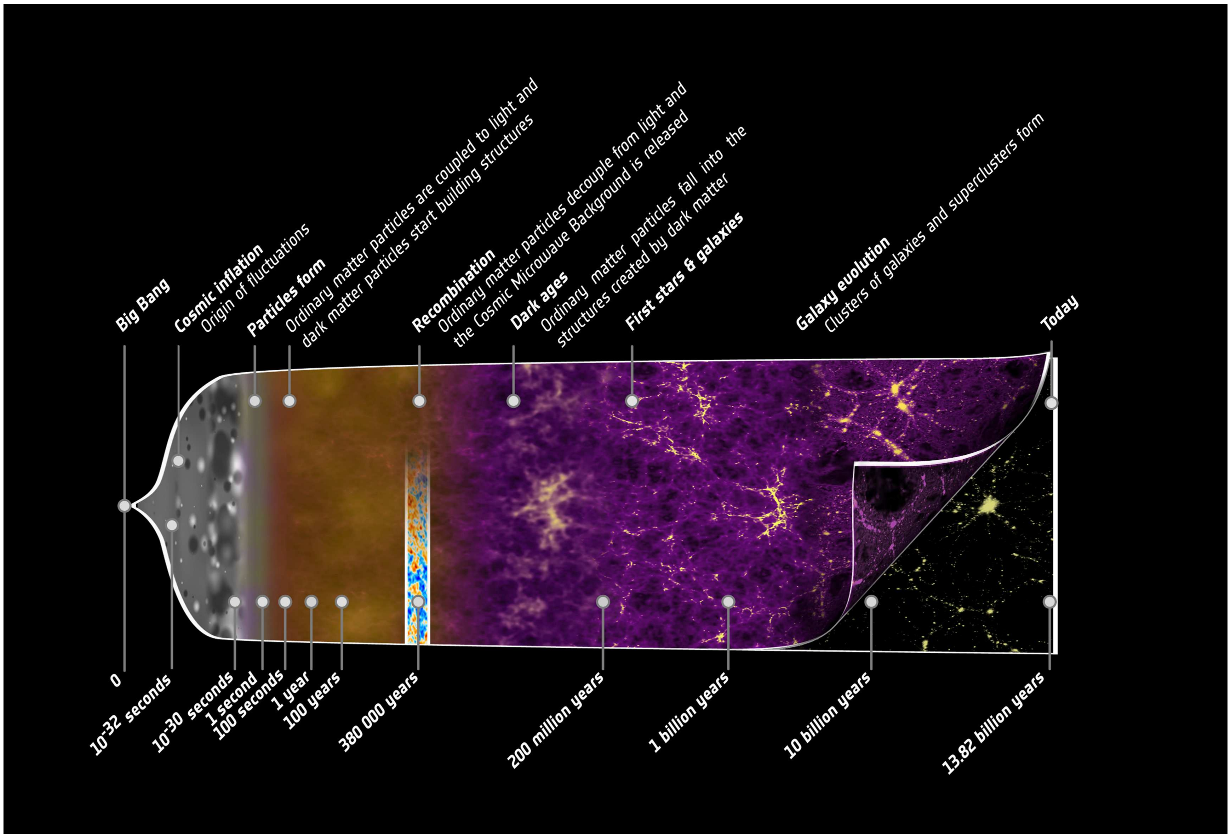
Big Bang
Cosmic inflation
Origin of fluctuations
Particles form
Ordinary matter particles are coupled to light and
dark matter particles start building structures
Recombination
Ordinary matter particles decouple from light and
the Cosmic Microwave Background is released
Dark ages
Ordinary matter particles fall into the
structures created by dark matter
First stars & galaxies
Galaxy evolution
Clusters of galaxies and superclusters form
Today
0
10^{-32} seconds
10^{-30} seconds
1 second
100 seconds
1 year
100 years
380 000 years
200 million years
1 billion years
10 billion years
13.82 billion years

Figure 1.3: Timeline of the Universe. Shortly after the Big Bang came a period of accelerated expansion (inflation) during which the primordial quantum fluctuations got stretched to macroscopic scales. At the end of inflations the scalar field decays giving rise to particle creation. The Universe is in a hot state in which particles are coupled to the photons. As the Universe expands and cools species come out of equilibrium until eventually at recombination the Universe is no longer opaque, neutral hydrogen is produced and photons can freely stream giving rise to the CMB. The later phase of evolution of the Universe is orchestrated by dark matter forming structures in a hierarchical fashion in which baryons can fall into, form the first stars and galaxies and eventually galaxy clusters we see today.

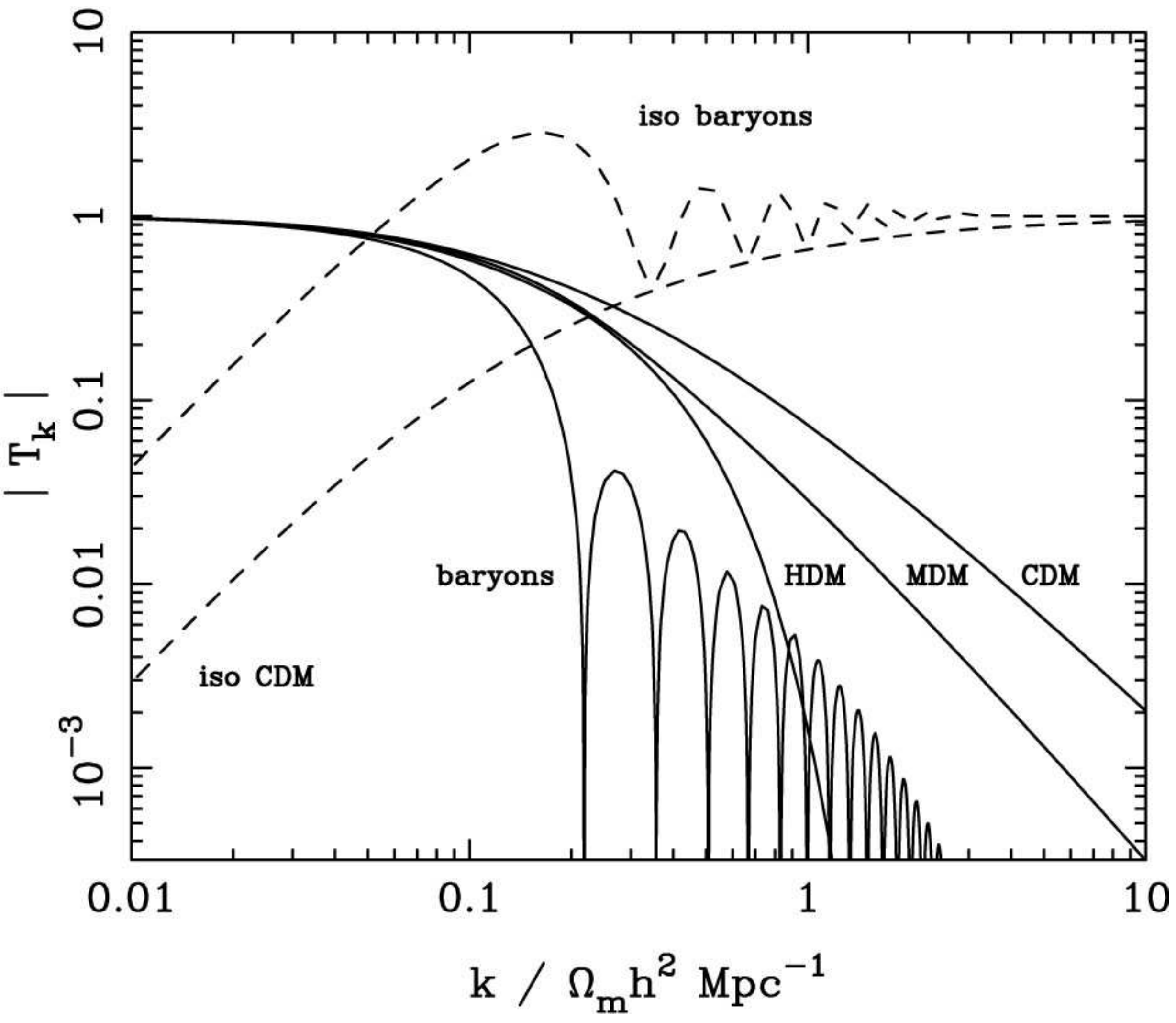

Figure 1.4: An example of a transfer function. The baryons show signs of oscillations (this is due to the pressure term present in the equation governing the growth of perturbations) which dampen away for small k (due to Silk damping). Dark matter also shows signs of damping, this is due to the streaming velocities of the dark matter particles. For hot dark matter this is quite pronounced and occurs at roughly the same k as for the baryons (this is because these particles come out as relativistic at decoupling). For cold dark matter the streaming velocities introduce a cut off too but at much larger k.

Chapter 2

Dark Matter

The most abundant form of matter in the Universe is dark matter. It is thought to be a collisionless fluid that comes out as non-relativistic at the time of decoupling and that interacts only with ordinary matter solely through the force of gravity. In this section we give a brief account of the observational evidence on different scales in support for dark matter. We then discuss the motivations behind why this component cannot be baryonic (the best evidence comes from a cosmological stand point) and introduce the idea of cold dark matter that is at the heart of the standard cosmological model. We then close this section by introducing the principal candidates beyond the standard model that have been proposed by particle physics to account for the dark matter and currently ongoing experiments.

2.1 Observational evidence

2.1.1 Galactic scales

On galactic scales, the evidence for dark matter first came from the observation of rotation curves of spiral galaxies (e.g. (Rubin & Ford, 1970)). These measure the circular velocity of galaxies as a function of radius using optical long-slit spectroscopy or the Doppler shift from the HI 21cm hyperfine transition line associated with the neutral hydrogen gas which extends much further than the optical part traced by the stars. Such measurements have now been performed for a large amount of objects and they all exhibit the same unexpected behaviour: they are flat beyond the edge of their exponentially falling stellar disks. According to Newtonian gravity the circular velocity of a spherical system is defined as $v(r) = \sqrt{(}GM(r)/r)$, where $M(r)$ is the enclosed mass within radius r. Outside the stellar disk, $M(r)$ is expected to be constant (the neutral gas is not self-gravitating and thus counts as a tracer of the underlying potential), thus circular velocity should follow a Kepler falloff $v(r) \propto 1/\sqrt{(}r)$. If Newtonian gravity is correct, then the flatness of these curves imply that galaxies must be surrounded by extended dark matter haloes with $M(r) \propto r$ beyond their stellar disks.

Strong lensing in galaxies also another manifestation in support for dark matter. In general relativity, light follows null geodesics and gets bent by mass. The projected visible mass density in the plane of a galaxy is negligible to create large deflection angles at the positions where multiple images and arcs appear in lensing galaxies. The multiple images and arcs that are seen around some massive elliptical galaxies or in galaxy clusters imply that the total projected surface density is much higher than that of the stars. In the case, when a galaxy sits directly behind another, this configuration creates an Einstein ring. This feature can be explained to first order if one models the matter distribution as a singular isothermal sphere, where $\rho \propto r^{-2}$ (note these have also the same property as to produce flat circular velocity curves with $M(r) \propto r$). Many lenses have been studied showing clear evidence for more matter surrounding galaxies beyond their optical radius.

2.1.2 Galaxy Cluster scales

Already in the 30s, Zwicky (1933) reported the need for dark matter to explain the mass of the Coma Cluster . Using its member galaxies in combination with the virial theorem, he estimated the total mass of Coma and noted that the inferred total mass was factor of 400 off compared to the sum of all the visible light in the cluster galaxies. He later concluded that this dark matter could be observed with the aid of gravitational lensing (Zwicky, 1937). Fritz Zwicky was clearly ahead of his time and it took about 40 years for the idea of dark matter to be really seriously considered by astrophysicists. Nowadays galaxy clusters offer us a great number of probes for studying in detail their total matter content as well as their dark matter content: stellar kinematics from the central galaxies, strong and weak lensing, X-ray emission from the hot electron gas in hydrostatic equilibrium, the motion of satellite galaxies. These various independent probes for mass give all similar answers when compared to each other, providing clear evidence that dark matter dominates the mass budget of galaxy clusters out to large radii ($\sim$ 3Mpc)

2.1.3 Cosmological scales

Existence for (non-baryonic) dark matter is now also required from a cosmological point of view. Detailed studies of the cosmic microwave background (CMB), in particular of its angular temperature power spectrum can put strong constraints on the cosmological parameters of a given model (see Figure 2.1). If dark matter would be baryonic it would oscillate with the baryon fluid during radiation era and at radiation-matter decoupling, the perturbations would also get Silk damped in such a way that there would not be any structures on scales smaller than $\sim$ 1Mpc. Dark matter needs to be non-baryonic so that the primordial potential in which baryons fall into can already be in place. The CMB temperature power spectrum is sensitive to various cosmological parameters in particular Ω_b and Ω_m. Matter raises the amplitude of the peaks due to growth of structure. Baryons on the other hand change the amplitude of the the first peak but not the subsequent ones due to the damped oscillations in the baryon fluid and Silk damping acting to suppress the growth of perturbations on smaller scales.

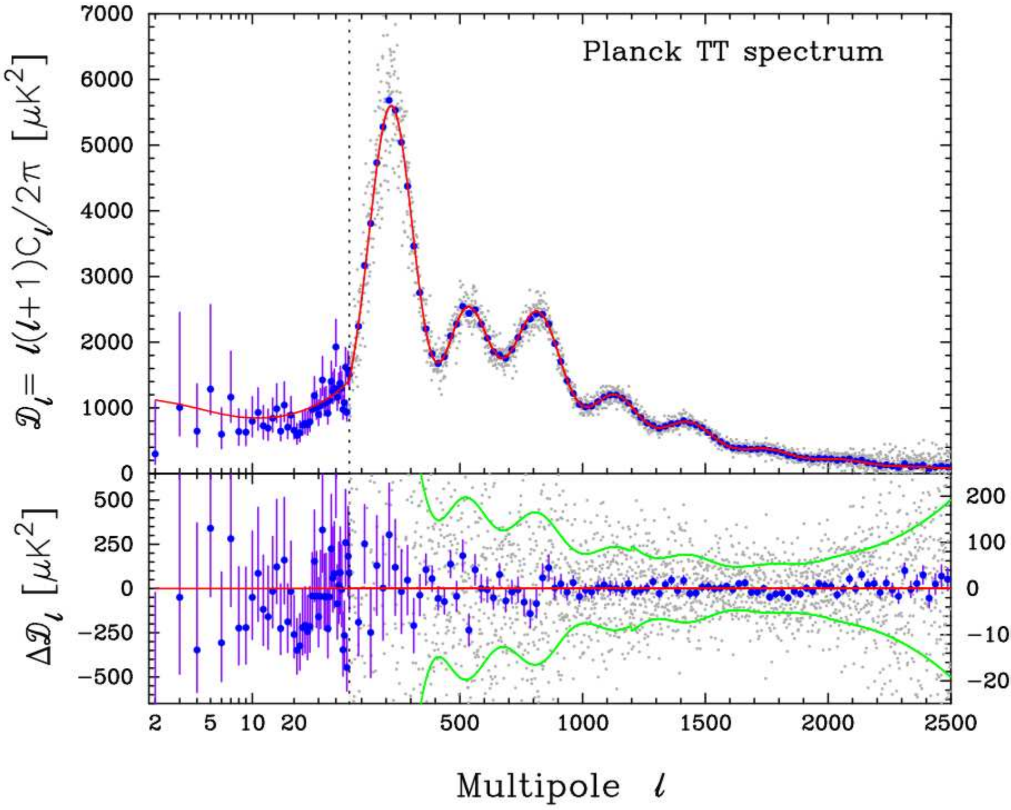

Figure 2.1: Temperature power spectrum (Planck Collaboration et al., 2013). The red line is the best-fit ΛCDM model. Measurements like this can put strong constraints on the matter content of our Universe.

2.1.4 Collisionless Cold Dark matter

The main support for cold dark matter (as opposed to hot dark matter) comes from numerical simulations (see Figure 2.2). It seems the Universe in which we live in is consistent with hierarchical growth of structure. Hot dark matter on the other hand exhibits an anti-hierarchical behaviour in the growth of structure with clusters being the first objects to form.

Support for the collisionless nature of dark matter comes from observations such as that of the Bullet Cluster (Figure 2.3). This merging cluster shows two clumps of galaxies in its optical image. In X-rays, the hot electron gas sits between the two clumps and shows that it has been shocked. Weak lensing can also be used to map the total distribution of matter to be situated in the two separate galaxy clumps. If dark matter was collisional it would also sit at the same position of the hot electron gas. The fact that the dark matter

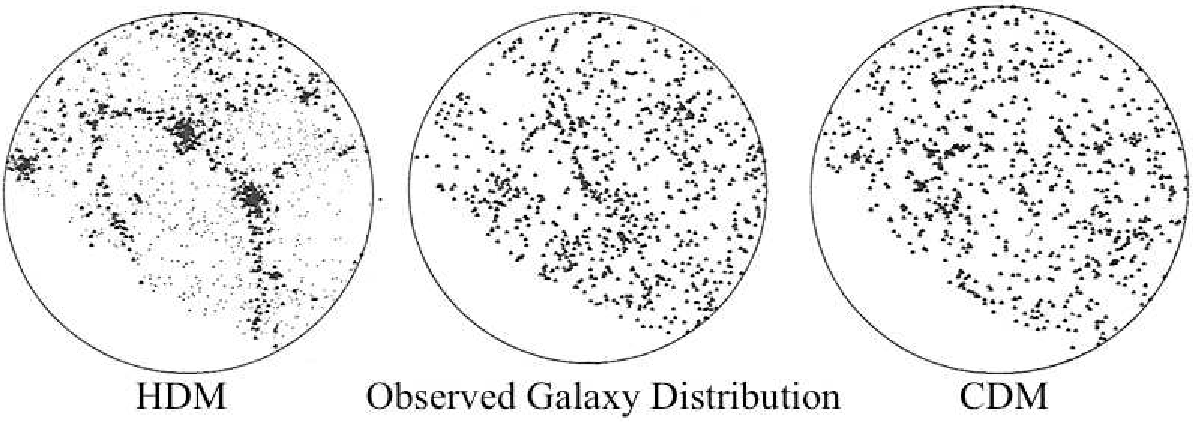

Figure 2.2: Comparison between the observed distribution of galaxies from the CfA survey (Huchra et al., 1983) and that of dark matter haloes (in which galaxies are believed to reside) from simulations of hot (left) and cold (right) dark matter. It is clear that the observed distribution of galaxies in the Universe has nothing to do with that envisaged by HDM models. This demonstrates how simulations of the clustering of dark matter have helped us establish the nature of the dark matter.

did not feel the shock but instead travelled with the galaxies through the merger supports the collisionless nature of this dark matter fluid.

2.2 Dark matter as a particle

We discussed several observations which require that dark matter not to be baryonic. We also argued that the dark matter is most likely a non-relativistic particle, i.e. cold. At the elementary particle physics level, such a particle cannot be accommodated within the standard model and one needs to consider extensions to it.

2.2.1 WIMPs

A popular dark matter particle candidate is the Weakly Interacting Massive Particle (WIMP). It is a non-relativistic particle in the mass range $1\mathrm{GeV} \lesssim m_\chi \lesssim 1\mathrm{TeV}$, which is thermally produced in the early Universe and that interacts via the weak force and gravity. Supersymmetry (an extension to the Standard Model) accounts for such particles, one of them being the neutralino. There are three ways one could detect WIMPs. Firstly they are hoped to be produced in a laboratory like at the Large Hadron Collider in CERN. Second, these may be detectable via interactions with underground detectors (similarly to neutrinos). Finally if they self-interact, these particles could produce gamma-rays. Some of the best sites for indirect detection of WIMP dark matter are in the dwarf spheroidals of the Milky Way which are known to be dark matter dominated objects.

2.2.2 axions

Axions are light bosons that are produced non-thermally which can be either cold, warm or hot dark matter depending on their production mechanism. In this sense, they are quite different to WIMPs and thus their observational/detection prospects will be quite different. One way to detect them is by axion-photon mixing. This is done by applying a strong magnetic field to a microwave cavity (tuned to fulfil a resonance condition $h\nu = m_\alpha c^2$, where m_α is the axion mass). In the event an axion encounters the cavity, it will decay to produce photons.

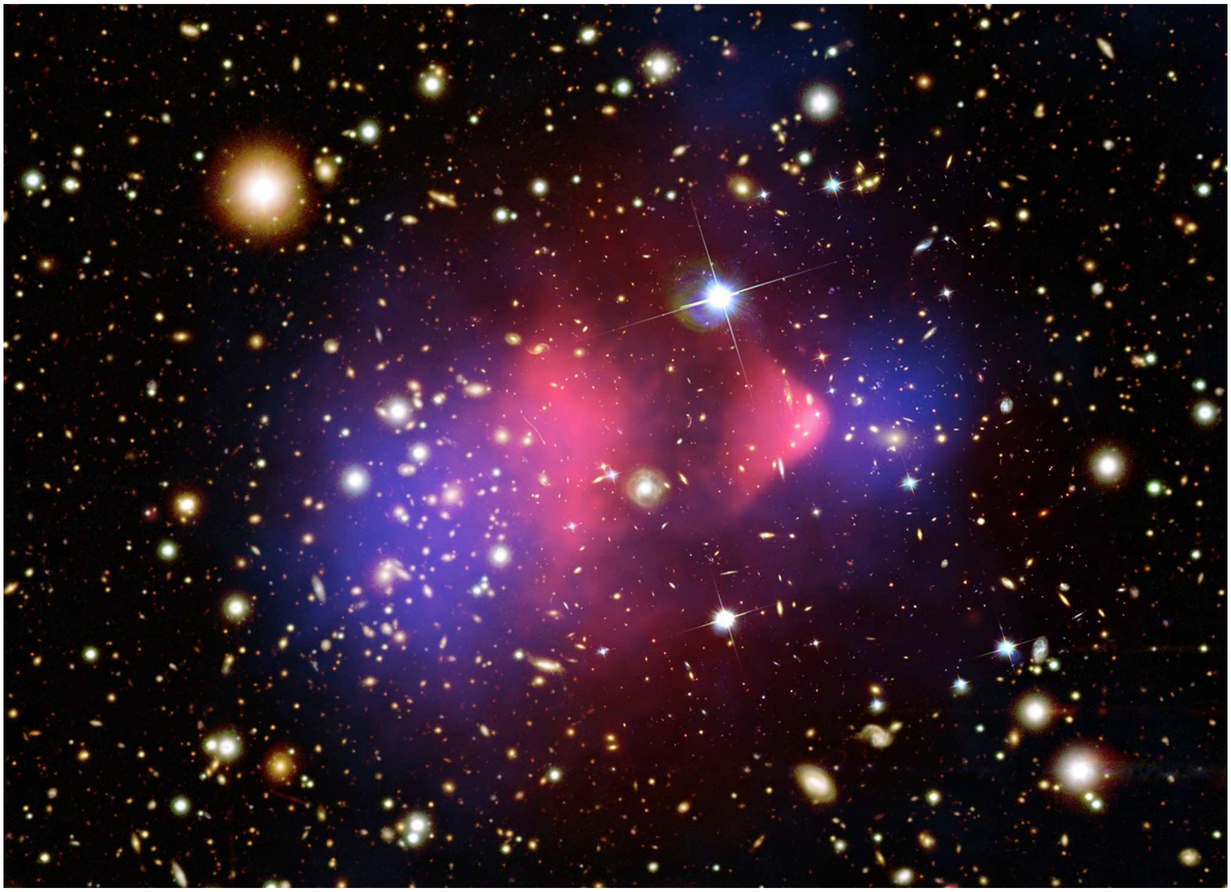

Figure 2.3: The Bullet Cluster is an ongoing collision between two galaxy clusters. The collisional gas component (in red) underwent a shock (see the clear bow shock on the right hand) and is now trapped between the two sub-groups of the cluster. The galaxies and dark matter (as traced by the weak lensing map in blue) however, are collisionless and easily pierce through. This astrophysical object supports strongly the existence of collisionless dark matter. Observations such as those and the profiles of hot electron gas in galaxy clusters can put important constraints on alternative dark matter models like collisional dark matter.

Chapter 3

Collisionless systems and the N-body method

3.1 Dynamics of collisionless systems

The dynamics of the large-scale structures and stars in a galaxy can be characterised by that of a collisionless fluid. This is because the relaxation timescale $t_{\rm relax} \sim \frac{0.1N}{\ln N} t_{\rm cross}$ (where N is the number of stars or dark matter particles and $t_{\rm cross}$ is the time needed for a stars/dark matter particle to cross the galaxy once) in these systems is exceedingly high. A collisionless fluid is characterised by its distribution function $f \equiv f(\mathbf{x}, \mathbf{v})$ (DF) and its dynamical evolution is entirely described by the Collisionless Boltzmann Equation (CBE, or also known as the Vlasov equation).

$$\frac{df}{dt} = \frac{\partial f}{\partial t} + \mathbf{v} \cdot \frac{\partial f}{\partial \mathbf{x}} - \nabla\Phi \cdot \frac{\partial f}{\partial \mathbf{v}}, \tag{3.1}$$

where Φ is the smooth potential that is generated by the collection of phase-space elements under which these move.

3.2 N-body method

Solving the CBE directly is an arduous task. However, it is possible to represent the distribution function and follow its evolution through Monte-Carlo sampling (i.e. one can represent the distribution function as a set of delta-functions in phase-space). In this way, the problem is discretised and the distribution function is said to be “coarse-grained”. One is then able to calculate the forces between every particle at each time step to describe the evolution of the system according to the CBE. This is the idea behind the N-body method and is currently the standard way of solving for gravity between multiple bodies.

In simulating the evolution of the CBE, the N-body method reduces the problem of solving a partial differential equation in seven dimensions to that of a set of ordinary differential equations describing the evolution of the phase-space coordinates $(\mathbf{x}, \mathbf{v})$ for each particle under the action of gravity:

$$\frac{\mathrm{d}\mathbf{x}}{\mathrm{d}t} = \mathbf{v}; \; \frac{\mathrm{d}\mathbf{v}}{\mathrm{d}t} = -\nabla\Phi \tag{3.2}$$

3.3 Force calculation and algorithms

The most straightforward method to calculate the gravitational force on a particle due to all its neighbours is by direct summation.

$$\mathbf{F}_{ij} = -\sum_{j \neq i} \frac{G m_i m_j (\mathbf{x}_i - \mathbf{x}_j)}{|\mathbf{x}_i - \mathbf{x}_j|^3} \tag{3.3}$$

When the collisionless fluid is discretised with particles one quickly runs into troubles due to the singularity which arises when the inter-particle distance is zero or very close to zero leading to large scattering of particles. In order to avoid such problems, one introduces a softening scale ϵ (generally specified by the mean inter-particle separation in the simulation) and calculates the gravitational force on a particle as:

$$\mathbf{F}_{ij} = -\sum_{j \neq i} \frac{G m_i m_j (\mathbf{x}_i - \mathbf{x}_j)}{(\epsilon^2 + |\mathbf{x}_i - \mathbf{x}_j|^2)^{3/2}} \tag{3.4}$$

Suitable compromised choices of softening are often invoked in order to balance between accuracy of the scale one wished to resolve and the size of the time-step one wishes to use (reference). The total time required to calculate all the forces in this pairwise operation scales as N^2, where N is the number of particles. This is problematic for most cosmological applications and one needs to find other methods to calculate the forces for which the $O(N^2)$ scaling can be reduced to $O(N \ln(N))$ or even $O(N)$. This thesis uses the GADGET code (Springel et al., 2001) and we shall describe its features in solving the N-body problem in the next section.

3.3.1 Particle mesh method

The particle mesh method computes the forces between particles by solving the Poisson equation on a grid of meshes. In this scheme, the simulation volume is divided up into a grid of M^3 meshes. The procedure is summarised in the following steps:

1. The first step is to calculate the density at each grid point according to the particle distribution. This procedure is called mass-assignment and can be done in numerous ways (nearest grid point, cloud in cell, ...).
2. The Poisson equation is solved on the grid. This is done in Fourier space. Thus the Poisson equation reads $-k^2\phi_{\mathbf{k}} = 4\pi G\rho_k$, where $\rho_{\mathbf{k}}$. The gravitational force at each grid point can then be obtained by the Fourier transform of $\mathbf{F}_{\mathbf{k}} = -\phi_{\mathbf{k}}\mathbf{k}$

3. The forces on the grid points are then interpolated at the positions of the particles.

3.3.2 Tree method

In the tree method, particles are grouped according to their distances to the particle for which the gravitational force needs to be calculated. The force from each group is then replaced by its multipole expansion. If we keep a fixed number of multipole components, the more distant particles can be grouped into larger ensembles without compromising the accuracy of the force calculation.

The computational domain is hierarchically divided into a tree structure. At the base of the tree is the *root node*. This is then subdivided into which can be sub-divided further into *branches* which are subdivided until one reaches a number of one particle per subdivision - these are called the *leaves*. There are many ways of dividing space up but a commonly used method is the *Oct-Tree* method of Barnes & Hut (1986), where each parent cube is divided into 8 equal children cubes. This is shown in Figure 3.1.

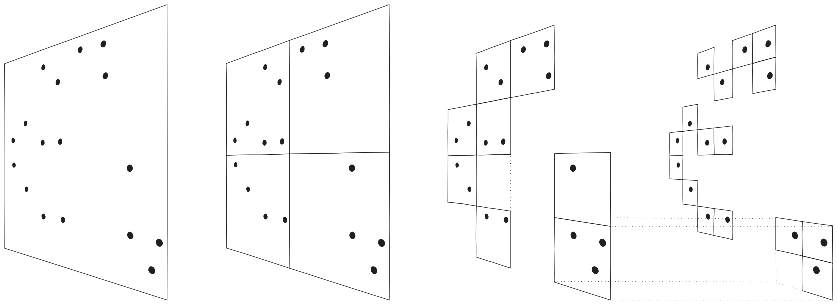

Figure 3.1: Illustration of an Oct-Tree in two dimensions. The far left shows the root which is then divided further into branches (two middle panels) which are also divided down to the leaves (last panel) which have an occupation number of one.

Once the tree is built, one evaluates the potential of each tree node as:

$$\Phi_{node}(\mathbf{r}) = -G \int \mathrm{d}^3\mathbf{x} \frac{\rho \mathbf{x}}{\sqrt{\epsilon^2 + |\mathbf{r} - \mathbf{x}|^2}}, \tag{3.5}$$

where (x) is the distance to the centre of mass of the node. The density within the node is a sum over the particles (represented by delta functions):

$$\rho_{node}(\mathbf{x}) = \Sigma \frac{m_\alpha}{\sqrt{\epsilon^2 + |\mathbf{r} - \mathbf{x}^\alpha|^2}} \tag{3.6}$$

Since $|\mathbf{r}| >> |\mathbf{x}^\alpha|$, we can Taylor expand to get the multipole expansion for the node:

$$\Phi_{node}(\mathbf{r}) = -G\Sigma m_\alpha (\frac{1}{s} + \frac{r_i x_i^\alpha}{s^3} + \frac{3}{2}\frac{r_i x_i^\alpha r_j x_j^{alpha}}{s^5} + ...) \tag{3.7}$$

One can then calculate these multipole sums for each node and sum over all nodes to obtain the force at a given point starting from the root node. This procedure of force computation is called the tree walk. In the Barnes & Hut (1986) tree walk, the multipole expansion of a node of size l is used only if $r > l/\theta$, where r is the particle node distance, l the size of the node and θ is the opening angle which controls the accuracy of the force computation. If this criterion is satisfied by a node then the tree walk along that branch is complete, otherwise the walk is continued with all its siblings.

3.3.3 TreePM method

As its name suggests the TreePM method is a hybrid between the tree and PM methods. In this scheme the small-range interactions are treated with a hierarchical tree and the long-range ones with the particle mesh algorithm. This is a popular technique used in state-of-the-art cosmological simulation codes such as GADGET Springel et al. (2001); Springel (2005).

3.4 Cosmological Simulations

The study of the evolution of the density field in the non-linear regime ($\delta \gtrsim 1$) can only be addressed by N-body techniques. The cosmological simulation of dark matter is generally carried out in a box of size L. This scale varies depending on the purpose of the simulation, but should be large enough to contain a representative volume of the Universe (e.g. a scale where the Universe is homogeneous, $L \geq 100\,h^{-1}\,\mathrm{Mpc}$, if one wishes to simulate the evolution of the dark matter density field to the present day). Periodic boundary conditions are used to account for the finiteness of the box (Hernquist et al., 1991). The generation of initial conditions can be split into two parts. The first is to set up a uniform distribution of particles to represent the unperturbed Universe. The second is to impose density perturbations with the desired properties of the cosmological model taken into consideration [1]

3.5 Initial Conditions

The first step is not a trivial task. When generating a random distribution of mass in a box of side L, one introduced white noise (i.e. $P(k) \propto k^n$ with $n = 0$) and in the absence of any other fluctuations, nonlinear objects will quickly form when running the simulation. One could instead consider creating a regular cubic lattice of particles. However this leads to strong direction preference on all scales because the grid spacing introduces a characteristic length scale on small scales. A good solution to this problem is to create a glass-like particle load proposed by White 1996 in White S. D. M. in Schaeffer et al. (1996). Particles are initially placed at random within the computational volume and then evolved by N-body integration but with the acceleration sign reversed so that the mutual gravitational forces become repulsive. The particles then settle into a glass-like distribution which has no preferred direction and the force on each particles is approximately zero.

---

[1] for a random Gaussian field this is encapsulated in the power spectrum $P(k)$ which can be computed from linear perturbation theory.

The initial density field for dark matter is a random Gaussian field [2] and thus is entirely characterised by its power spectrum $P(k)$. Thus in order to impose the density perturbations on the particle load in the simulation box, this power spectrum can be generated by using the Zel'dovich approximation to impose displacements on the particles about their unperturbed position.

3.5.1 The Zel'dovich Approximation

The Zel'dovich is another way of describing the evolution of the density field in the linear regime ($\delta < 1$) but it is particularly useful for setting up initial conditions for cosmological simulations (which we will describe in section Y). Neglecting the decaying mode, the density contrast evolves self-similarly $\delta(\mathbf{x}, t) = D(a(t))\delta_i(\mathbf{x})$. This must also hold for the peculiar velocity and the gravitational acceleration. From the Poisson equation this implies that:

$$\phi(\mathbf{x}, t) = \frac{D(a(t))}{a}\phi_i(\mathbf{x}) \text{ where } \nabla^2\phi_i(\mathbf{x}) = 4\pi G\rho a^3\delta_i(\mathbf{x}). \tag{3.8}$$

The linearised Euler equation $\dot{\mathbf{v}} + (\dot{a}/a)\mathbf{v} = -\nabla\phi/a$ can then be integrated for fixed $\mathbf{x}$ to get:

$$\mathbf{v} = -\frac{\nabla\phi_i}{a}\int\frac{D}{a}\mathrm{d}t. \tag{3.9}$$

If we integrate a second time using the fact that $\mathbf{v} = a\dot{\mathbf{x}}$ we get:

$$\mathbf{x} = \mathbf{x}_i - \int\mathrm{d}t\frac{\nabla\phi_i}{a^2}\int\frac{D}{a}\mathrm{d}t. \tag{3.10}$$

By definition, $D(a(t))$ satisfies the fluctuation growth equation $\ddot{\delta} + (2\dot{a}/a)\dot{\delta} = 4\pi G\rho\delta$ so that $\int(D/a)dt = \dot{D}/4\pi G\rho a$ and it can be shown that:

$$\mathbf{x} = \mathbf{x}_i - \frac{D}{4\pi G\rho a^3}\nabla\phi_0, \;\; \mathbf{v} = -\frac{\dot{D}}{4\pi G\rho a^2}\nabla\phi_i(\mathbf{x}) \tag{3.11}$$

This formulation of linear perturbation is due to Zel'dovich (1970). It is the Lagrangian description of the growth of structure giving the displacement $\mathbf{x} - \mathbf{x}_i$ and the peculiar velocity $\mathbf{v}$ of each phase-space element of the distribution function in terms of the initial position $\mathbf{x}_i$. Zel'dovich proposed that these equations could be used to to extrapolate the evolution of structures up to the quasi-linear regime ($\delta \sim 1$). This is the Zel'dovich approximation. In this scheme the particle trajectories are straight lines with distance traveled proportional to D.

---

[2] This is now confirmed by the Planck data which has put strong constraints on primordial non-gaussianity.

In a more compact form the Zel'dovich can be written as:

$$\mathbf{x} = \mathbf{q} - D(t)\psi(\mathbf{q}), \tag{3.12}$$

where $\mathbf{x}$ is the comoving Eulerian coordinate of a particle, $\mathbf{q}$ is the Lagrangian coordinate denoting its initial position, $D(t)$ is the growth factor of linear fluctuations and ψ is the displacement vector and describes the spatial structure of the density fluctuation.

3.5.2 Use in cosmological N-body simulations

We saw earlier that the Zel'dovich approximation is expressed as $\mathbf{x} = \mathbf{q} - D(t)\psi(\mathbf{q})$. We also know that $\psi(\mathbf{q}) = \frac{\nabla\phi_i(\mathbf{q})}{4\pi G\bar{\rho}a^3}$ and its Fourier transform can be written as $\psi(\mathbf{k}) = \frac{i\mathbf{k}\phi_i(\mathbf{k})}{4\pi G\bar{\rho}a^3} = -i\mathbf{k}\frac{\delta_i(\mathbf{k})}{k^2}$ (where we used the Poisson equation for $\phi_i(\mathbf{x})$ in Fourier space $-k^2\phi_i(\mathbf{k}) = 4\pi G\bar{\rho}a^3\delta_i(\mathbf{k})$. Using this fact, the displacement vector can be written as a discrete Fourier Transform:

$$\psi(\mathbf{q}) = \alpha \sum i\mathbf{k}c_{\mathbf{k}}e^{i\mathbf{k}\cdot\mathbf{q}} \tag{3.13}$$

where the sum is over all possible wavenumber from the fundamental mode to that of the Nyquist wavenumber. The power spectrum dependence comes in the real and imaginary parts of the Fourier components $c_k = (a_k - ib_k)/2$ which are independent Gaussian numbers with zero mean and dispersion $\sigma^2 = P(k)/k^4$.

$$a_k = \frac{\sqrt{P(k)}}{k^2}Gauss(0,1)\,;\, b_k = \frac{\sqrt{P(k)}}{k^2}Gauss(0,1). \tag{3.14}$$

To compute the displacement for each particle position, one then generates a realisation of $\{k_x, k_y, kz, c_k\}$ for the given power spectrum on a grid in Fourier space. Then one needs to FFT each of the grids to get $\psi(q)_x, \psi(q)_y, \psi(q)_z$ in real space. At this point one applies the Zel'dovich approximation to displace the particles from their Lagrangian positions ($\mathbf{q} \rightarrow \mathbf{x}$). In the case of regular grid particle load this is straightforward but for a glass one needs to use an interpolation scheme to apply those displacements correctly to the initial particle distribution. Velocities can be obtained from using $\mathbf{x} = -\dot{D}(t)\psi(\mathbf{q})$. This is a general outline and the details on setting up initial conditions can be found in Efstathiou et al. (1985). The later evolution of the dark matter density field can then be followed by integrating the equations of motion of the particles using the N-body method described earlier.

3.6 The State of the Art

Some of the first cosmological simulations which were carried out used modest particle numbers (32^3 in Davis et al. (1985)). Yet, the results obtained from such simulations were critical to assess the nature of the dark matter through its clustering properties. The direct comparison between the results from simulations assuming different kinds of dark matter particle properties with the large scale structure managed to rule out Hot Dark Matter in

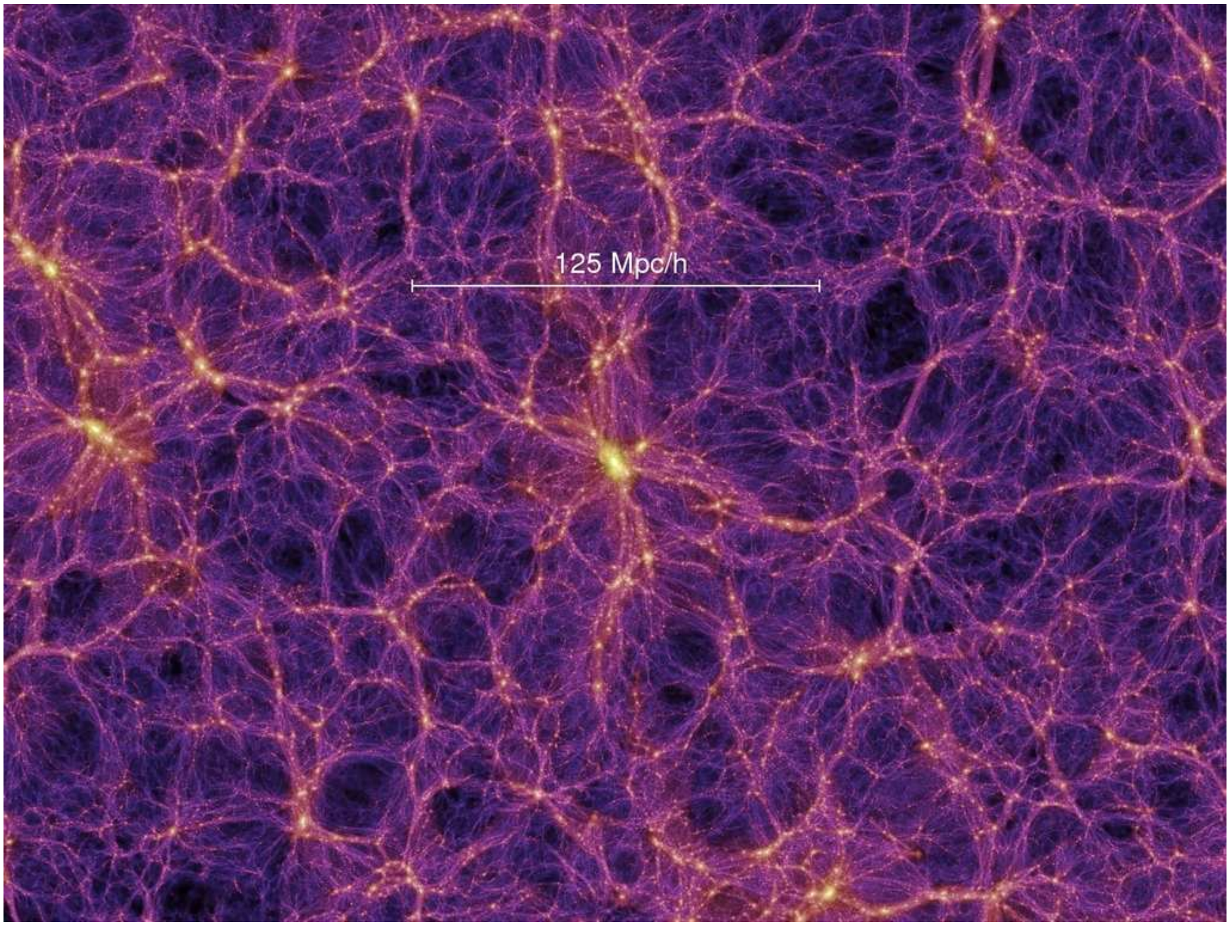

Figure 3.2: The Millennium simulation carried out by the VIRGO Consortium followed the evolution of 10 billion particles in a box of $500\,h^{-1}\,Mpc$ starting from $z = 127$ to $z = 0$. The particle mass was $m_p = 8.6 \times 10^8\,h^{-1}\,\mathrm{M}_\odot$ and the Plummer softening length was $\epsilon = 5\,h^{-1}\,\mathrm{kpc}$ It resolved virialised bound objects from galaxy clusters to a minimum dark halo mass of $1.7 \times 10^{10}\,h^{-1}\,\mathrm{M}_\odot$.

favour of Cold Dark Matter which is now at the heart of our currently favoured standard cosmological model, the ΛCDM paradigm. Over the years (with improvements in algorithm scalability and computational power) the number of particles within a given box size has dramatically increased. This has enabled cosmological N-body simulations to study the clustering of dark matter over a wide dynamic range from the large scale structures within our current Hubble radius (Angulo et al., 2012) to that of galaxies (Boylan-Kolchin et al., 2009) all the way down to dark substructures orbiting Milky Way like dark matter haloes Diemand et al. (2007); Springel et al. (2008). The *Millennium* simulation is an example of such large cosmological dark matter simulations (Springel et al., 2005) as shown in Figure 3.2.

Zoom Simulations

For some applications, it is important to resolve certain objects to much higher-resolutions such as when studying in detail the assembly of galaxy cluster or Milky Way sized dark matter haloes. Obviously by increasing the number of particles everywhere in an entire cosmological simulation box only makes the task more difficult. One technique that is widely used is the zoom-in method. First, one identifies an object of interest (e.g. galaxy cluster, Milky Way like dark matter halo, a void) within a large cosmological box for re-simulation. One then tracks all the particles within a certain volume associated with the object of interest and tracks their position back to their initial conditions and define a Lagrangian volume at z_{init}. At this point one increases the number of particles in that region (thus lower the mass of the particles) and keep the regions outside this volume to the same initial resolution of the simulation. This technique was pioneered by Navarro & White (1994) and is a common method to run zoom-in simulations of individual objects. The simulations presented in this thesis were set-up in such a way.

Part II

Brightest Cluster Galaxies and the distribution of dark matter in galaxy clusters and the dwarf spheroidals

Chapter 4

Shallow Dark Matter Cusps in Galaxy Clusters

4.1 abstract

We study the evolution of the stellar and dark matter components in a galaxy cluster of $10^{15}\,\mathrm{M}_{\odot}$ from $z = 3$ to the present epoch using the high-resolution collisionless simulations of Ruszkowski & Springel (2009). At $z = 3$ the dominant progenitor halos were populated with spherical model galaxies with and without accounting for adiabatic contraction. We apply a weighting scheme which allows us to change the relative amount of dark and stellar material assigned to each simulation particle in order to produce luminous properties which agree better with abundance matching arguments and observed bulge sizes at $z = 3$. This permits the study of the effect of initial compactness on the evolution of the mass-size relation. We find that for more compact initial stellar distributions the size of the final Brightest Cluster Galaxy grows with mass according to $r \propto M^2$, whereas for more extended initial distributions, $r \propto M$. Our results show that collisionless mergers in a cosmological context can reduce the strength of inner dark matter cusps with changes in logarithmic slope of 0.3 to 0.5 at fixed radius. Shallow cusps such as those found recently in several strong lensing clusters thus do not necessarily conflict with CDM, but may rather reflect on the initial structure of the progenitor galaxies, which was shaped at high redshift by their formation process.

4.2 Introduction

Brightest cluster galaxies (BCGs) are the most massive elliptical galaxies in the Universe at the extreme end of the galaxy luminosity function and perhaps “special” (see Paranjape & Sheth, 2012). These objects are intriguing because they do not follow the same scaling relations as normal giant ellipticals. Using the Sloan Digital Sky Survey (SDSS), von der Linden et al. (2007) found that BCGs deviate systematically from the Faber & Jackson (1976) and the Kormendy (1977) relations with lower velocity dispersions and larger sizes respectively. Early theoretical studies investigated the role of cooling flows (Fabian, 1994) in BCG formation. This hypothesis is disfavoured by observations with Chandra and XMM-Newton which show that such flows are much weaker than required, as are the star formation rates in the central galaxies of clusters (McNamara et al., 2000; Fabian et al., 2001). Another scenario has BCGs growing by feeding on smaller galaxies (minor mergers). This is the notion of galactic cannibalism (Ostriker & Hausman, 1977; Hausman & Ostriker, 1978).

In the ΛCDM scenario, structures build-up hierarchically through accretion and mergers of smaller progenitors. Groups form before clusters and have sufficiently low relative velocities that galaxy-galaxy mergers can occur before cluster formation, thus enhancing the formation of a massive central galaxy. De Lucia & Blaizot (2007) use semi-analytic galaxy formation models to show that in the ΛCDM cosmology, BCGs form primarily through in-situ star-formation at high redshifts, $z \geq 3$, with subsequent mass growth dominated by non-dissipational merging. Similar processes are seen in hydrodynamical cosmological simulations of massive galaxy formation (Naab et al., 2009; Oser et al., 2012a; Feldmann et al., 2011) although these are typically less effective at suppressing star formation at late times than semi-analytic models, leading to galaxies which are "younger" than those observed.

From this, it seems that many aspects of the late assembly of BCGs can be modelled without considering the early star formation phase. Dubinski (1998) was an early example of such work based on numerical N-body simulations of collisionless mergers of galaxies in a cosmological context. Dubinski found that the properties of cluster BCGs can be naturally explained by merging of galaxies which have already formed their stars at high redshift. This idea was further investigated by Ruszkowski & Springel (2009) (RS09) who studied the deviations of BCGs from the Kormendy and FJ relations in a ΛCDM simulation.

In relaxed clusters, BCGs reside at the bottom of the potential well, making them ideal probes of the distribution of dark matter from kpc to Mpc scales. Sand et al. (2002, 2004, 2008) studied a selection of clusters combining stellar dynamical modelling and strong gravitational lensing in order to infer the inner slope of the dark matter density profiles. Their studies found values for the logarithmic slope of the dark matter density profile $\gamma = -d\ln(\rho)/d\ln r < 1$, at odds with the predictions of dark-matter-only simulations of halo formation which generally follow the NFW profile with $\gamma_{\rm NFW} = 1$ (Navarro et al., 1997). More recently, Newman et al. (2011) revisited the study of Abell 383 by Sand et al. (2008), combining stellar kinematics, strong and weak lensing and X-ray data to deduce an inner slope of $\gamma = 0.59^{+0.30}_{-0.35}$ at 95 percent confidence. These authors suggest this may indicate a genuine problem with our understanding either of baryonic evolution or of the nature of the dark matter.

Indeed, some recent hydrodynamical simulations of galaxy formation in clusters indicate a steepening of the inner-slope of the dark matter profile (Gnedin et al., 2004, 2011; Sommer-Larsen & Limousin, 2010), exacerbating the core-cusp problem . More gentle contraction is seen in other simulations (e.g. Duffy et al., 2010) but not on the scales investigated by Newman et al. (2011). A simulation in which dynamical friction significantly erodes the cusp at the center of ellipticals was presented by Johansson et al. (2009) but on the scale of the central galaxy of a small group. However, the final masses of the central galaxies in these simulations are in general a factor of two or three higher than expected from abundance matching arguments (Guo et al., 2010; Moster et al., 2010; Behroozi et al., 2010), implying the need for a signicantly improved treatment of baryonic astrophysics. El-Zant et al. (2004) claimed that shallower cusps could be produced in a cluster through dynamical heating by the galaxies. However, they treated galaxies as unstrippable point masses which is too unrealistic to address the issue in quantitative detail.

At this stage it still seems interesting to address the second question by Newman et al. (2011): is the presence of shallow dark matter cusps at the centre of clusters a significant challenge to CDM? We use the RS09 simulation to test whether such cusps can be created through dry (i.e., gas-free) mergers. Recent observations of massive ellipticals at $z = 2$ have shown that they were more compact than similar mass galaxies today (see e.g. van Dokkum et al., 2008). Dry, predominantly minor mergers have also been proposed as a possible mechanism to drive the required size evolution (e.g., Naab et al., 2009; Bezanson et al., 2009)

In this context a significant limitation of the RS09 simulations was that the galaxies they inserted at $z = 3$ had stellar masses an order of magnitude larger than expected from abundance matching arguments (Moster et al., 2010) and were assumed to follow the present-day mass-size relation. Here we remedy the inconsistencies between the simulations and observations by using a method that re-assigns the mixture of stellar and dark matter in each simulation particle. This enables us to study the evolution of stellar and dark matter distributions for different levels of initial compactness and stellar mass.

In Section 2, we give a description of the simulations as well as of the weighting scheme used in this study. We also present results on the mass and size growth of the BCG for different initial assignments of stars and dark matter. In Section 3, we look at how the initial slope of the dark matter evolves from $z = 3$ to the present. We discuss our results and conclude in Section 4.

4.3 Numerical Methods

4.3.1 Simulation

The simulations used for this study are described in detail in Ruszkowski & Springel (2009), (RS09) and we give only a short summary here. A cluster mass dark matter halo of $10^{15}\,\mathrm{M}_\odot$ was identified in the *Millennium Simulation* (Springel et al., 2005). The cosmological parameters of this simulation are $\Omega_m = 0.25$, $\Omega_\Lambda = 0.75$, a scale-invariant slope of the power spectrum of primordial fluctuations ($n = 1.0$), a fluctuation normalization $\sigma_8 = 0.9$, and a Hubble constant $H_0 = 100\,h\,\mathrm{km\,s^{-1}\,Mpc^{-1}} = 73\,\mathrm{km\,s^{-1}\,Mpc^{-1}}$.

The cluster was then re-simulated using a zooming technique with a mass resolution of $m = 1.57 \times 10^7 h^{-1}\,\mathrm{M}_\odot$ and comoving softening length $\epsilon = 2.0\,h^{-1}\,\mathrm{kpc}$. At redshift $z = 3$, the 50 most massive progenitors of the final cluster were identified and replaced by spherical equilibrium models in which stars were distributed according to a Hernquist

(1990) profile embedded in a NFW dark matter halo (Navarro et al., 1997). The masses of the dark matter and star particles were set to be identical $m_{dm} = m_* = 1.57 \times 10^7 \, h^{-1} \, \mathrm{M}_\odot$ and they were assigned a softening length of $\epsilon = 1 \, h^{-1}$ kpc. comoving, half that of the other dark matter particles from the original resimulation. Throughout this paper we use $h = 0.73$ and our mass and length units are thus in kpc and $\mathrm{M}_\odot$.

Two simulations were run with different initial galaxy models: one in which the dark matter was adiabatically contracted following Blumenthal et al. (1986) and one where it retained an undisturbed NFW profile. We shall refer to these as models A and B respectively. The Blumenthal et al. (1986) formalism over-predicts the amount of contraction observed in many hydrodynamical simulations (Gnedin et al., 2004), however through the inclusion of uncompressed and compressed dark halo models, we can probe two alternative regimes. If dry-merging is indeed the main driver in the late assembly of BCGs and if the RS09 initial galaxies were realistic, then the "real" solution would lie between these two models.

In fact, however, the galaxies which RS09 inserted at redshift $z = 3$ followed the *present-day* mass-size relation from Shen et al. (2003) and assumed a stellar to dark matter mass ratio $m_*/M = 0.1$. This value is too large by a factor of 10 according to recent results from matching the observed high-redshift abundance of massive galaxies (Moster et al., 2010; Behroozi et al., 2010; Wake et al., 2011). We note that many other simulations investigating similar processes have like-wise assumed over-massive stellar components (e.g., Nipoti et al., 2009; Rudick et al., 2011). However, we point out that for a given mass resolution, more massive stellar bulges are represented by a larger number of particles which considerably improves the numerical convergence of the simulations.

Not surprisingly, the final merger remnants in RS09 were also too massive $m_* \sim 10^{13} \, \mathrm{M}_\odot$ with half-mass radii which were too large (~ 100 kpc) compared to real BCGs. These generally do not exceed $r_e \sim 50$kpc (Bernardi et al., 2007).

In order to study more consistently the change in the slope of dark matter density profiles at the centre of ΛCDM clusters, we need to address the question with galaxies that have stellar properties consistent with observations. We also need to test whether the final stellar mass of the merger remnant agrees with the stellar to halo mass relation (SHM) at $z = 0$ (Guo et al., 2010; Moster et al., 2010; Behroozi et al., 2010). We employ a weighting procedure to re-assign the luminous component of every initial galaxy such that only one percent of its total dark matter mass is locked in stars. For the range of halo masses ($10^{13} \, \mathrm{M}_\odot - 10^{12} \, \mathrm{M}_\odot$) that we populate, abundance matching implies that this ratio is rather constant. Additionally, our weighting scheme enables us to change the sizes of the luminous components to study the assembly of the BCG for different levels of compactness while keeping the total initial stellar mass fixed. We present this scheme in the next section.

4.3.2 Weighting Scheme

Here we describe our method for re-assigning simulation particles in the initial conditions so that the light to stellar mass ratio and the size of the luminous component of a galaxy can be varied. Our scheme is similar to that of Bullock & Johnston (2005) and is applicable

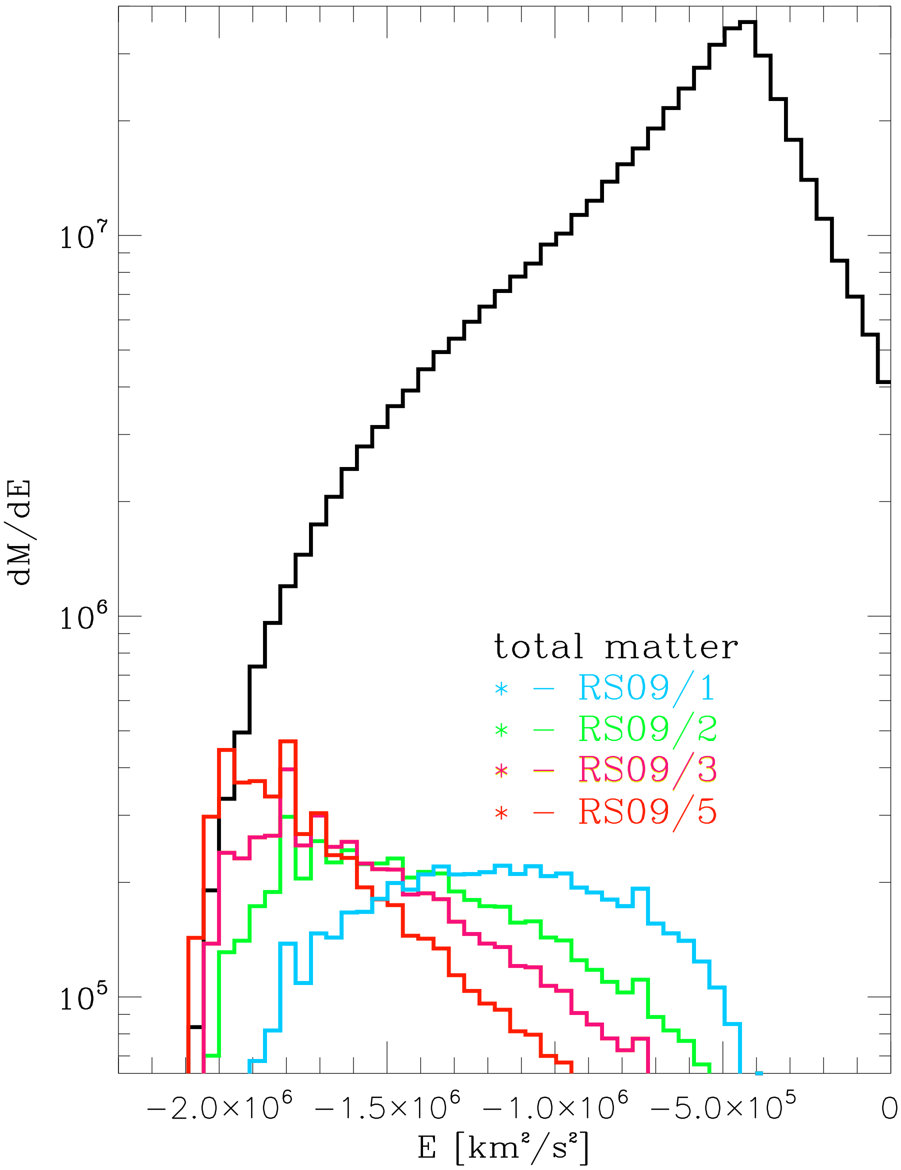

Figure 4.1: Differential energy distribution for the proto-BCG for the total mass and light contributions for three test cases $r_e = r_{e_{\mathrm{RS09}}}/1, r_{e_{\mathrm{RS09}}}/2, r_{e_{\mathrm{RS09}}}/3, r_{e_{\mathrm{RS09}}}/5$. Although the $r_{e_{\mathrm{RS09}}}/5$ histogram intersects the total differential energy distribution, the particles in those energy bins are below our spatial resolution of $\epsilon = 1\,h^{-1}\,\mathrm{kpc}$.

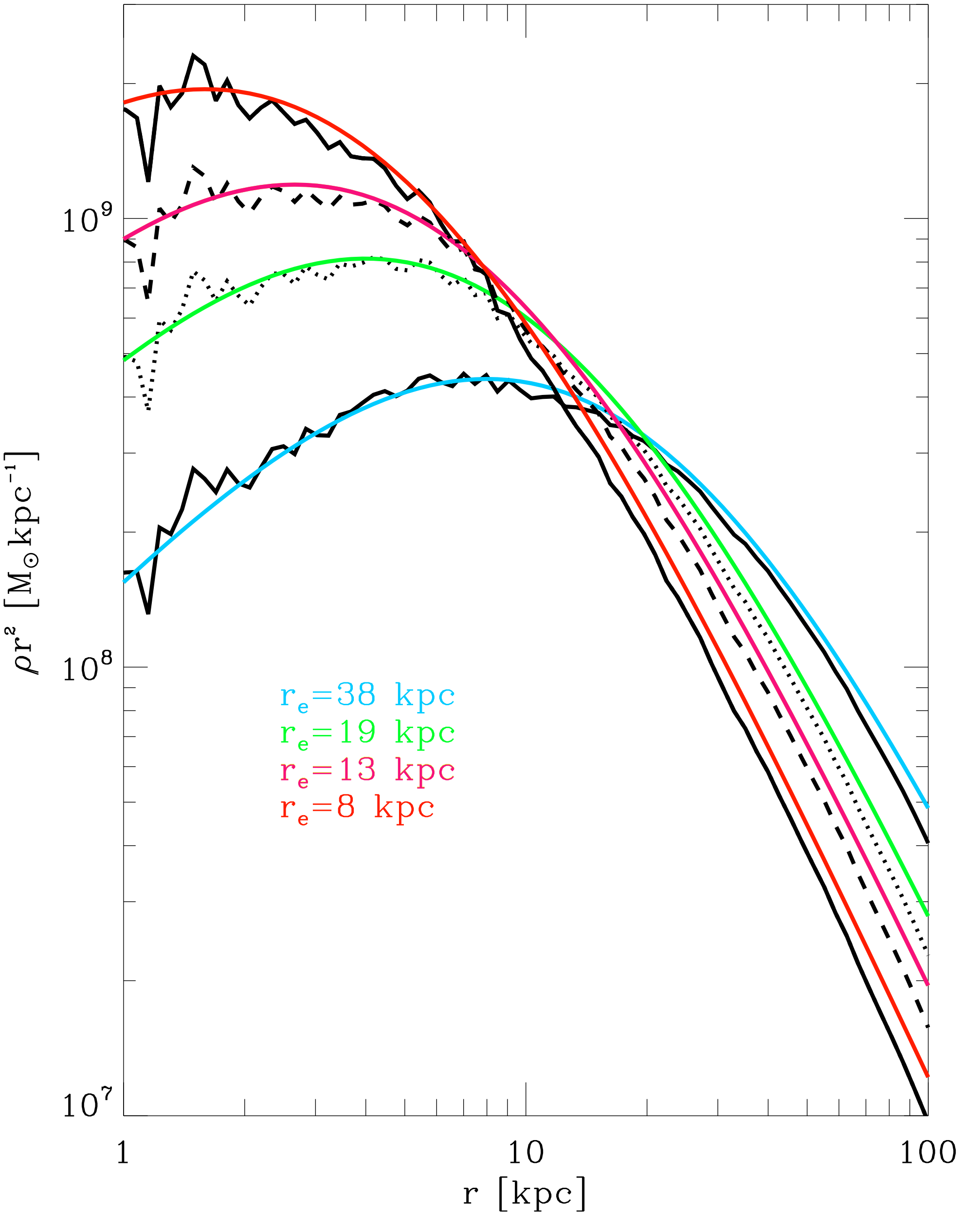

Figure 4.2: ρr^2 profiles vs. radius for the four different realisations. The target functional forms of each realisation are overplotted in solid colored lines.

to spherically symmetric density distributions. A galaxy is represented by a distribution of N particles of mass $M_{\rm tot}/N = m_p$ and phase-space coordinates $(\mathbf{x}, \mathbf{v})$ which generate the potential $\Phi = \Phi_{\rm dark} + \Phi_{\rm stellar} = \Phi_{\rm NFW} + \Phi_{\rm Hernquist}$. Each particle of energy $E = \frac{1}{2}v^2 + \Phi$ now simultaneously represents dark matter and stars in different amounts according to a weight function $\omega(E) = f_*(E)/f(E)$. This is the ratio between the stellar distribution function (DF) and the total DF. One can construct the stellar DF in the following way.

In computing $f_*(E)$, one assigns the particles a spherical number density distribution $\nu(r)$ and solves the Eddington inversion formula:

$$f_*(\mathcal{E}) = \frac{1}{\sqrt{8}\pi^2} \int_0^{\mathcal{E}} \frac{d\Psi}{\sqrt{\mathcal{E} - \Psi}} \frac{d^2\nu(\Psi)}{d\Psi^2} + \frac{1}{\sqrt{\mathcal{E}}} \frac{d\nu}{d\Psi}\bigg|_{\Psi=0}, \tag{4.1}$$

where $\Psi = -\Phi + \Phi_0$ and $\mathcal{E} = -E + \Phi_0 = \Psi - v^2/2$ are the relative potential and total energies respectively. The potential used to generate the model galaxies in RS09 was a linear combination of a Hernquist and an NFW potential, both of which tend to zero in the limit r goes to infinity thus $\Phi_0 = 0$. We choose $\nu(r)$ to follow a Hernquist profile (1990):

$$\nu(r) = \frac{a}{r(r+a)^3}. \tag{4.2}$$

The total DF is the ratio of the differential energy distribution $N(E) = dM/dE = f(E)g(E)$ and the density of states $g(E)$ which is solely defined by the potential Φ:

$$g(E) = (4\pi)^2 \int_0^{r_E} r^2 \sqrt{2(E - \Phi(r))}dr. \tag{4.3}$$

Since $\Phi(r)$ and $N(E)$ can both be measured directly from the simulation's initial condition, this determines $f(E)$.

Note that the only free parameter we have introduced is the scale radius a for the light distribution which is related to the half-light radius by $a = r_e/(\sqrt{2} + 1)$. Within certain limits we can vary the relative mixture of dark and luminous matter to represent, for example, less massive and more compact bulges. This has the advantage of allowing us to study aspects of the assembly of massive galaxies from $z = 3$ to $z = 0$ without having to run additional CPU intensive simulations, simply by tracking the weights to the final merger remnant. This scheme allows multiple interpretations of a single simulation. However, for our purposes the stellar mass within each galaxy is kept fixed, its value being dictated by abundance matching arguments, so it is the stellar and dark matter distributions which vary with the total mass distribution held fixed. Note that this implies that the initial dark matter distributions in the adjusted galaxies are no longer those expected naturally in ΛCDM. Thus while we can address issues of how the mixing of the two components changes inner profile shapes and is affected by initial compactness, we cannot expect the final DM distributions to be realistic.

Figure 1 shows the differential energy distribution for the most massive of the $z = 3$ galaxies (the dark halo and stars of the main BCG progenitor) as a function of energy.

Overplotted are stellar differential energy distributions for four reinterpretations with different galaxy sizes: the original effective radius used in RS09 and the same reduced by factors of two, three and five. To show more explicitly that our method works we present ρr^2 profiles in Figure 2. Note that changing the sizes of the stellar component for a fixed $m_*/M_{\rm halo}$ ratio, implies substantial changes in the inner slope of the dark matter profile. The reduction of the stellar mass by a factor of 10 from that assumed in RS09 also means that both the uncontracted and contracted models now have overly concentrated dark matter distributions in the centres of the galaxy subhalos, except at very small radii where the reduced radii can lead to an increase of stellar density relative to RS09.

The maximum extent to which we are able to rescale the stellar component is set by the total mass profile. This is saturated by the stars alone at the softening radius if the RS09 sizes are reduced by a factor of ~ 5 (see Figure 1).

The initial and final light profile shapes in the RS09/1 interpretation will be the same as in the original simulation, as only the stellar masses of every galaxy are changed (the inner dark matter profiles will differ, however, since they now contain the additional mass which used to be assigned to stars). This also means that the galaxies no longer lie on the Shen et al. (2003) stellar mass-size relation. In order to put them back on it (within the scatter) we need to reduce the sizes by factors of ~ 5.

Recent observations show, however, that $z = 2$ elliptical galaxies were more compact than implied by the local relation (van Dokkum et al., 2008). Unfortunately, our spatial resolution limit does not permit us to consider such small sizes. We stress that these observations still need to be treated with caution as the galaxy stellar masses are estimated photometrically. Martinez-Manso et al. (2011) argue that dynamical masses of compact galaxies at redshift $z = 1$ may be six times lower than some photometric estimates. Nevertheless if the photometrically determined stellar masses of galaxies at redshift $z = 2$ are even approximately correct, the galaxies should be even smaller than we assume in this paper. As we will see, the exercise presented here can nonetheless give insight into the puffing-up of BCGs by minor mergers and its dependance on the initial compactness of the galaxies.

4.3.3 Results for the BCG evolution

Size growth of the BCG

Fixing the stellar masses within all haloes according to abundance matching arguments (and hence reducing them by an order of magnitude from those originally assumed by RS09), we studied four assumptions for the compactness of the galaxies $r_e = r_{e_{\rm RS09}}/1$, $r_{e_{\rm RS09}}/2$, $r_{e_{\rm RS09}}/3$, $r_{e_{\rm RS09}}/5$ in each of our two simulations. The trends arevery similar in the two models. We find that the relative growth in size of the BCG from $z = 3$ to $z = 0$ is not identical for different assumptions about initial concentration. This is illustrated in Table 1, where we give the growth factors as characterised by the increase in half-light radius. The size of the BCG at $z = 0$ in the original RS09 simulations was high by a factor of two compared to local BCGs. However, in the RS09/5 case, the sizes of the initial galaxies correspond to those of low-redshift largest ellipticals of similar stellar mass (within the scatter of the Shen et al. 2003 relation) and the most massive BCG progenitor grows by a factor of 4, reaching a size that is in reasonable agreement with observed BCGs. This supports the idea that massive ellipticals can grow rapidly in size through repeated minor mergers in a cosmological context (Naab et al., 2009; Oser et al., 2010, 2012a; Shankar et al., 2011).

Mass growth of the BCG

Turning to the mass growth of the BCG, the main progenitor starts with a stellar mass of $\sim 2.5 \times 10^{11}\mathrm{M}_{\odot}$ at $z = 3$ and the final merger remnant at $z = 0$ has a total stellar mass of 6 to $7 \times 10^{11}\mathrm{M}_{\odot}$. For the cluster mass we are considering here ($\sim 10^{15}\,\mathrm{M}_{\odot}$), abundance matching suggests $m_*/M_{\mathrm{halo}} = 0.001$ (see Fig. 2 of Guo et al. (2010)). Considering that semi-analytic models predict that 80 percent of the stars which end up in a BCG are already formed by $z = 3$ (De Lucia & Blaizot, 2007) our value of $m_*/M(z = 0) = 0.0006$ is a considerable improvement over the value prior to rescaling ($m_*/M(z = 0) \sim 0.01$). We note that this factor is still somewhat lower than expected from semi-analytic models. A quick query in the Millenium database indicates that only 30 percent of the stars in the $z = 0$ BCG in the cluster come from the 50 most massive progenitor haloes at $z = 3$. The missing contribution comes from smaller subhaloes which were not populated with stars in the simulation. Figure 3 shows the normalised radial distribution of simulation BCG stars coming from different galaxies at $z = 0$. The two panels illustrate the process of mass aggregation for two extreme interpretations (RS09/1 and RS09/5). The stars coming from the proto-BCG (in-situ) are represented by the solid black line and those accreted from other galaxies by the dashed-dotted line. Contributions from individual galaxies are shown by coloured lines. Between $z = 3$ and $z = 0$ the BCG was subjected to two mergers with mass ratios of about 3:1 and six with about 10:1. These are responsible for the inside out growth of the BCG.

For the most compact galaxy interpretation (RS09/5), 30 percent of the BCG mass comes from accretion which dominates beyond $\sim$ 30kpc. This is in contrast with the extended galaxy (RS09/1) where this transition occurs at 60kpc. Note that little of the accreted mass reaches the centre. Most gets deposited on the outskirts leading to inside-out growth.

The reason why the mass growth factor decreases with increasing compactness is that the initial compact galaxies have more stars on higher binding energy orbits than their less compact counterparts (as can be seen in Figure 1). These stars are harder to unbind. Thus, as encounters take place, less stellar mass is stripped and deposited on the BCG. More remains bound to the original galaxies.

Another interesting aspect of our numerical experiment is the scaling between total stellar mass and effective radius. For the most extended galaxies, the BCG radius and mass scale as $r_e \propto M$. For the compact galaxies in the RS09/5 interpretation this scaling is almost $r_e \propto M^2$. This latter scaling agrees with van Dokkum et al. (2010) who studied the growth of compact galaxies at fixed number density finding $r_e \propto M^{2.04}$. Thus for

Run	r_e/kpc	r_{e_f}/r_{e_i}A	M_f/M_iA	r_{e_f}/r_{e_i}B	M_f/M_iB
RS09/1	38	2.7	2.9	2.5	2.9
RS09/2	19	3.2	2.7	3.0	2.6
RS09/3	13	3.6	2.5	3.1	2.5
RS09/5	8	4.3	2.4	3.8	2.4

Table 4.1: Initial half-light radii r_{e_i}, size and mass growth factors (defined as the ratio of initial and final half-light radii and stellar masses) for the eight interpretations. The initial stellar mass of the largest BCG progenitor is $2.5 \times 10^{11}\mathrm{M}_\odot$ in all cases.

smaller sizes, we get a stronger size evolution in better agreement with observation. Seeing that our weighting scheme produces central galaxies with appropriate stellar masses for their host dark halo, we now address the issue of the change in inner slope of the dark matter profile in the presence of a baryonic component, and how this varies depending on the relative distribution of stars and dark matter.

4.4 Evolution of the dark matter slope

4.4.1 Methodology

In relaxed clusters, BCGs are usually coincident with the centre of the cluster, defined theoretically as the bottom of its gravitational potential well and empirically as the centre of the X-ray emitting hot gas. Thus we define the centre of the galaxy (BCG) and cluster as the position of the particle with the minimum potential identified by the SUBFIND algorithm (Springel et al., 2001).We then compute density profiles in spherical shells around this centre, using 44 bins spaced logarithmically between 0.1kpc and 2500kpc. The intrinsic slopes of the density profiles are computed by numerical differentiation using a 3-point Lagrangian interpolation as in Navarro et al. (2010).

4.4.2 Results for the original RS09 simulations

We begin by analysing the simulations as originally presented in RS09. In Figure 4, we present the intrinsic logarithmic slope $\gamma = -d\ln(\rho)/d\ln r$ as a function of radius r for the dark matter (red dashed lines) and for the total matter (solid black lines). The dashed horizontal line $\gamma = 1$ marks the asymptotic value that the NFW profile should reach as $r \to 0$. Results are given for the main BCG progenitor at $z = 3$ in the left panels and the final BCG at $z = 0$ in the right panels. The upper panels are for run A (contracted) and the lower panels for run B (uncontracted). The BCG progenitors at $z = 3$ have inner slopes of $\gamma \sim 1.3$ and $\gamma \sim 1$ at 5 kpc for the dark matter in the contracted and uncontracted models, respectively. In the final systems at $z = 0$ these latter inner slopes reach $\gamma \sim 0.9$ and $\gamma \sim 0.8$. These are depressions of $0.2 < \Delta\gamma < 0.4$ with respect to the initial slope at this radius. However, as already noted these initial conditions are inconsistent with

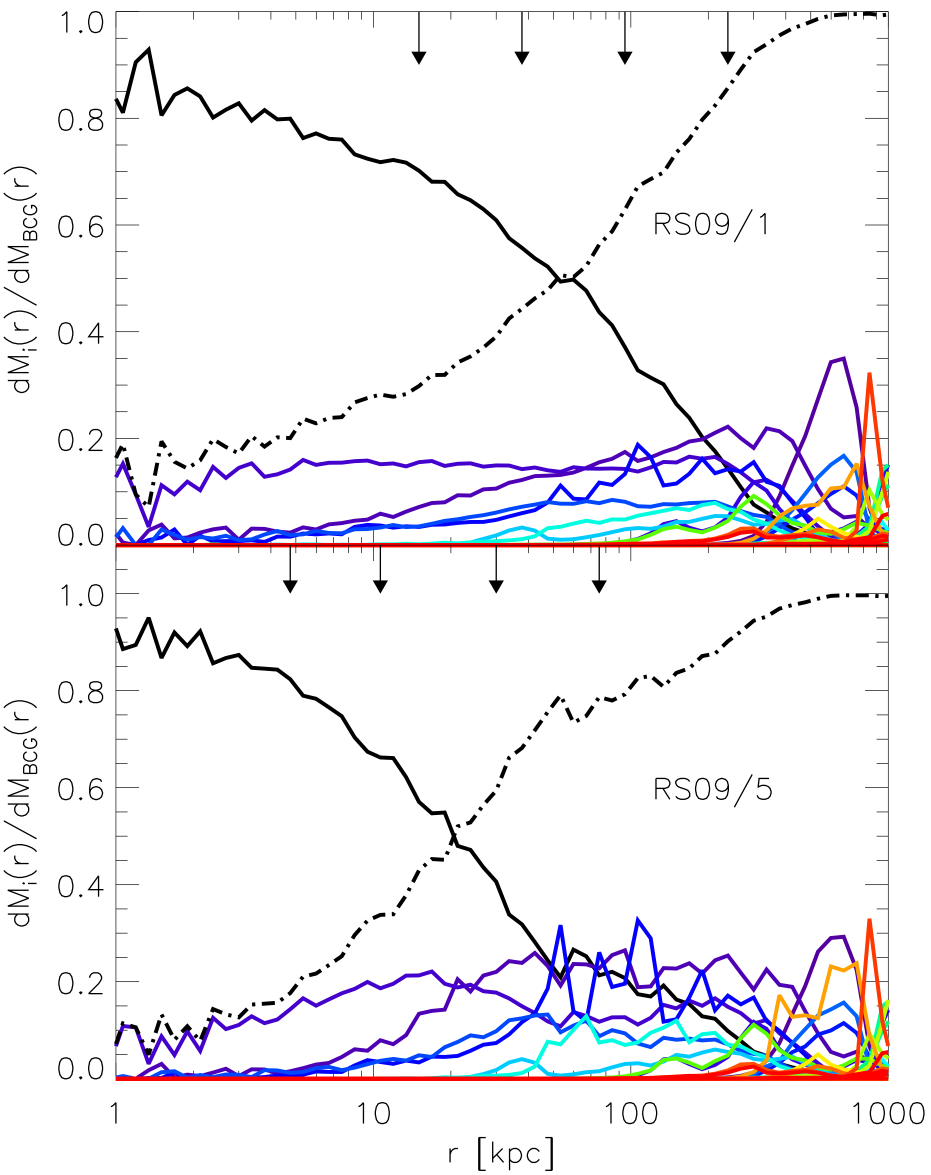

Figure 4.3: Normalised radial distribution of stellar mass in the $z = 0$ BCG coming from different contributing galaxies for model A (each colour). The solid line shows the stars coming from the largest progenitor, taken to be the proto-BCG (in-situ). The dashed-dotted line is the radial distribution of stellar mass contributed by accreted galaxies. The top and bottom panels show the results for two interpretations (RS09/1 and RS09/5). In the RS09/5 case, accreted material contributes 50 percent of the mass budget already at 30 kpc while this occurs at 60 kpc for the RS09/1 case. The arrows point out the radii containing 10, 25, 50 and 75 percent of the BCG stars.

observations of $z = 3$ galaxies assuming a ΛCDM universe. The behaviour here merely serves to prove that collisionless evolution can reduce the slope of the inner dark matter profile. We still need to test whether this holds for galaxies with more realistic initial configurations, so we turn to results from our weighting scheme.

4.4.3 Dark matter slope evolution for other BCG stellar mass profiles

Figure 4 shows the initial and final slopes of the dark matter density profiles for each of our reinterpretations of the two simulations using the weighting scheme presented above. The total mass does not of course change from one interpretation to another, only the partition between stellar and dark matter distributions does. Because we have decreased the stellar mass by a factor of ten, the dark matter mass increases to compensate. The distribution of the dark matter varies however, according to the concentration we assume for the stellar mass. In the RS09/1 interpretation, there is additional dark matter at all radii and γ becomes more negative for the dark matter everywhere. In the RS09/5 interpretation however, stars are much more concentrated which results in a shallower initial slope near the centre. The slopes of the dark matter profiles retrieved from the weighting scheme are represented by the solid coloured lines.

The initial dark matter profiles in each interpretation differ from each other in the inner regions where stars contribute significantly to the mass budget ($5-10$ kpc) and asymptote to the same profiles at larger radii. At $z = 3$, the slopes in model A range from $\gamma \sim 1.4$ to 1.0 at 5 kpc, and $\gamma \sim 1.6$ to 1.5 at 10 kpc between RS09/1 and RS09/5. At $z = 0$ the final slopes take values $\gamma \sim 0.5$ to 1.0 at 5 kpc and $\gamma \sim 1.2$ to 1.0 at 10 kpc. These are changes with respect to the initial slopes of $0.4 < \Delta\gamma < 0.5$ at both 5 kpc and 10 kpc. Note that in a few cases (RS09/4 and RS09/5 model A) the final slopes are already shallower than $\gamma = 1$ below 10 kpc, a region of interest for observations using stellar kinematics.

For our model B, at $z = 3$ the slopes range from $\gamma \sim 1.3$ to 1.0 to $\gamma \sim 1.6$ to 1.4 at 5 and 10 kpc respectively. At $z = 0$ we also observe significant changes in the inner-slope between $0.3 < \Delta\gamma < 0.4$ and $0.4 < \Delta\gamma < 0.6$ at 5 and 10 kpc. We caution that interpretation RS09/5 has a steep slope profile and that for this particular interpretation the slope change is much more significant $\Delta\gamma \sim 0.7$.

Thus, we see that the various mergers between galaxies not only change the slopes of the total matter density profiles but also those of the dark matter profiles. We show that even when baryons account for just one percent of the total mass of a galaxy, in agreement with recent abundance matching results, their effect is still significant enough to have an impact on the scales probed by observations, making initial cusps shallower. In the new interpretations, the changes in the slope are more localised to the inner regions ($5-10$ kpc) of the galaxy when compared to results from the original RS09 simulations where the slope was shallower than $\gamma = 1$ out to ~ 30 kpc for model B.

Aspects of this evolution are present in the explanation proposed by El-Zant et al. (2004) for the shallow slopes measured by Sand et al. (2004): dynamical friction as the

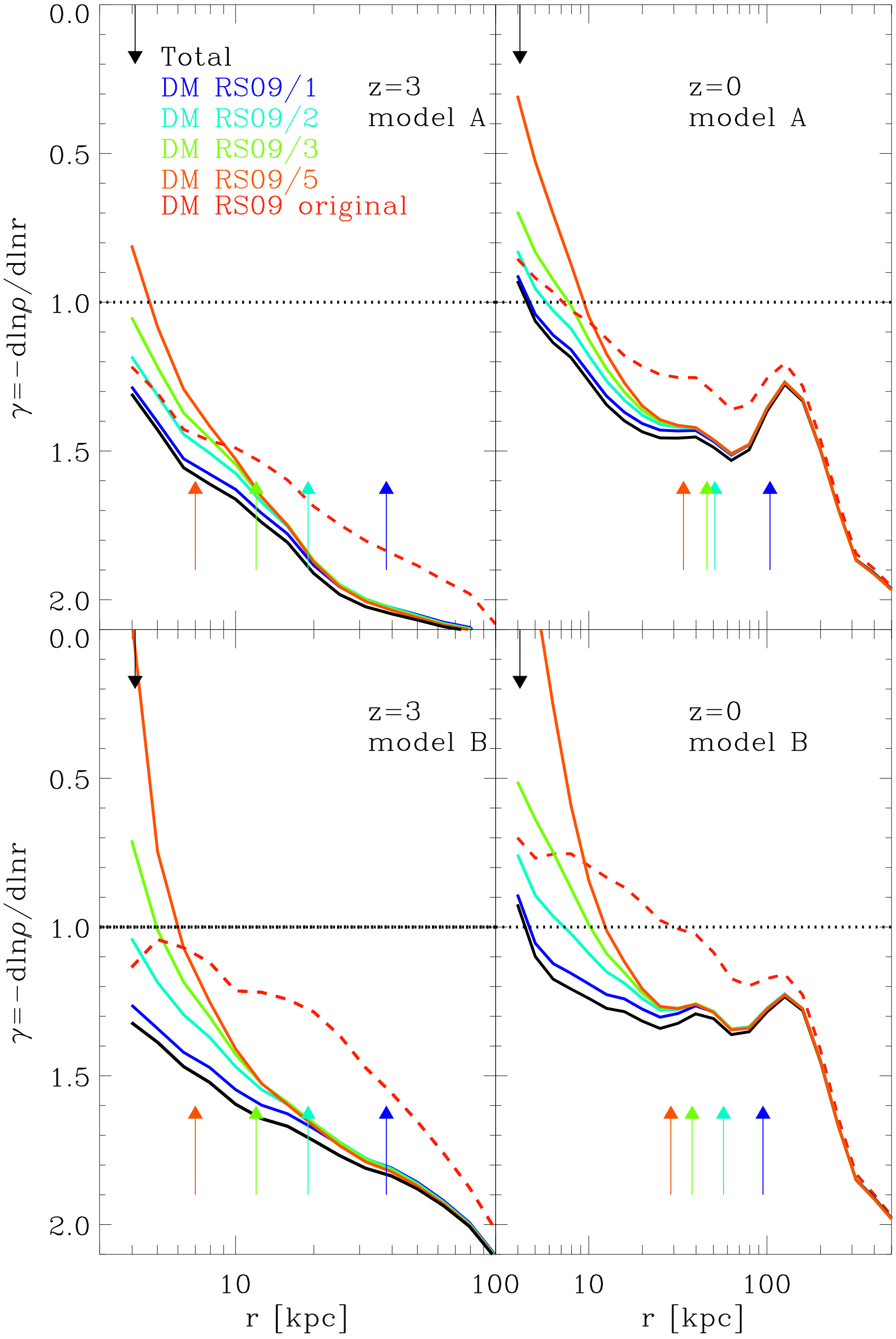

Figure 4.4: Slopes of the total matter and dark matter profiles at $z = 3$ and $z = 0$ for the four interpretations and for the original RS09 simulations. The top and bottom panels show results for models A and B respectively. The dashed red line is the slope of the dark matter profile in the original RS09 simulations (prior to rescaling). The horizontal dashed black line $\gamma = 1$ marks the asymptotic limit for a NFW cusp. The arrows mark the resolution limit $3\epsilon = 4.1\,\text{kpc}$. The lower coloured arrows mark the half-light radii for the different representations.

galaxies orbit in the cluster heats up the central dark matter and makes cusps shallower. A limitation of this work was the use of massive particles to represent galaxies which can not capture other processes such as mixing and stripping of stars and dark matter. Their shallow cusp was produced by evacuating the central dark matter and replacing it with massive point-like galaxies. The relative distribution of stars and dark matter was thus not followed realistically.

In our numerical experiment, the galaxies are represented by many particles giving them a gravitationally self-consistent phase-space distribution. The numbers of mergers and of galaxies falling to the centre of the cluster are given by the simulation. Using the fact that the galaxies are set up initially to be spherically symmetric and in a steady state, it follows from Jeans' theorem and Eddington's formula that we can construct different equilibrium stellar density distributions out of the total mass distribution of particles. Our simulations show that differences in the weakening of cusps from one interpretation to another are due to differences in the mixing between stars and dark matter. Within the ΛCDM context, the many collisionless mergers experienced by the BCG produce a weakening of dark matter cusps.

This is a qualitative result and certain aspects of the matter distributions in our simulations remain unrealistic. As a result we do not attempt to reproduce observations of Abell 383 (e.g. the velocity dispersion and luminosity profiles in N11). Even with a fully realistic simulation such a goal would likely be unattainable, given that we have only one realisation of a cluster at our disposition. BCG formation and evolution is tightly coupled to that of the cluster as a whole, so BCGs have a variety of profiles.

In reality the situation is more complicated, galaxies do not form only through collisionless mergers. Disspational processes certainly play an important role in shaping galaxies at earlier times. Baryons dominate the visible regions of the progenitor galaxies and can alter the initial distribution of dark matter in numerous ways: through gas expulsion (Navarro et al., 1996), supernova driven impulsive heating (Pontzen & Governato, 2012), AGN feedback (Duffy et al., 2010) or adiabatic contraction (Blumenthal et al., 1986; Gnedin et al., 2004, 2011).

4.5 Conclusions

We have studied the formation of a $10^{15}\,\mathrm{M}_{\odot}$ cluster in a ΛCDM Universe, following the evolution of galaxies through collisionless mergers from $z = 3$ down to $z = 0$. We showed that as a result of mixing between stars and dark matter in dissipationless mergers, initial cusps ($0.8 < \gamma < 1.3$) can be substantially weakened ($0.3 < \gamma < 0.9$) at the inner-most resolved radii. Our results indicate that observations of shallow dark matter cusps at the centre of clusters are not necessarily inconsistent with CDM. We find changes of dark matter profile slope at a fixed radius of the order $0.3 < \Delta\gamma < 0.5$.

Another interesting result from this study is that the evolution in size is stronger than in mass for more compact stellar distributions. We find that the trend moves from $r_e \propto M$ for extended galaxies to $r_e \propto M^2$ for more compact ones. The latter evolutionary trend has in fact been found in a recent observational study by van Dokkum et al. (2010). Our numerical experiments have some serious limitations that we hope to improve on in future work. It would be interesting to use initial conditions based on the observed $z = 2$ mass-size relation for galaxies combined with stellar to dark matter ratios consistent with abundance matching arguments in order to study the build-up of BCGs and the fate of the most compact ellipticals in ΛCDM more reliably. This would allow us to check semi-analytic descriptions of the process in the ΛCDM context such as that of Shankar et al. (2011). This will be the subject of the next Chapter.

Chapter 5

The Growth in Size and Mass of Cluster Galaxies

We study the formation and evolution of Brightest Cluster Galaxies starting from a $z = 2$ population of quiescent ellipticals and following them to $z = 0$. To this end, we use a suite of nine high-resolution dark matter-only simulations of galaxy clusters in a ΛCDM universe. We develop a scheme in which simulation particles are weighted to generate realistic and dynamically stable stellar density profiles at $z = 2$. Our initial conditions assign a stellar mass to every identified dark halo as expected from abundance matching; assuming there exists a one-to-one relation between the visible properties of galaxies and their host haloes. We set the sizes of the luminous components according to the observed relations for $z \sim 2$ massive quiescent galaxies. We study the evolution of the mass-size relation, the fate of satellite galaxies and the mass aggregation of the cluster central. From $z = 2$, these galaxies grow on average in size by a factor 5 to 10 of and in galaxy mass by 2 to 3. The stellar mass of our simulated BCGs grow by a factor of ~ 2.1 in the range $0.3 < z < 1.0$, consistent with observations, and by a factor of ~ 1.4 in the range $0.0 < z < 0.3$. Furthermore the non-central galaxies evolve on to the present-day mass-size relation by $z = 0$. Assuming passively evolving stellar populations, we present surface brightness profiles for our cluster centrals which resemble those observed for the cDs in similar mass clusters both at $z = 0$ and at $z = 1$. This demonstrates that the ΛCDM cosmology does indeed predict minor and major mergers to occur in galaxy clusters with the frequency and mass ratio distribution required to explain the observed growth in size of passive galaxies since $z = 2$. Our experiment shows that Brightest Cluster Galaxies could, in principle, form through dissipationless mergers of quiescent massive $z = 2$ galaxies, without substantial additional star formation.

5.1 Introduction

Brightest cluster galaxies (BCGs) form the massive end of the galaxy population. Except in strong cooling flows, they are generally associated with old stellar populations, little star formation and large sizes (von der Linden et al., 2007; Bernardi, 2009). In some clusters, BCGs are surrounded by a diffuse envelope of intracluster light. This additional light has been measured in a number of nearby clusters (Gonzalez et al., 2005) as well as in stacks of BCGs from the Sloan Digital Sky Survey (Zibetti et al., 2005). There have been claims (e.g. Collins et al., 2009; Stott et al., 2011) that the observed evolution of BCGs disagrees with the predictions of the semi-analytic galaxy formation models of De Lucia & Blaizot (2007). These studies selected BCGs in high redshift clusters and compared them to the central galaxies of present-day clusters of the same X-ray luminosity, observing little change in the sizes and stellar masses. However, recent results from Lidman et al. (2012) seem to indicate less tension between the models and observations in the evolution of stellar mass (see also Tonini et al. (2012)). It is important to note that current semi-analytic models of galaxy formation do not predict surface brightness profiles in a realistic manner. Thus, any direct comparison of sizes in the models and in real galaxies should be made with caution.

Observations of $z = 2$ galaxies by Daddi et al. (2005) and Trujillo et al. (2007) revealed the presence of a population of massive quiescent galaxies with much smaller sizes than similar mass present-day ellipticals. This result has been confirmed by several other groups (van Dokkum et al., 2008; Newman et al., 2012). Minor mergers (Bezanson et al., 2009; Naab et al., 2009) have been proposed as the main mechanism driving the recent size evolution of elliptical galaxies. Currently, it is unclear whether all such galaxies will grow into present-day ellipticals. Bernardi (2009) proposed that some of these objects might be progenitors of today's BCGs.

White (1976) and Ostriker & Hausman (1977) introduced galactic cannibalism as a possible mechanism to explain the formation of cD galaxies: a central galaxy gradually swallows its companions as dynamical friction brings them to the cluster centre. These deposit their stellar material primarily on the outskirts of the larger galaxy, helping it grow in size and mass. This phenomenon seems to fit well within the ΛCDM cosmogony where structure grows hierarchically. For example, semi-analytic models of galaxy formation find that BCGs form in a two-phase process: an initial collapse with rapid cooling and star formation at high redshift is followed by later growth through multiple dissipationless mergers of pre-existing progenitors (Khochfar & Silk, 2006; De Lucia & Blaizot, 2007). A similar two-phase formation mechanism is also reported in hydrodynamical simulations of massive elliptical formation (Naab et al., 2009; Oser et al., 2010; Feldmann et al., 2011). Notably, Oser et al. (2012b) show that compact massive ellipticals can grow onto the present-day mass-size relation through minor mergers. However, such simulations still produce galaxies that are too massive for the host haloes they inhabit so their quantitative applicability is in some doubt.

Dubinski (1998) studied whether BCGs could form out of a population of spirals between redshift $z = 3$ and $z = 0$. His cosmologically motivated simulation showed that BCGs could potentially form through repeated dissipationless mergers of galaxies. This inspired later studies testing the collisionless merger hypothesis within cosmological simulations which provided new insights into the evolution of BCGs (Ruszkowski & Springel, 2009) and into the origin of the intracluster light (Rudick et al., 2006). A persistent issue, however, is that the structure of the initial galaxies they assumed is inconsistent with recent observations of high redshift galaxies. In Chapter 4, we showed that re-scaling the luminous components of the galaxies to bring them into better agreement with these observations changed the size growth of BCGs from $r \propto M$ to $r \propto M^2$, consistent with observational studies of massive quiescent galaxies at fixed number density (van Dokkum et al., 2010; Patel et al., 2013)

Here, we present a scheme which can weight particles in a high-resolution cosmological simulation of cluster formation to represent realistic stellar density profiles for the initial galaxies. Using this method we can assign to every halo of mass M at a certain redshift z_i, a stellar mass m_* according to an appropriate abundance matching relation, hereafter AMR (Kravtsov et al., 2004; Vale & Ostriker, 2004; Moster et al., 2010; Guo et al., 2010; Behroozi et al., 2010, 2013; Moster et al., 2013). This ensures a faithful representation of the high redshift luminosity function at $z = 2$. We can then study the evolution of cluster galaxies from a population of galaxies consistent *both* with the luminosity function and with the mass-size relation observed at $z = 2$. We aim to test the dissipationless merger hypothesis (White, 1976; Ostriker & Hausman, 1977; Dubinski, 1998). The questions we want to address are the following: are BCGs special or simply the product of merging of normal cluster galaxies? Does star formation contribute substantially to the growth in mass of BCGs between $z = 2$ and $z = 0$? Do mergers explain why BCGs seem to lie off the present-day mass-size relation? Could BCGs have evolved from the observed high-redshift population of massive quiescent galaxies?

Section 2 presents the simulations we use and our method of generating stellar density profiles. In section 3, we study the properties of the BCGs and compare them with observations. In section 4 we study the evolution of BCGs and how it compares to the population of cluster ellipticals. We discuss the significance of our results in section 5 and conclude in section 6.

5.2 Methods

5.2.1 Simulations

We use a set of nine dark-matter-only zoom-in simulations of galaxy clusters from the *Phoenix* project (Gao et al., 2012). These are named Ph-A to Ph-I. The haloes were initially selected from the *Millennium Simulation* (Springel et al., 2005) and re-simulated with comoving softening length $\epsilon = 0.3h^{-1}\,kpc$ and mass resolution $m_p \sim 4{-}10{\times}10^6 h^{-1}\mathrm{M}_\odot$. Details of the simulations are given in Gao et al. (2012). The subhaloes were identified with the structure finder SUBFIND (Springel et al., 2001). We also compute the potential of every particle in each subhalo at redshift $z = 2$. For the rest of the discussion, our units are kpc and $\mathrm{M}_\odot$ for length and mass respectively. This assumes the cosmology of the Millennium simulation: $\Omega_m = 0.25$, $\Omega_\Lambda = 0.75$, $\sigma_8 = 0.9$ and $n = 1$.

5.2.2 A Weighting scheme for cosmological dark matter simulations

The weighting scheme presented here generalises that of Bullock & Johnston (2005) for direct use in cosmological dark matter simulations of structure formation. Cold dark matter (just like stars in a galaxy) is collisionless and its distribution function (DF) satistfies the collisionless Boltzmann equation (CBE). Provided that the DF of the dark matter in a halo is in a steady state, Jeans' theorem guarantees the existence of a distribution function of the form $f = f(I_1, I_2, I_3)$, where $I_{1,2,3}$ are isolating integrals of the motion. In a triaxial potential a DF of the form $f = f(H)$, where $H = \frac{1}{2}v^2 + \Phi$ is the Hamiltonian, can always be generated. Generally, dark haloes are not in a steady state; their lives are continuously shaped by accretion events such as mergers and infall. However, in their study of the evolution of the DF of CDM haloes, Natarajan et al. (1997) showed that between merger events haloes are in phases of "quasi-equilibrium" within the virialised regions. Thus, provided we restrict ourselves to the virialised regions, Jeans' theorem can be invoked to generate a stellar DF of the form $f_* = f_*(E)$.

In order to generate a luminous tracer stellar profile, we take each simulation particle of energy E to simultaneously represent dark matter and stars in diferent amounts. through a weight function $\omega(E) = \frac{N_*(E)}{N(E)} = \frac{f_*(E)g(E)}{N(E)}$, where N is the differential energy distribution, g is the density of states and asterisks denote stellar quantities.

We choose the stellar number density to be represented by the Hernquist (1990) profile:

$$\nu = \frac{a}{r\,(r+a)^3}, \tag{5.1}$$

where a is the scale radius which is related to the 3D half-mass radius through $a = r_e/(\sqrt{2}+1)$. The half-mass radius in projection is related to r_e through $R_e = 1.33 r_e$

We generate f_*, using Eddington's formula:

$$f_*(\mathcal{E}) = \frac{1}{\sqrt{8}\pi^2} \int_0^{\mathcal{E}} \frac{d\Psi}{\sqrt{\mathcal{E}-\Psi}} \frac{d^2\nu(\Psi)}{d\Psi^2} + \frac{1}{\sqrt{\mathcal{E}}} \frac{d\nu}{d\Psi}\bigg|_{\Psi=0}, \tag{5.2}$$

where $\Psi = -\Phi + \Phi_0$ and $\mathcal{E} = -E + \Phi_0 = \Psi - v^2/2$ are the relative potential and total energies respectively. The potential of an NFW profile is generally a reasonable description of the true potential and tends to zero in the limit r goes to infinity thus we set $\Phi_0 = 0$.

The density of states is given by:

$$g(E) = (4\pi)^2 \int_0^{r_E} r^2 \sqrt{2(E - \Phi(r))}\,dr. \tag{5.3}$$

Equations (2) and (3) are only valid for spherical systems, however provided an educated guess, they can also be applied to triaxial ones. Indeed, authors in the past have already used the same formalism to study the distribution function of dark haloes (Natarajan et al., 1997). To compute the $\frac{\mathrm{d}^2\nu}{\mathrm{d}\Phi^2}$ term in Eddington's formula, we have to relate Φ to ν monotonically as $\Phi(r)$ is multivalued in a triaxial potential. For this, we simply approximate

Figure 5.1: Example $\rho_{*} r^2$ profile for a typical compact stellar profile generated using our weighting scheme (black solid line) along with the stellar target profile (red dashed line). The dip is due to low particle numbers in the region below 1 kpc. Arrows mark the radii containing 50 and 95 percent of the simulated stellar mass profile.

$\Phi(r) =< \Phi(\mathbf{r}) >$. However, in the definition of the energy, we retain the actual value of the potential associated with every particle. This ensures the generation of a profile with equidensity surfaces which correctly follow the potential.

Figure 1 illustrates the kind of profile one can generate within the $z = 2$ haloes of the Phoenix simulation given a target input profile (red dashed line). We have checked for the stability of our method by evolving a live dark halo for 150 Myr and saw no change in structure. This was done by keeping the weights of individual particles constant as the N-body simulation evolves them forward in time. We further looked for isolated galaxies in haloes which have not experienced any stellar mass growth between $z = 2$ and $z = 0$. We present such an example in the top panel of Figure 2. This halo has grown in dark matter mass by a factor of two but its stellar mass profile has changed very little over 10 Gyr, although the half-light radius (defined as the radius of a sphere containing half the total stellar mass) has increased by 30 percent. This is not a substantial problem for studying the evolution of BCGs, where the change in radius is much larger and is primarily caused by material deposited on the outside of the galaxy (see below and also Chapter 4). Nevertheless it warns us that our experiment is close to the resolution limit for studying the size growth of galaxies which do not accrete much stellar mass. Considering the large period of time over which this test was carried out, we infer that two-body relaxation processes are not the driving force behind the size growth we observe below for the most massive galaxies. The bottom panel of Fig. 2 shows the evolution of a BCG which has grown in mass by $m_{*_f}/m_{*_i} = 4$ and in size by $r_f/r_i = 9$, where the subscripts i and f designate the initial and final times.

5.2.3 Initial Conditions

For our initial conditions, we choose to represent a population of galaxies consistent with the observed stellar mass function at $z = 2$, which we relate to ΛCDM haloes in the simulations through recent AMR results (Moster et al., 2010) which are consistent with results from Moster et al. (2013) even at $z = 2$. We do not include the scatter in these relations, as the scatter for the mass-size relation is already large. We further require that the sizes of our model galaxies are consistent with those observed for massive quiescent galaxies at $z = 2$. For our purposes, we choose the mass-size relation as parametrised by Williams et al. (2010) and note that it is very similar to that of Newman et al. (2012) (see the 3rd panel of their Figure 8).

At $z = 2$, a few haloes are undergoing mergers, but because these are a small fraction of the total, we normally ignore them. However, if a particularly massive halo hosting a

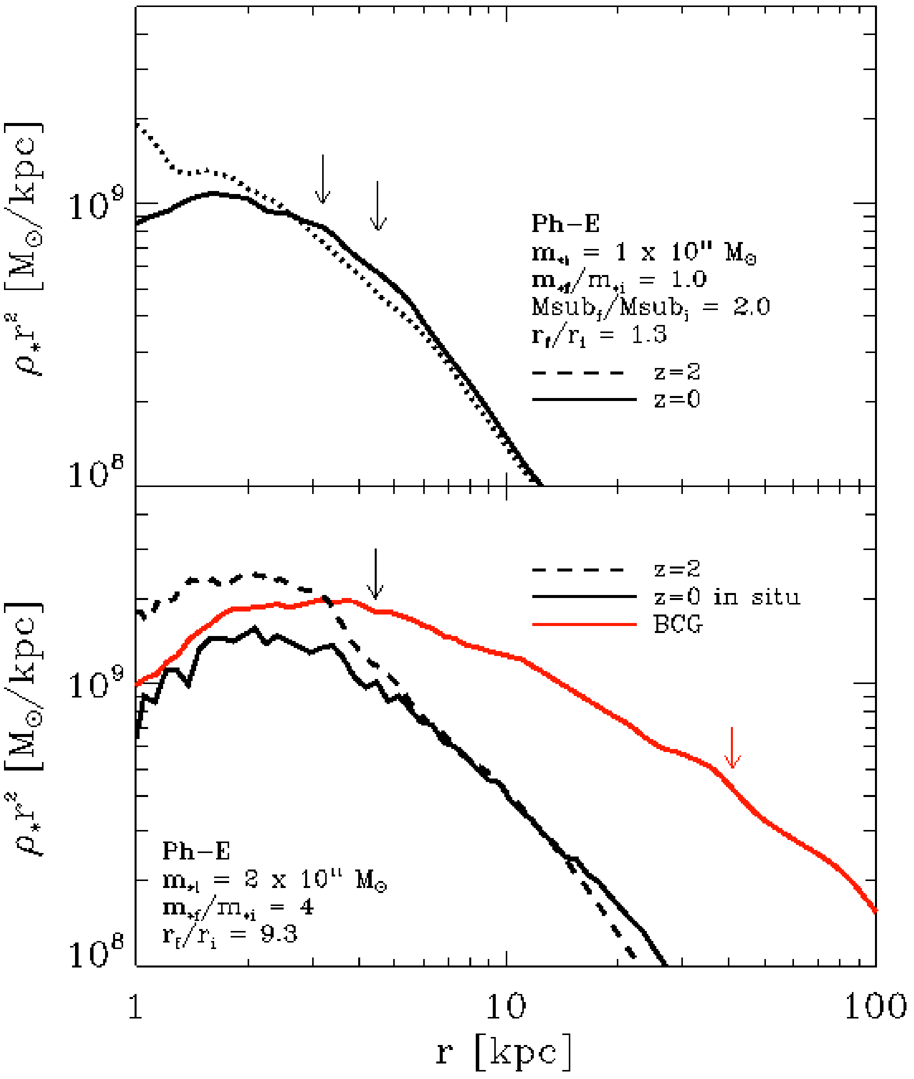

Figure 5.2: *Top*:$\rho_* r^2$ profile for a galaxy which has evolved from $z = 2$ (dashed line) to $z = 0$ (solid line) without experiencing mergers or interactions with other haloes populated with stars. The host dark matter halo has grown in mass (M_{sub_f}/M_{sub_i}) by a factor of 2. This does not, however, translate in significant size growth (r_f/r_i) of the stellar component. The arrows mark the radii enclosing 50 percent of the mass of the galaxies. *Bottom*: $\rho_* r^2$ profiles for a BCG most massive progenitor (dashed black line), and final $z = 0$ BCG (red line). We also show the distribution of the stars in the BCG most massive progenitor at $z = 0$ (solid black line). The BCG grew by a factor of $m_{*_f}/m_{*_i} = 4$ in stellar mass and $r_f/r_i = 9.3$ in size. The black and red arrows show the radii enclosing 50 percent of the mass of the most massive BCG progenitor at $z = 2$ and BCG at $z = 0$ respectively. Clearly, the size growth observed for these galaxies is not due to two-body relaxation processes.

$\sim 10^{11}M_\odot$ galaxy is undergoing a merger we generate its stellar distribution function at an earlier snapshot. Depending on the state of the halo it is sometimes hard to generate stellar density profiles that perfectly match the original target, but as long as the galaxies are within the scatter of the observational relation we consider this good enough. For the rest of our discussion of the structural properties of ellipticals in clusters we will focus on objects which have masses above $7 \times 10^{10}\mathrm{M}_\odot$, which still leaves us with a sample of 156 galaxies at $z = 2$. We follow, the subsequent evolution of galaxies by keeping the weights of individual particles fixed as the simulations evolve. Since our experiment tests the collisionless merger evolution scenario, stars and dark matter particles with similar orbits are expected to follow each other over time.

5.3 Structural Properties of BCGs

As a first test, it is interesting to check whether the total stellar mass of the final merger remnant agrees with expectations from the BCG luminosity function at $z = 0$. Figure 3 shows the stellar-to-halo mass relation for the galaxies at $z = 2$ and for cluster centrals and satellite galaxies at $z = 0$. As expected, many cluster galaxies have their dark matter haloes stripped, moving them horizontally in the $m_* - M_{halo}$ plane. Some of the cluster galaxies have a stellar mass deficit which can be explained by the lack of star formation in our experiment. These galaxies lie below the Moster et al. (2010) relation at $z = 0$. Some cluster satellite galaxies however grow to stellar masses in agreement with the relation at $z = 0$. Moreover, the final BCGs occupy a region that is in good agreement with expectations of AMRs at $z = 0$. This success depends on the assumption we made about the progenitor galaxies at redshift $z = 2$ and on the hierarchical growth of the clusters according to the ΛCDM paradigm. At face value, this strongly supports the hypothesis that BCGs form from dissipationless mergers of galaxies that were already in place at $z = 2$. This is in line with the galactic cannibalism picture originally formulated by White (1976) and Ostriker & Hausman (1977): BCGs *predominantly* grow through the later merging of already existing galaxies. This idea agrees with the more recent studiy of De Lucia & Blaizot (2007) who find using their semi-analytic model that 80 percent of the stars ending up in BCGs are already formed at $z = 3$. With this in mind, we now ask whether any of the structural properties of our BCGs closely resemble those of known cluster central galaxies.

5.3.1 Surface Brightness and Density Profiles

Recent studies of massive quiescent galaxies at $z = 2$, (Williams et al., 2010; van Dokkum et al., 2008) adopt a Kroupa IMF and solar metallicity when interpreting their photometric data and find a stellar population age of 1 Gyr for the bulk of the population. We adopt these same parameters for all of our galaxies. Our experiment assumes that the stellar populations evolve passively (the collisionless merger hypothesis), so we determine the mass-to-light ratios at later times using the values computed by Maraston (2005). We

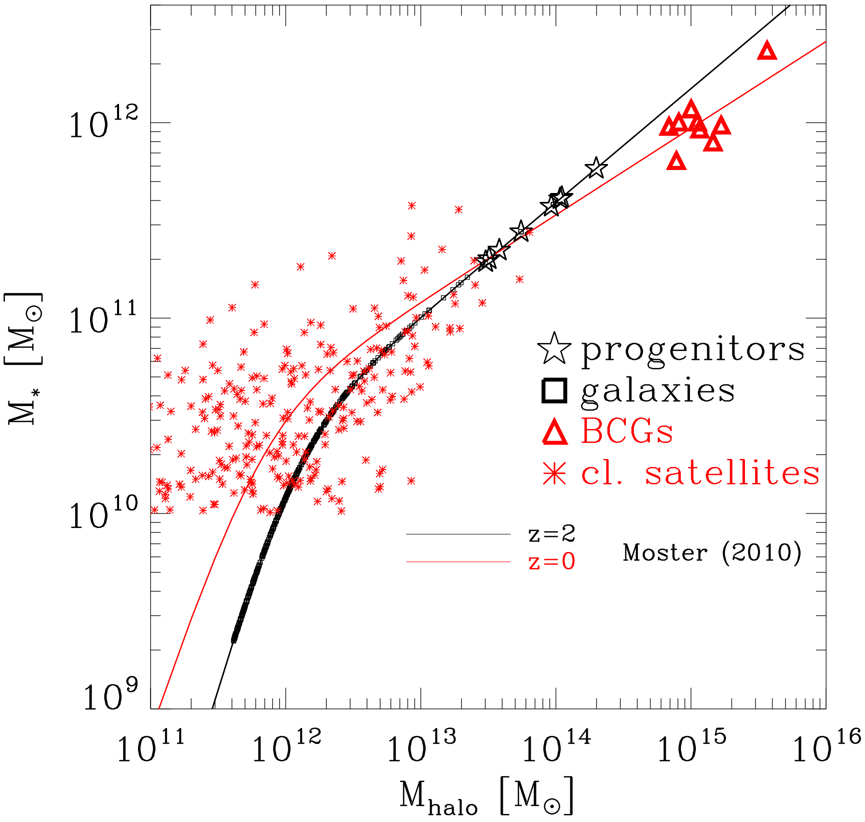

Figure 5.3: Stellar-to-halo mass relations at z=2 and z=0 (black and red lines respectively). The black stars represent the most massive progenitors of BCGs at z=2 and the small black squares represent all the haloes populated with stars in the initial conditions. The red triangles are the BCGs at z=0 and the red crosses represent cluster satellite galaxies.

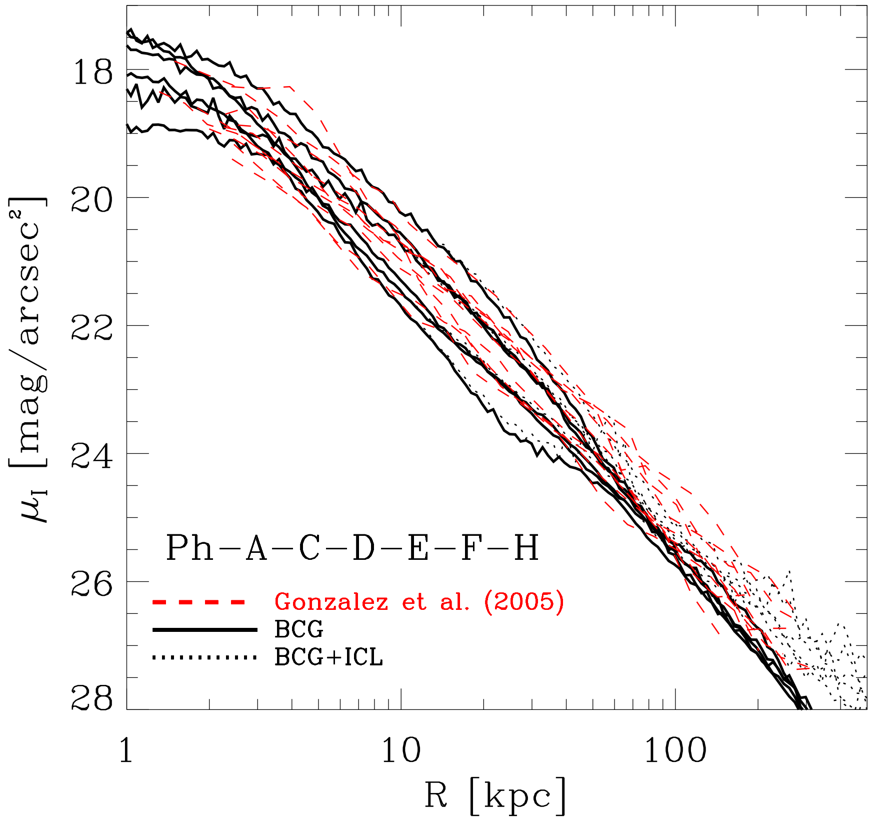

Figure 5.4: Surface brightness profiles for BCGs at $z = 0$ derived assuming passive evolution between $z = 2$ and $z = 0$. Overplotted in red are surface brightness profiles for nearby galaxy clusters from Gonzalez (2005). The simulated surface brightness profiles have a sligthly steeper fall-off at large radii compared to the observed ones but can be accounted for including intra-cluster light.

note that Newman et al. (2012) use Salpeter IMFs to derive their stellar masses, however due to the large scatter in the mass-size relation this is a minor issue. In fact, the two sets of data agree at $z = 2$. Stellar mass-to-light ratios are assumed fixed as a function of radius. We have not tried varying ages or metallicity with host mass as there are currently no observational constraints on variations in stellar metallicity or age at such redshift.

In Figure 4, we present surface brightness profiles for BCGs at $z = 0$. This is done by taking 50 random projections of the individual galaxies. Surface brightness profiles taken from Gonzalez et al. (2005) are overlaid in red. These authors measured the surface brightness profiles of 24 nearby BCGs in the I-band. The clusters they used were in the redshift range $0.03 < z < 0.1$. We find a reasonable match between the observed and simulated light distributions both in shape and in normalisation. However, we still note that at large radii our simulated galaxies have systematically slightly steeper fall-offs in their surface brightness profile.

Some authors have claimed that BCGs are already well in place at high redshift, $z = 1.0$, and that they evolve little thereafter (Collins et al., 2009; Stott et al., 2011). We compare the surface brightness profiles of some of our relaxed cluster BCGs to those of compiled by Stott et al. (2011) at $z = 1.0$ in Figure 5. These authors deduced a stellar population formation age at $z = 3$, similar to that is found for quiescent $z = 2$ galaxies. The observations were performed in the *HST* F850LP band, but we compute our surface brightness profiles assuming a mass-to-light ratios in the SDSS z band which matches closely the F850LP band. We add the $(1 + z)^4$ surface dimming correction for direct comparison with their data. Given the uncertainties in the IMF and the different band zero-point, the agreement between the two is still reasonable and encouraging.

We also present the evolution in density profiles from $z = 2$ to $z = 0$ in Figure 6, separating the components into in-situ and accreted components. As previous studies have shown the size evolution is predominantly driven by adding stellar mass to the outskirts of the galaxies (Naab et al., 2009; Oser et al., 2012b; Laporte et al., 2012; Hilz et al., 2012).

5.4 Evolution of BCGs and Ellipticals in Clusters

Recently, Lidman et al. (2012, hereafter L12), presented new results on the evolution of the stellar mass in BCGs using samples of high, intermediate and low redshift clusters. We compare their data with ours in Figure 7, looking at cluster mass versus BCG stellar mass at three different redshifts. Our BCGs lie within the scatter of their data, although generally towards the massive end in stellar mass. However, we show this is also partly due to the way L12 derive their stellar masses. For some of our BCGs, we used de Vaucouleurs profile fits within an aperture of 30 kpc to derive stellar masses. For high Sersic indices (e.g. $n = 8$) up to half of the total stellar mass of the BCG can be missed. We indicate the shifts such systematics can cause for a few of our galaxies in Figure 7, showing that this might bring them in better agreement with the data. On the whole, L12 observe a stellar mass growth rate of 1.8 between $0.2 < z < 0.9$ for their sample. This is consistent with that found for our simulated galaxies: we observe a stellar mass increase of factors of

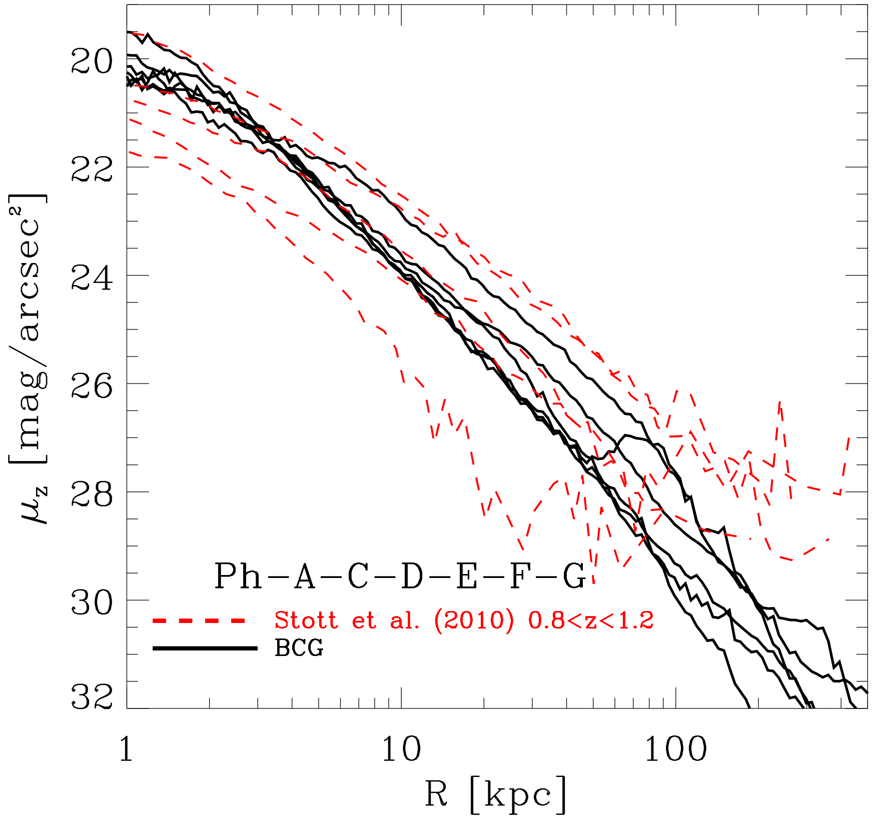

Figure 5.5: Simulated surface brightness profiles in the SDSS z-band for BCGs at $z = 1$ against projected radius. Overplotted in red are the observed surface brightness profiles in the F850LP HST band of for clusters of similar mass taken from the sample of Stott et al. (2011)

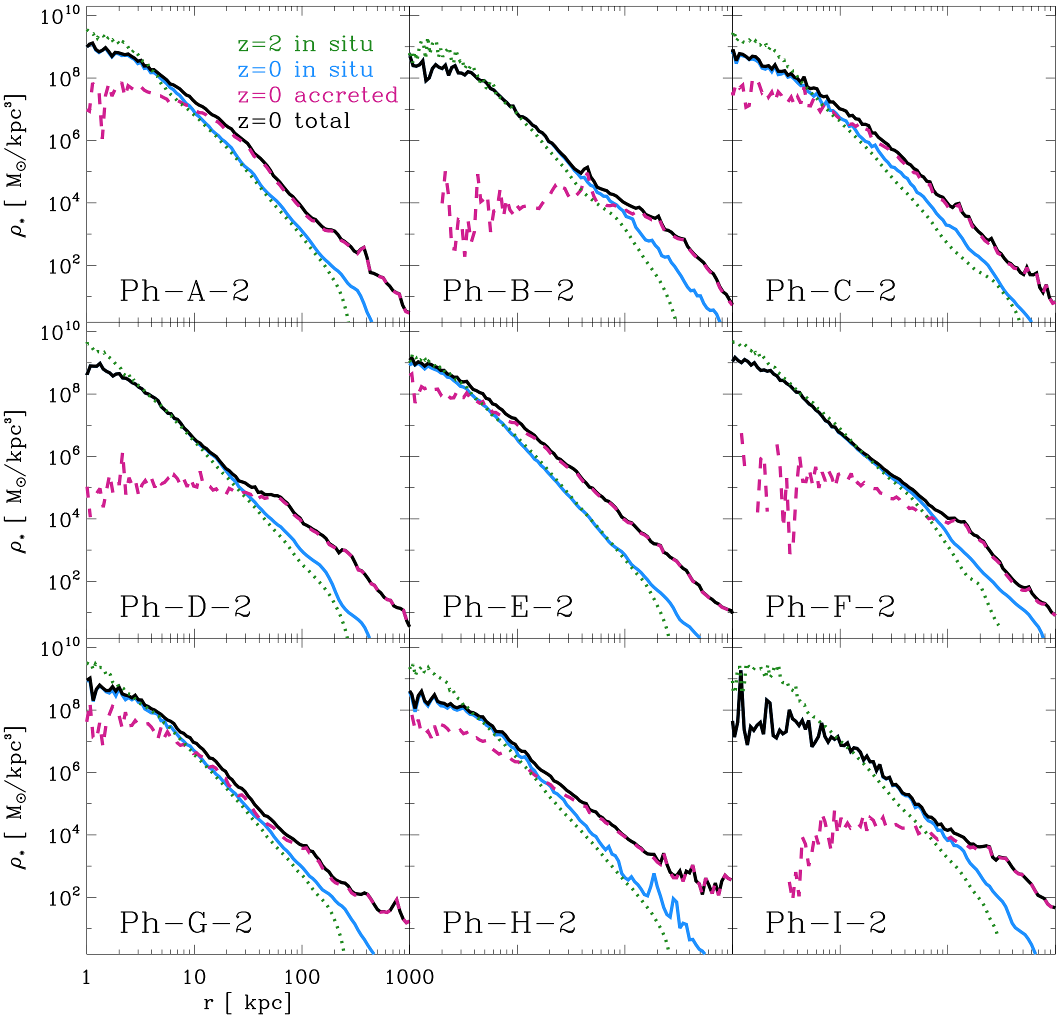

Figure 5.6: Density profiles of BCGs for the nine cluster simulations. We separate in-situ components at $z = 2$ (for the most massive progenitor) and $z = 0$ (green and blue respectively) and accreted component at $z = 0$ (magenta), the final BCG density profile is shown in black. Note that haloes B, H, I are unrelaxed at z=0 making their analysis cumbersome.

2.1, 1.4 and 2.6 over $0.3 < z < 1.0$, $0.0 < z < 0.3$, and $0 < z < 1$ respectively. The stellar mass growth since $z < 1$ reported here is consistent with results from De Lucia & Blaizot (2007) and Tonini et al. (2012)

We now turn to a comparison of the evolution in mass and size of the BCGs and that of the general cluster population of ellipticals. We proceed by identifying all the $z = 2$ haloes which end up in the final clusters at $z = 0$ (defined as the major FOF group) and track them over redshift using trees constructed from the SUBFIND data at ~ 50 intermediate outputs using individual particle IDs to match subhaloes in neighbouring outputs. As in Ruszkowski & Springel (2009), we compute three-dimensional spherical stellar mass profiles using logarithmic bins of widths $\Delta = 0.1$ and measure their 3D half-mass radii. This is shown in Figure 8. We visually inspected the individual density profiles of cluster galaxies checking their Hernquist profile fits given the parameters determined in the previous step, namely M and a. However, for BCGs, as their profile can sometimes be more extended (with Sersic profiles reaching $n = 8-10$) than a simple de Vaucouleurs law, these fits were often poor. Furthermore, we note that some clusters are out of equilibrium at various times which complicates the analysis of the central galaxy, this is the case for Ph-A-B-H-I at $z = 1$ and for the Ph-B-I clusters at $z = 0$.

Comparing panels, we see that BCGs evolve more rapidly than other galaxies and that different BCGs evolve at different rates. While some of the BCGs experience rapid growth in stellar mass by $z = 1$ (e.g. Ph-H), others see most evolution between $z = 0.3$ and $z = 0$ (e.g. Ph-B, Ph-G). There are also BCGs that show almost no significant evolution in stellar mass or size between $z = 0.3$ and $z = 0$ (e.g. Ph-A, Ph-E). Furthermore, some BCGs still suffer many mergers between $z = 0.3$ and $z = 0$, this is the case for Ph-I, which doubles in stellar mass. Such late phases of merging are observed (Liu et al., 2009; Brough et al., 2011). We also see a growing mass gap between BCGs and other cluster ellipticals as we get closer to $z = 0$.

Our result confirms that of Ruszkowski & Springel (2009): BCGs tend to move off the mass-size relation of local ellipticals because of their much higher merger rate. Whether all BCGs should lie off the normal relation is harder to ascertain with a sample of only nine galaxy clusters. We find that at $z = 0$, our cluster-ellipticals and some our BCGs lie on the mass-size relation derived by Hyde & Bernardi (2009). For comparison we also show in Figure 7 the Shen et al. (2003) relation which is shallower, a consequence of using Petrosian-based quantities which introduces a bias for objects of large Sersic index.

It is interesting to also look at the amount of mass deposited through mergers and disruption of satellites. We define a merger event with the BCG when half of the stellar mass of a progenitor galaxy gets incorporated within the first subhalo of the FOF group (defined as the halo inhabited by the BCG). Anything below this threshold we called "diffuse" stellar accretion from stripped satellites. We list in Table 1 the amount by which each type contributes to the mass aggregation for each BCGs. This table shows that for the various BCGs not all the mass accretion came from mergers but also some from stripped galaxies or galaxies in the process of merging. This amount of diffuse mass deposition, defined in Table 1 as the percentage of the final BCG mass diffusely accreted (i.e. $f_{diffuse} = (m_{acc} - m_{merger})/(m_0 + m_{acc})$, where m_0 is the mass of the in-situ component

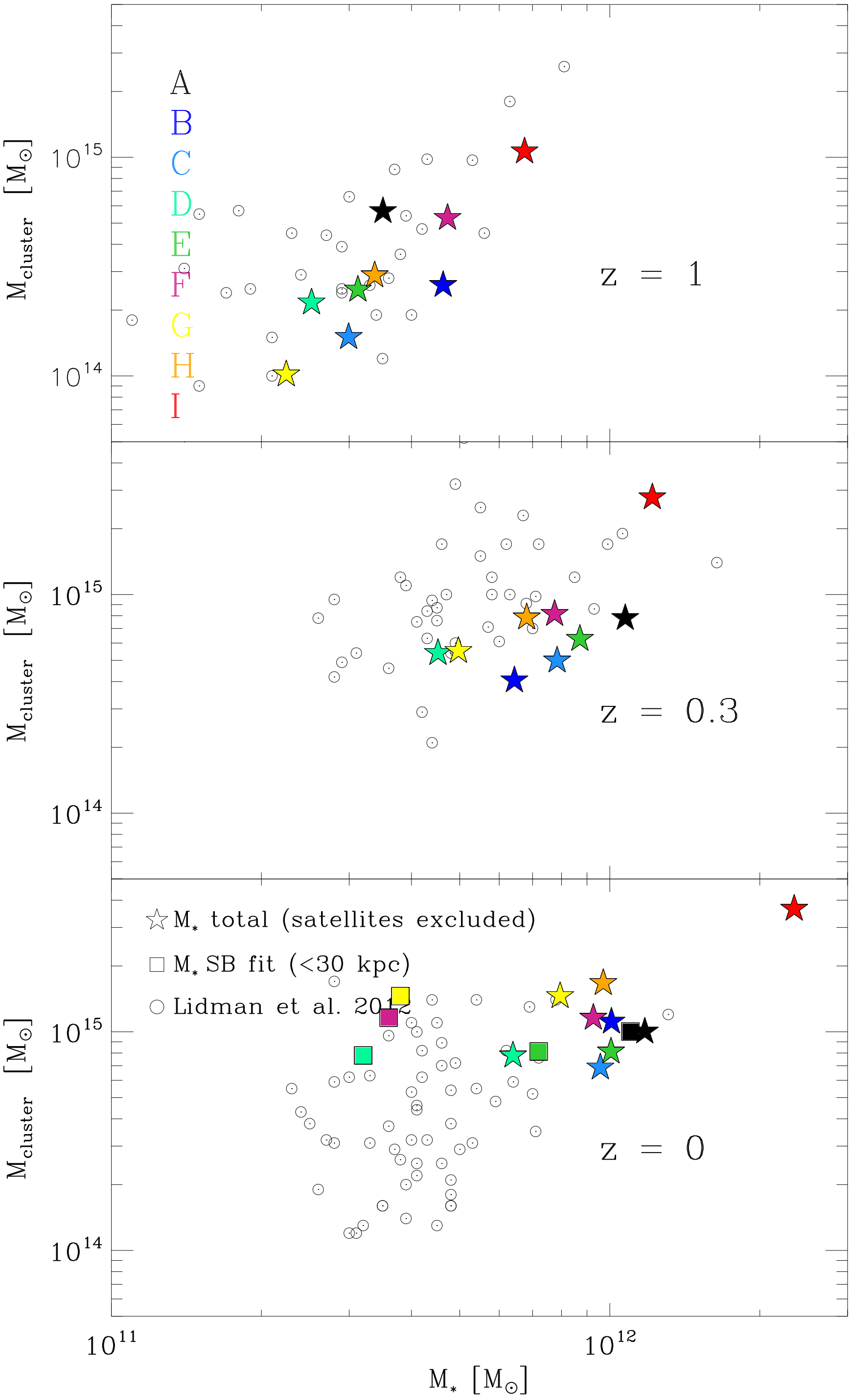

Figure 5.7: Cluster mass against BCG stellar mass at different redshifts. *Top:* High-z BCG sample ($0.8 < z < 1.5$) and the Phoenix BCGs at $z = 1.0$ (coloured stars). *Middle:* Intermediate-z L12 BCGs ($0.2 < z < 0.5$) and Phoenix BCGs at $z = 0.3$. Bottom: Low-z ($z < 0.2$) L12 BCGs and Phoenix BCGs. At $z = 0$, we show for some BCGs the stellar mass predicted by fitting a de Vaucouleurs profile within a 30 kpc aperture. For large indices (n=8 or n=10) this can lead to an underestimate of the true stellar mass of up to a factor of two. Models and observations are consistent at all z given the large scatter in the observations.

Run	m_0 $10^{11}\mathrm{M}_\odot$	m_{acc} $10^{11}\mathrm{M}_\odot$	m_{merger} $10^{11}\mathrm{M}_\odot$	f_{diffuse}	M_{200} $10^{14}\mathrm{M}_\odot$
Ph-A-2	3.9	7.8	7.2	0.05	8.9
Ph-B-2	4.1	5.9	4.4	0.15	11.3
Ph-C-2	2.8	6.8	6.0	0.08	7.5
Ph-D-2	2.0	4.4	2.1	0.07	8.5
Ph-E-2	2.8	7.3	6.8	0.30	8.2
Ph-F-2	4.1	5.2	3.2	0.20	10.9
Ph-G-2	2.2	5.7	2.9	0.32	15.8
Ph-H-2	1.8	6.6	4.4	0.3	15.6
Ph-I-2	5.8	17.6	11.2	0.3	33.0

Table 5.1: Initial mass of the most massive BCG progenitor, stellar mass accreted over the last 10 Gyr, stellar mass contributed by mergers, the fraction of the final stellar mass contributed by the disruption of satellites (not defined as mergers) and final cluster mass. Note that we define a merger to occur when more than 50 percent of the stellar mass of a galaxy goes into the final BCG.

of the most massive BCG progenitor), can vary between five percent (Ph-C) and thirty percent (Ph-G and Ph-H) of the total accreted stellar mass. Furthermore, these values of accreted stellar mass are in agreement with the trends found in Moster et al. (2013). We also present the number of mergers each BCGs experienced through their lifetime and list their ratios in Table 2. Although our definition of merger is somewhat arbitrary it clearly shows that BCGs go through a succession of major (1:1 - 1:2) and minor merging events (1:3 - 1:10) both of which are observed in real BCGs (e.g. Liu et al., 2009; Edwards & Patton, 2012). Furthermore, we see that the clusters for which we have identified fewer mergers also have a higher fraction of diffuse stellar accretion through stripped satellites: this is the case for clusters Ph-F, Ph-G and Ph-H. Although, there is a mixture of types of mergers, in the cases where minor merging has been predominant (Ph-B, Ph-C, Ph-D, Ph-F, Ph-I), the numbers and ratios are in agreement with those which the ad hoc simulations of Hilz et al. (2013) found necessary to make the sizes of compact high-z ellipticals grow to those of present-day ones.

5.5 Discussion

We now turn to compare our work with previous simulation studies of BCGs. Recently, Martizzi et al. (2012) presented hydrodynamical simulations of BCGs in which the central galaxy was brought to agree with the local AMRs through the inclusion of AGN feedback. However, the surface brightness profile of the final galaxy contains a stellar core of 10 kpc. Such large stellar cores are clearly absent in real BCGs (Lauer et al., 2007). The largest core size measured in a BCG is of $\sim$ 3kpc (Postman et al., 2012). This suggests that the AGN feedback mechanisms implemented in these simulations are too strong.

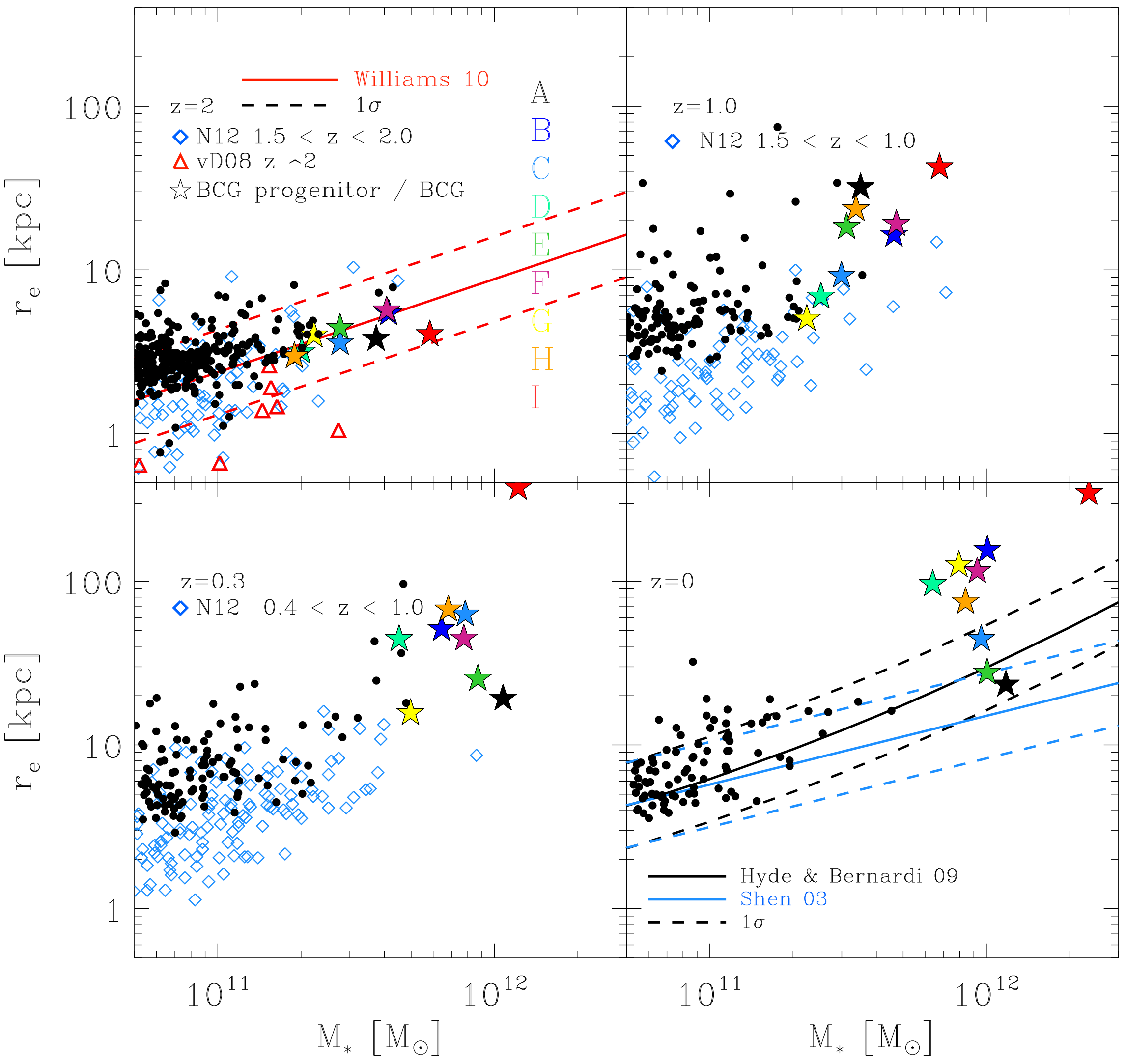

Figure 5.8: Mass-size evolution for cluster galaxies. Note that we use a 3D definition of half-mass radius for our simulated galaxies and we compare these to de-projected half-mass radii for observations. Black dots represent simulated ellipticals, stars depict the $z = 0$ BCGs and their most massive progenitors in the higher redshift panels. *Top left*: $z = 2$ initial conditions overlaid with data from Newman et al. 2012 (N12) in blue diamonds, van Dokkum et al. (2008) in red triangles and the relation from Williams et al. 2010. *Top right*: $z = 1.0$ mass size relation with data from N12 in the redshift range $1.5 < z < 1.0$. *Bottom left*: $z = 0.3$ mass-size relation with data from N12 in the redshift range $0.4 < z < 1.0$. *Bottom right*: $z = 0$ mass-size relation overlaid with the mass-size relations of Hyde & Bernardi (2009) and Shen et al. (2003)

Run	1:1-2	1:3-5	1:10-100
Ph-A-2	2	1	6
Ph-B-2	0	4	3
Ph-C-2	1	4	5
Ph-D-2	1	2	2
Ph-E-2	2	1	4
Ph-F-2	1	0	3
Ph-G-2	1	2	8
Ph-H-2	2	3	2
Ph-I-2	0	6	8

Table 5.2: Table summarising the merger count for each BCG. Note that we define a merger when more than 50 percent of the stellar mass of a galaxy goes into the BCG.

While it seems that AGN feedback is the most promising way of suppressing over-cooling and star formation at the centre of clusters (Croton et al., 2006; Sijacki & Springel, 2006; Puchwein et al., 2010), its impact on the structure of the existing stellar population in the cluster central galaxy is probably negligible because too little gas is present in the star-dominated regions. Our work shows that dissipationless mergers of galaxies between $z = 2$ and $z = 0$ can produce BCGs with properties closely resembling those seen in the local Universe (surface brightness profiles, stellar-to-dark matter ratios).

Turning to the evolution of our, by definition, "quiescent" galaxies, we observe an evolutionary trend close to those found in observations (e.g. Newman et al. (2012)). However we caution that perhaps our experiment is over-idealised for such a direct comparison to observations. Indeed, the $z = 2$ galaxy population is diverse, containing extended star-forming galaxies as well as quiescent galaxies (e.g. Figure 2 in Szomoru et al. (2012)). In this paper we have assumed that all haloes at $z = 2$ contain compact quiescent galaxies. On the other hand, we can affirm that BCGs could well be descendants of quiescent massive ellipticals at $z = 2$. The best evidence for this in our experiment is that our simulated galaxies started on the same mass-size relation as the bulk of galaxies, yet mergers turn them into present-day systems which closely match the surface brightness profiles of known BCGs.

One limitation of our experiment is that we omit the effect of the baryons on the total potential of galaxies at $z = 2$. We have considered the potentials of halos in the dark-matter only simulations to represent those of $z = 2$ galaxies. Including the self-gravity of the stars would in principle deepen the galactic potential wells, making tidal stripping of the inner-regions of haloes less efficient. However, the inclusion or omission of contraction of the dark matter haloes due to the presence of a stellar component in these simulations appears to make relatively little difference to the final results on the evolution of the BCG as seen in Chapter 4 or Ruszkowski & Springel (2009). Once more information is available on the internal structure of galaxies at $z = 2$, it will be necessary to consider more complex modelling, including the stars explicitly.

5.6 Conclusions

We have studied the late formation and assembly of BCGs in the ΛCDM cosmology starting from a $z = 2$ population of "quiescent" galaxies resembling those observed. We did so by representing the stellar components of galaxies inside their dark matter haloes through a particle weighting scheme. In contrast with previous studies, our experiment *simultaneously* represents the luminosity function at $z = 2$ as derived from abundance matching relations and the observed mass-size relation at $z = 2$. Previous N-body studies asssumed substantially too much stellar mass for a given halo mass (Ruszkowski & Springel, 2009; Rudick et al., 2011), thus adopting initial conditions inconsistent with modern observations and a ΛCDM cosmology.

Under the assumptions of our experiment, we predict present-day BCGs with stellar masses in good agreement with those inferred from the $z = 0$ stellar-to-halo mass relation. Moreover, the surface brightness profiles of our simulated BCGs match observations of local BCGs both in shape and in normalisation. This suggests that most BCGs have evolved passively from $z = 2$ to $z = 0$, forming out of a pre-existing population of compact galaxies with very little star formation after $z = 2$.

The large masses and sizes of BCGs reflect the hierarchical growth of structure in ΛCDM and their special location at the centres of galaxy clusters. Our experiment also reproduces surface brightness profiles of some of the five $z \sim 1$ BCGs in Stott et al. (2011) suggesting that these do not conflict with ΛCDM expectations. In fact, we show that our results agree well with the recent study of Lidman et al. (2012). Our simulated galaxies suggest that estimates based on fluxes within 30 kpc apertures may in some cases substantially underestimate the stellar masses of BCGs.

The Phoenix project offers an important window to study various aspects of cluster dynamics and the evolution of galaxies and the gravitational wave signal from merging black-holes (McWilliams et al., 2012). Our presented scheme could be used in the future with the aim to address questions about colour and metallicity structure in BCGs.

Chapter 6

The re-distribution of matter in galaxy clusters

We present cosmological N-body simulations to study the dynamics of mixing between stars and dark matter at the centre of galaxy clusters. We simulate the late time assembly of galaxy clusters from $z = 2$ to the present day by populating dark matter haloes with self-consistent stellar components satisfying observational constraints (mass-size and stellar-to-halo mass relations) at $z = 2$. The central regions of galaxy clusters get re-shaped through multiple mergers. These give rise to dark matter density profiles shallower than their dark matter-only run counterparts, reaching values of $\gamma = -\frac{d\ln\rho}{d\ln r}$ in agreement with recent measurements for galaxy clusters. The radius of transition to dark matter slopes shallower than $\gamma = -\frac{d\ln\rho}{d\ln r} = 1.0$ occurs at a scale of $r/r_{200} \sim 0.1 - 0.2$ similar to observations. The total dark matter density profiles remain identical to the dark matter only runs except below a scale of $r/r_{200} \sim 0.002 - 0.003$ where the stars dominate. The line-of-sight velocity dispersion profiles for the stars are also consistent with those measured for similar mass clusters. Thus the recent observations of galaxy clusters following an almost universal profile in their total density profile is not surprising and a reflection of the predominantly dissipationless assembly. Our numerical experiment shows that dissipationless mergers do not always bring dark matter fractions up at the centre of massive ellipticals but can also decrease them. The reason for this is related to the large scatter in stellar central densities at a given stellar mass which can lead to scenarios where denser galaxies can merge to the centre of a more extended progenitor, thus decreasing the dark matter fractions by factors as high as 2 within $1 - 2kpc$. Based on the merger histories of the clusters, we further estimate the effect of matter scouring (via dynamical friction) due to the presence of black holes in the most massive galaxies. We find that mass deficits of up to $M_{\rm def} \sim 10^{11}\,\mathrm{M}_\odot$ are possible, providing a natural explanation for the existence of the largest stellar cores of size $r_c \sim 3\,\mathrm{kpc}$ observed in the Brightest Cluster Galaxies.

6.1 Introduction

In the standard ΛCDM cosmological paradigm, dark matter is a collisionless particle and its clustering can be followed by solving the collisionless Boltzmann equation (CBE). This can be done through Monte-Carlo techniques such as the N-body method. In the last decade, cosmological dark matter only simulation have shown that the spherically averaged density profiles of dark matter haloes follow a universal form from clusters to dwarf galaxy scales which may be parametrised by the Navarro, Frenk & White (1997, 'NFW' hereafter) profile [1]. This density profile is characterised by a falls off as $\rho \propto r^{-3}$ at large radii and asymptotes to $\rho \propto r^{-1}$ as $r \rightarrow 0$. The exact origin of this profile is still unclear and many arguments have been put forward from multiple mergers(Syer & White, 1998) or the maximisation of entropy subject to constraints like the constancy of actions (Pontzen & Governato, 2013) but a convincing understanding of the emergence of such profile is yet lacking. The problem is made difficult when comparing models to simulations due to the inherent disjoint symmetries between spherical/axisymmetric models to triaxial ones, making the true identification of the isolating integrals of the motion arduous in the latter case (see for example Pontzen & Governato (2013)).

Observations of relaxed galaxy clusters on the other suggest that the dark matter density profiles are shallower than those found in simulations (Sand et al., 2002, 2004, 2008; Newman et al., 2009, 2011, 013b). However, recent results from Newman et al. (013a) combining simultaneously differerent mass measurement techniques (stellar kinematic, strong lensing, weak lensing and the X-ray emission from the hot electrong gas) point that the total density profile of such clusters are consistent with the end result of dark matter only collissionless simulations. This suggests that regardless of the galaxy formation physics, the NFW profile may be a gravitational attractor. This idea was proposed by Loeb & Peebles (2003) suggesting that such an attractor solution should arise in galaxies where the late assembly is orchestrated by dissipationless mergers. Although baryon condensation into stars would steepen the total density profile of progenitor galaxies, these authors postulated that the later high number of disspationless mergers would create enough fluctuations in the potential of the galaxies thus taking the new combined collisionless fluid back to the universal profile as observed in dark-matter only simulations. Gao et al. (2004) qualitatively studied this by tracking the central dark matter particles in dark matter-only simulations of galaxy clusters back to higher redshifts and saw that the inner-region of the dark matter profile of galaxy clusters is indeed built up by the assembly of separate entities formed at higher redshifts. They suggested that with the presence of starts efficient mixing would be possible to give rise to an attractor solution. However, the experiment containing two collisionless fluids (dark matter and stars) with initial conditions constrained by observations of real galaxies has yet never been carried out explicitly to test this attractor hypothesis.

It is generally thought that dynamical friction which brings galaxies to the cluster centre helps evacuating the central dark matter from the central region, depositing it to larger radii El-Zant et al. (2004). However, Laporte et al. (2012) showed that the competition between dynamical friction, stripping between stars and dark matter can vary the strength of this process which also depends on the initial structure of high-redshift galaxies. These authors showed that the later mixing of stars and dark matter through dissipationless mergers can produce reduce the strenght of the dark matter cusp up to an amount $\Delta\gamma = 0.5$ at the inner most resolvable radius, however their initial conditions where not correctly representative of the observations and results could only be interpreted qualitatively.

---

[1] It should be noted however that some scatter exists from halo to halo (Navarro et al., 2010)

In this contribution, we test whether given the current observational information on the structure of massive $z = 2$ galaxies, the later dissipationless mergers which occur at the cluster centre are able to produce dark matter cusps as shallow as those of Newman et al. (013b) and total density profiles consistent with (Newman et al., 013a). We run simulations which take explicitly into account the baryonic stellar loading of dark matter haloes at redshift $z = 2$ and follow the subsequent evolution of star and dark matter particles to the present-day. To this end, we have developed a method for directly inserting self-consistent luminous components of galaxies inside dark matter haloes formed in cosmological simulations. Past simulations of this sort have generally replaced dark matter haloes (and all their substructure) with spherical compound galaxy models made up of stars and dark matter (Dubinski, 1998; Rudick et al., 2006). We take a dark-matter only zoom-in simulation at $z = 2$ in which we insert directly stellar spheroids in equilibrium following constraints from abundance matching results Moster et al. (2013) and mass-size relations of galaxies at $z = 2$. The galaxies initially re-virialise as the dark matter particles are not aware of the newly inserted stellar potentials on a timescale of four to five dynamical times. We then study the mixing between stars and dark matter and the final resulting density profile which we compare to dark-matter-only simulations. Section 2 introduces the simulations and discusses our method for inserting N-body equilibrium model galaxies in cosmological dark matter simulations as well as stability and resolution tests which were performed. We study the final structural properties of the clusters in section 3. In section 4 we look further into the mergers and mixing processes that occured in the central region of the clusters. We discuss the further important role of black holes in section 5 and dicuss our results and conclude in section 6 and 7 respectively.

6.2 Numerical methods

6.2.1 Simulations

We use a suite of zoom-in dark matter only simulations of galaxy clusters, the PHOENIX project Gao et al. (2012) as our starting point for re-simulating the passive evolution of galaxies from $z = 2$ to $z = 0$. The haloes in the PHOENIX suites were initially selected from the *Millennium Simulation* (Springel et al., 2005) and re-simulated with comoving softening length $\epsilon = 0.3h^{-1}$ kpc and mass resolution $m_p \sim 4 - 10 \times 10^6 h^{-1}\,\mathrm{M}_\odot$. Details of the simulations are given in Gao et al. (2012). This assumes the cosmology of the Millennium simulation: $\Omega_m = 0.25$, $\Omega_\Lambda = 0.75$, $\sigma_8 = 0.9$ and $n = 1$. For the rest of the discussion, our spatial and mass units are in kpc and in $\mathrm{M}_\odot$ respectively. The subhaloes were identified with the structure finder SUBFIND (Springel et al., 2001). We generate stellar equilibrium models of galaxies which we insert in the dark matter haloes of the original PHOENIX simulations at $z = 2$ and re-simulate the later evolution of the stellar and dark matter particles down to the present day. The star and dark matter particle resolutions are kept fixed, except that the softening for the stars and dark matter is kept fixed at a physical scale of 0.1 kpc corresponding to the physical softening that at $z = 2$.

6.2.2 Generating the stellar components and compound galaxies

The galaxies are represented by Hernquist (1990) spheres:

$$\rho_* = \frac{aM_*}{r\,(r+a)^3}, \tag{6.1}$$

where a is the scale radius which is related to the 3D half-mass radius through $a = r_e/(\sqrt{2}+1)$. The half-mass radius in projection is related to r_e through $R_e = 1.33\,r_e$

The N-body models for the stellar distributions are generated through a Monte Carlo sampling of a spherical distribution function (DF) of the form $f \equiv f(E)$ using a Neumann rejection technique (Kuijken & Dubinski, 1994; Kazantzidis et al., 2004). The DF takes the form:

$$f_*(\mathcal{E}) = \frac{1}{\sqrt{8}\pi^2}\int_0^{\mathcal{E}} \frac{\mathrm{d}\Psi}{\sqrt{\mathcal{E}-\Psi}}\frac{\mathrm{d}^2\rho_*(\Psi)}{\mathrm{d}\Psi^2} + \frac{1}{\sqrt{\mathcal{E}}}\frac{\mathrm{d}\rho_*}{\mathrm{d}\Psi}\bigg|_{\Psi=0}, \tag{6.2}$$

where $\Psi = -\Phi + \Phi_0$ and $\mathcal{E} = -E + \Phi_0 = \Psi - v^2/2$ are the relative potential (containing the contribution of both the dark matter and stars) and total energies respectively. The potential of the dark matter halo is modelled as a Hernquist sphere through a χ^2-fit to the spherically average density profile. Because the total potential is modelled as the superposition of two Hernquist profiles, the constant term in equation 2 drops out. While there are better ways to represent the potential of the dark matter haloes, we have found this approximation to be robust enough to produce stable galaxies (as will be shown later). Moreover, we note that it is often recommended to take into account of the Plummer softening when generating N-body models from distribution function based methods. However, in the case of the Hernquist profile, Barnes (2012) demonstrates that this does not make a difference provided that the softening length is smaller than the scale radius of the galaxy and that the inner-slope is not strongly cusped.

6.2.3 Stability Tests

We perform some stability tests to check whether our method works efficiently. We extract a subhalo identified with the subtructure finder SUBFIND Springel et al. (2001) from the cosmological dark-matter-only run and insert a spheroid with mass and size according to abundance matching and mass-size relations at $z = 2$. We then evolve the new system in isolation with a softening length of $\epsilon = 0.1$kpc for a period of 10 Gyr in Newtonian space. Such a case is shown in Figure 1. The dark matter quickly contracts due to the sudden presence of the stellar component on a timescale of 200 Myr, however the stellar component is more stable because of the inclusion of the host potential in initialising the particle velocities. This is shown in Figure 2. We also observe a flattening of the stellar components after revirialisation as shown in Figure 3. We have not attempted to prevent the rapid contraction of the dark matter component. Considering the current state of observations with respect to the properties of spheroids at $z = 2$ and the lack of information about the structure of their dark matter haloes, we believe our representation is adequate enough to study the evolution of the properties of our galaxies. Furthermore, the initial contraction of the dark matter should give us already a lower limit to the effect of dissipationless mergers. We anticipate that if the dark matter density profiles were kept intact or made shallower this would result in stronger effects than what we will see here.

The following method improves on past attempts at replacing dark matter haloes in cosmological runs with purely spherical systems. This is because the treatment between the model galaxies' boundaries with the rest of the cosmic web becomes ill-posed. In our experiment, the spheroids are included directly into the simulation and settle quickly into stable configurations after a few dynamical times, giving a more sophisticated treatment of the ICs, preserving the original structure of every dark matter halo (in terms of their subhalo population). It is because of the high-resolution achieved in dark matter only simulations today that we are able to perform such runs which were not possible in earlier studies (Dubinski, 1998; Rudick et al., 2006). Based on the series of tests performed for different galaxy stellar masses, we are able to follow reliably the structural evolution of galaxies with masses above $2 \times 10^{10} \mathrm{M}_{\odot}$ without the effect of two-body relaxation mitigating our results.

6.2.4 Initial conditions

Using the method described above, we populate every subhalo identified by SUBFIND in the original dark matter-only simulation susceptible to hold a minimum stellar mass of $m_* = 2 \times 10^9 \,\mathrm{M}.$. In our initial conditions we choose to represent a galaxy populations with structural properties that agree with numerous observational constraints. The stellar mass associated with each dark matter halo is chosen such as to reproduce the $M_{200} - m_*$ results from the abundance matching of Moster et al. (2013). The size of a galaxy is set to follow either the mass-size relation for red compact massive quiescent galaxies or that of extended blue star forming galaxies. The distinction between red and blue galaxy is made in a probabilitistic way using the observed fraction of quiescent $z = 2$ galaxies as a function of stellar mass $q \equiv q(m_*)$ from Muzzin et al. (2013) which extends down to $10^{10} \,\mathrm{M}_{\odot}$. Below a stellar mass of $10^{10} M_{\odot}$ the sizes are selected according to the observed scatter in the mass-size diagram of galaxies (which is substantial).This is shown in Figure 4.

Although we are representing all galaxies as spheroids, our experiment is still aimed at addressing a well posed dynamics problem and the spread in sizes we have generated already encapsulates already much of the complexity of galactic structure on the galaxy population at $z = 2$. The galaxies are placed at the centre of the potential $\mathbf{x}_{\mathrm{pot}}$ of every dark

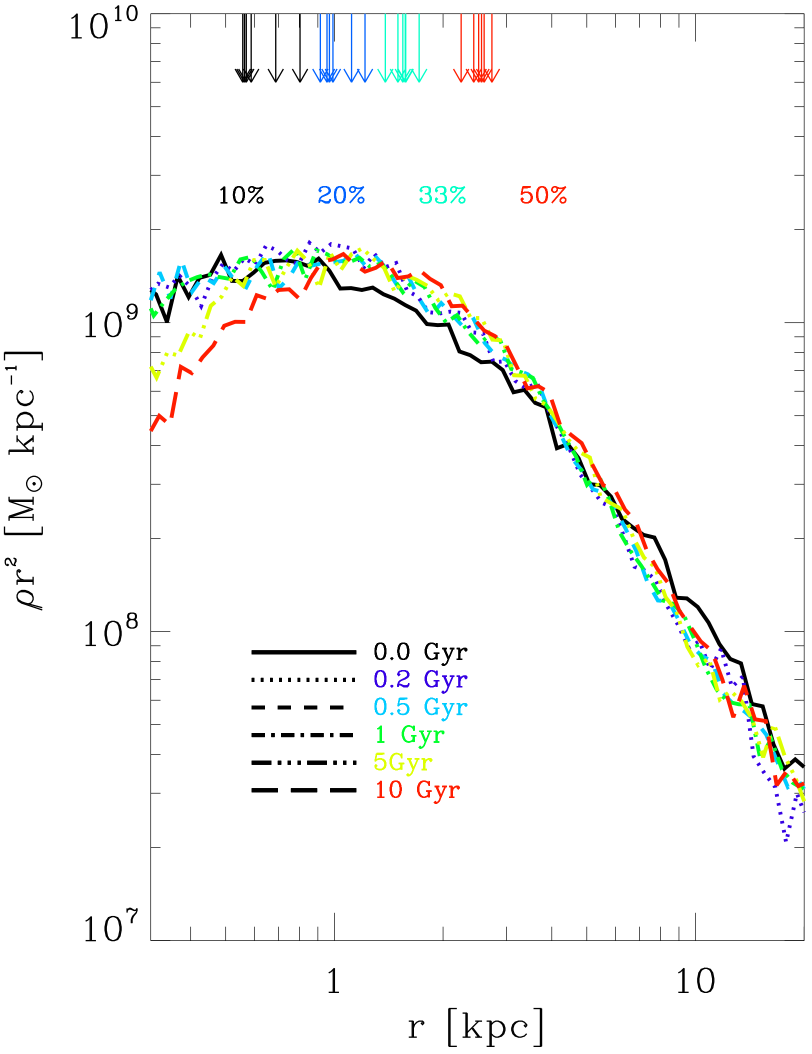

Figure 6.1: Stellar density profile as part of our stability test. Using the machinery described above, we introduce a stellar component in a live dark matter halo which we evolve in isolation. The system undergoes a rapid phase of re-virialisation which changes slightly the stellar density profile shape. However, it then stays constant during the next 10 Gyr of evolution in isolation. The arrows mark the radii enclosing 10, 20 33 and 50 percent of the light, these increase as time increases (0.0, 0.2, 0.5, 1, 5 and 10 Gyr). The size change impeded by the re-virialisation process is of order 5 percent proving the stability and robustness of our method to generate spheroids in cosmological dark matter haloes. This galaxy has a dark halo mass of $M_h = 7 \times 10^{12}\,\mathrm{M}_\odot$, stellar mass of $M_* = 9 \times 10^{10}\,\mathrm{M}_\odot$ and half-light radius of $r_e \sim 2\,\mathrm{kpc}$

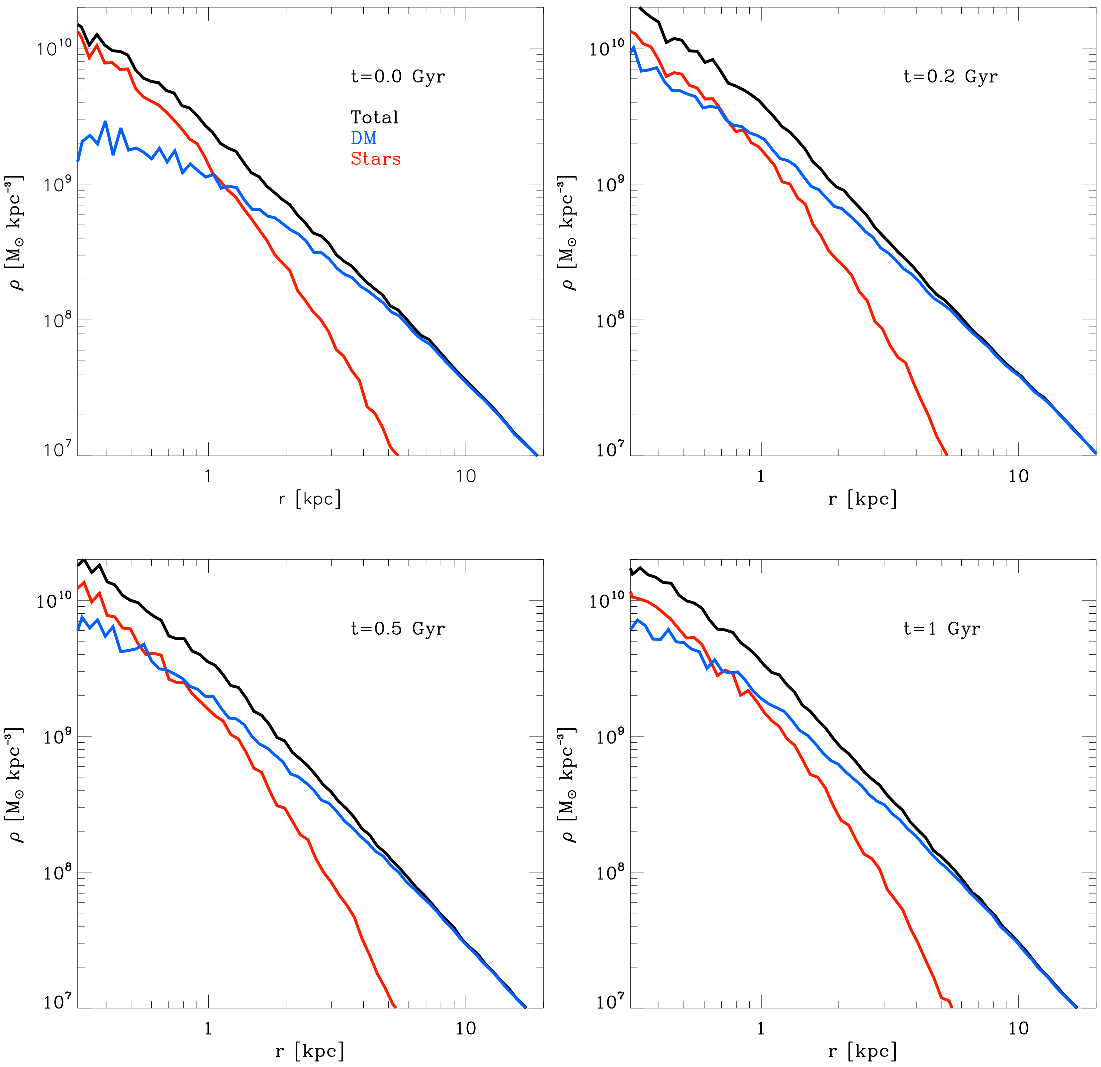

Figure 6.2: Evolution of density profiles from our stability test for the different components: dark matter (blue), stars (red), total (black). The system stabilises quickly with the dark matter contracting on a timescale of $t \sim 200$ Myr and then remaining intact subsequently.

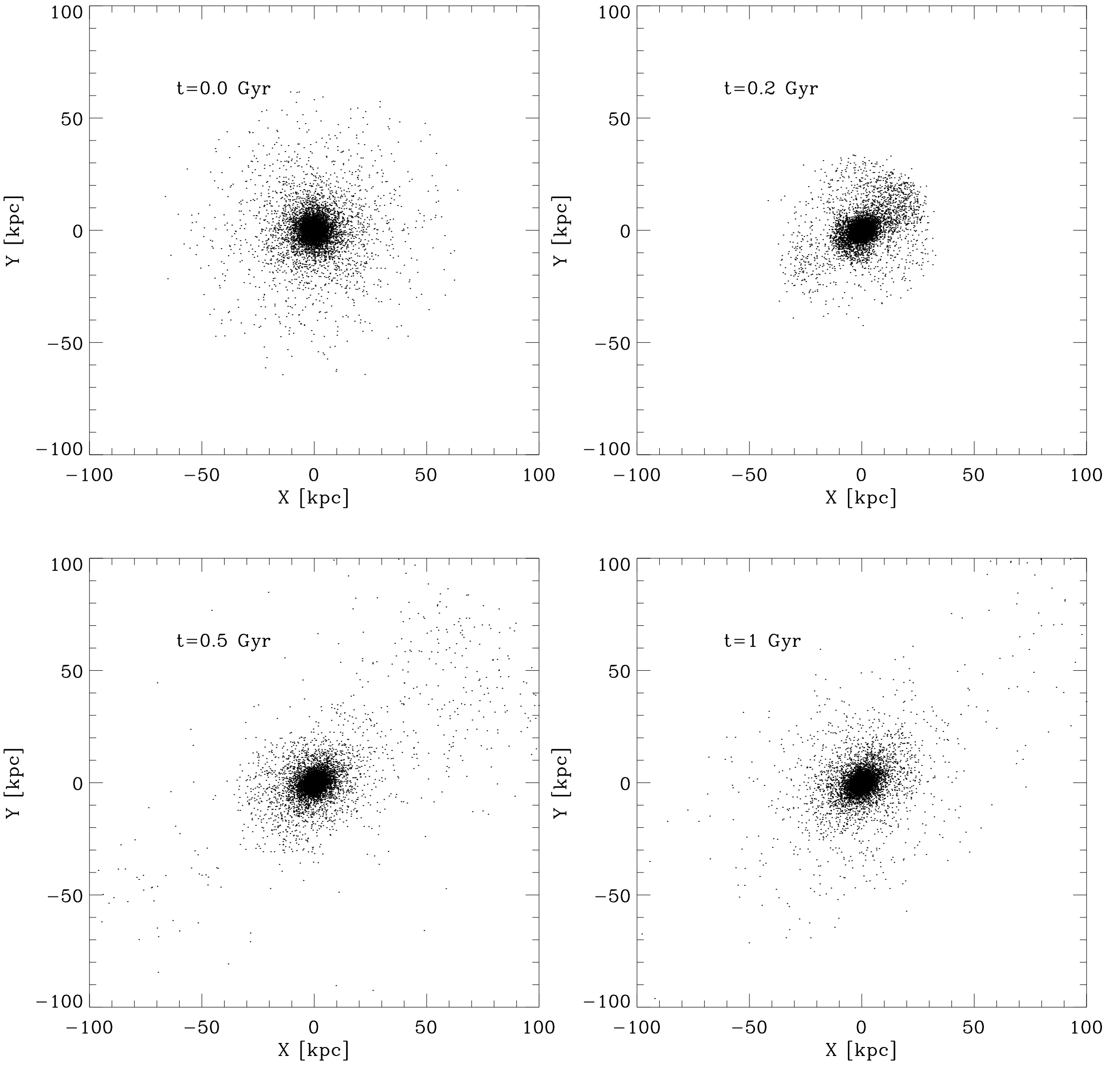

Figure 6.3: Projections of the same stellar component as in Figure 1 and 2 showing the flattening of the stellar component induced by the re-virialisation process. The stellar component is placed at the centre of the most bound dark matter particles (bottom of the potential). The velocity of the dark matter halo particles are also re-adjusted to be in the frame of the 100 most bound dark matter particles. The image illustrates that the complicated phase-space structure of real dark matter haloes can affect some of the outer regions of the galaxy during revirialisation, however this is only true for a negligible amount of stellar mass.

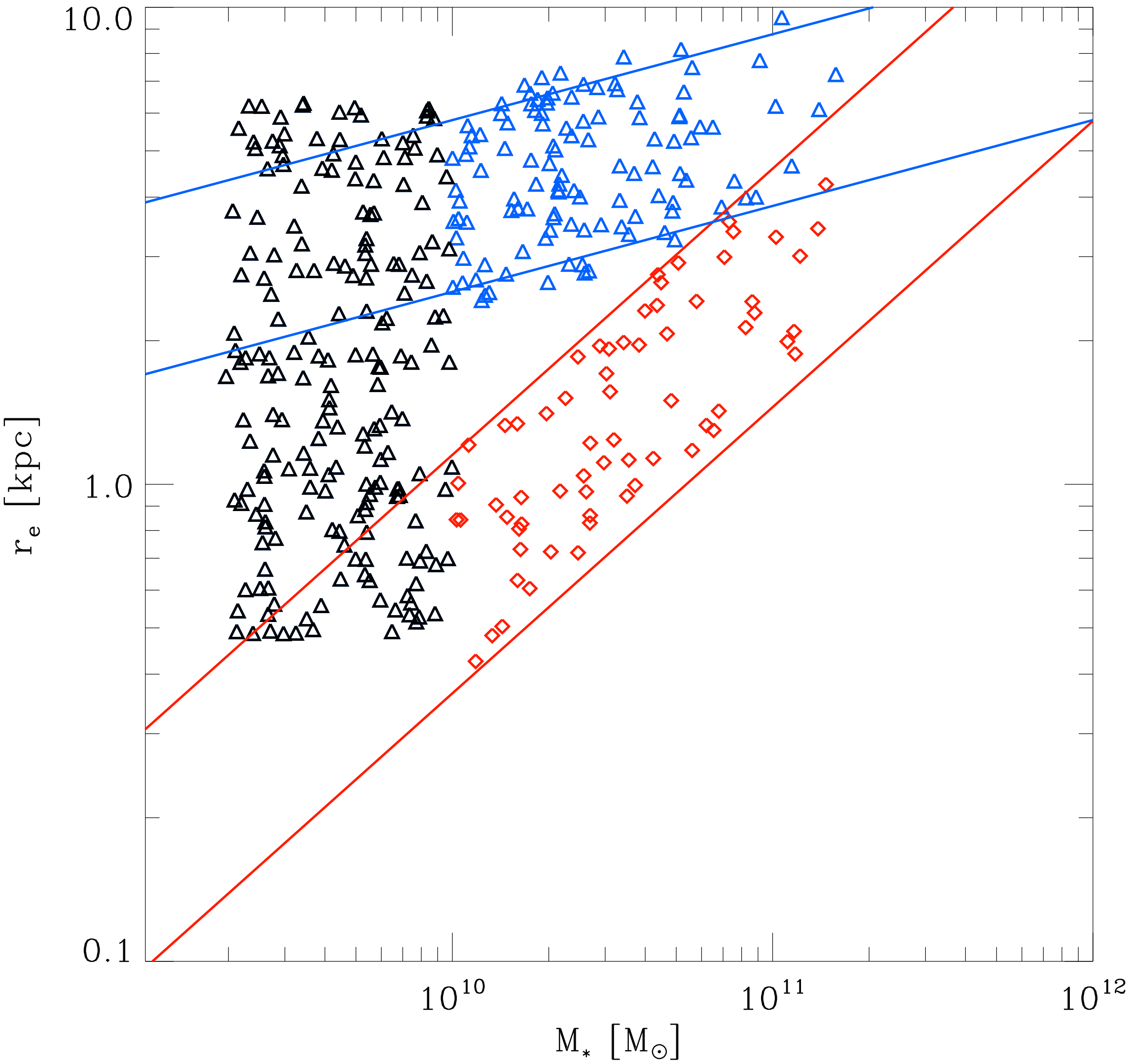

Figure 6.4: Mass-size relation of our galaxies. Red symbols belong to the compact massive quiescent galaxies class while the blue ones belong to the massive star-forming galaxies class. Below 10^{10} $M_\odot$, the observations are uncertain so we mimic the observed scatter in sizes (black triangles).

Run	M_{200} $h^{-1}\mathrm{M}_\odot$	c	R_{200} h^{-1}Mpc
Ph-C-2	5.495×10^{14}	5.11	1.386
Ph-E-2	5.969×10^{14}	5.19	1.369

Table 6.1: Basic structural properties (virial mass M_{200}, concentration c and virial radius R_{200}) of the Phoenix clusters at $z = 0$ from the original dark matter only simulations.

matter halo and their velocity are recentred according to the centre of velocity calculated around $\mathbf{x}_{\mathrm{pot}}$.

6.2.5 Cluster simulations

We choose to run two cluster re-simulations from the Phoenix suite. These are the Ph-E and Ph-C haloes for which we summarise their properties in Table 1. Before we begin to present our re-simulations' results, it useful to ask ourselves where did the particles constituting the central $r < 10$kpc regions of the galaxy clusters come from? This is shown in Figure 5, which illustrates the fact that the central regions of BCGs are significantly shaped by multiple mergers which was already noted in Gao et al. (2004).

6.3 Structure of galaxy clusters

6.3.1 Density profiles

In this section we present the density profiles for the stellar, dark and total matter components in our runs. We also compare those to their dark matter counterparts. This is shown in Figure 6, where we show the normalised $\rho r^2/(\rho_{200} r_{200}^2)$ profiles as a function of normalised virial radius r/r_{200}. Overplotted in this figure are the profiles derived in Newman et al. (013a,b). The first result to note is that the total density profiles in the dark matter only and two collisionless fluids run look very similar (almost identical, except in the inner-most regions of the dominant galaxy). This already suggest that the attractor hypothesis has been at work. The dark matter on the other hand shows a dip starting at a scale coincident with $r/r_{200} \sim 0.01 - 0.02$ from centre of the final merger remnant. The stellar density profile is also in reasonable agreement with the stellar profiles measured by Newman et al. (013a). Note that this result came as to assume a purely dissipationless formation channel from $z = 2$ to $z = 0$ for the BCG. This suggests that star formation may not play such an important role in the formation of BCGs.

In Figure 7, we present the slopes of the density profiles defined as $\gamma = -\frac{\mathrm{d}\ln(\rho)}{\mathrm{d}\ln(r)}$. These are plotted as a function of normalised virial radius r_{200}. In computing the slopes we have binned our data between $r = 0.1$ kpc and $r = 1000$ kpc into logarithmic bins of width $\Delta\log(r) = 0.1$. We have tried other ways of binning the data and they all lead to the same consistent result. Overall, the slope of the stellar profiles are consistent with the those

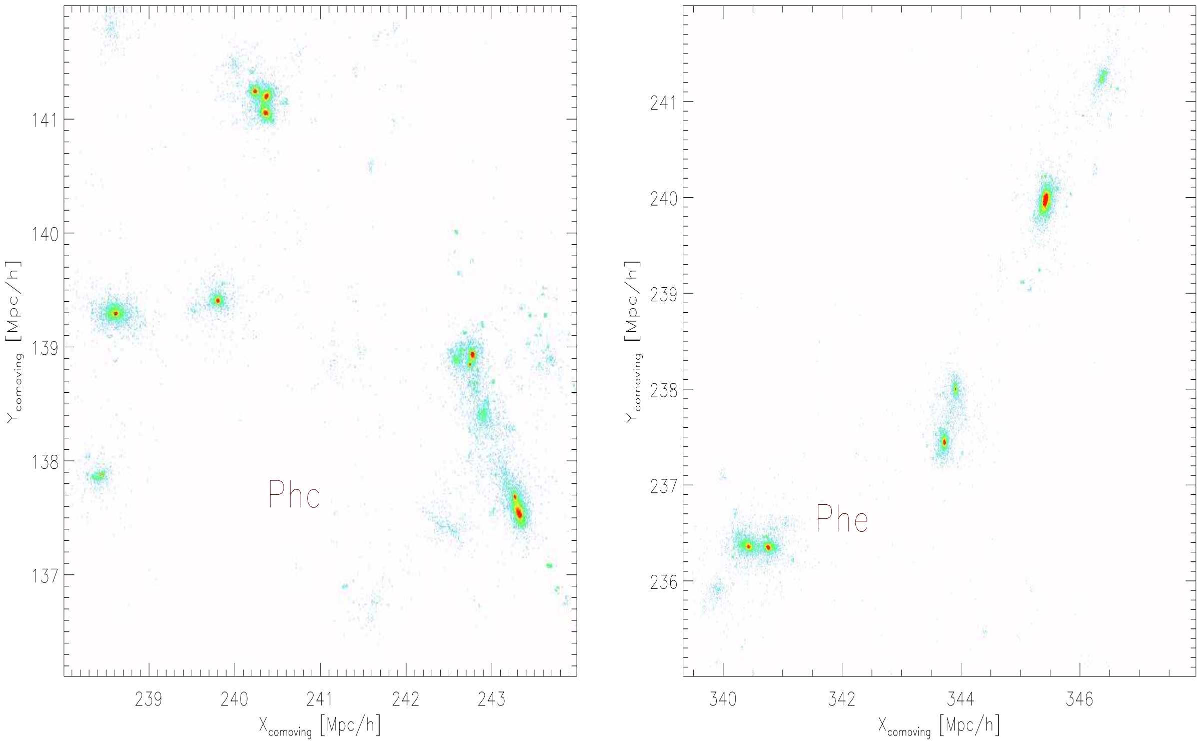

Figure 6.5: Distribution of dark matter particles identified in the original *Phoenix* simulations making up the central 10 kpc of the galaxy clusters at $z = 0$ tracked at $z = 2$. This illustrates that the central region of galaxy clusters are not always fully assembled by $z = 2$.

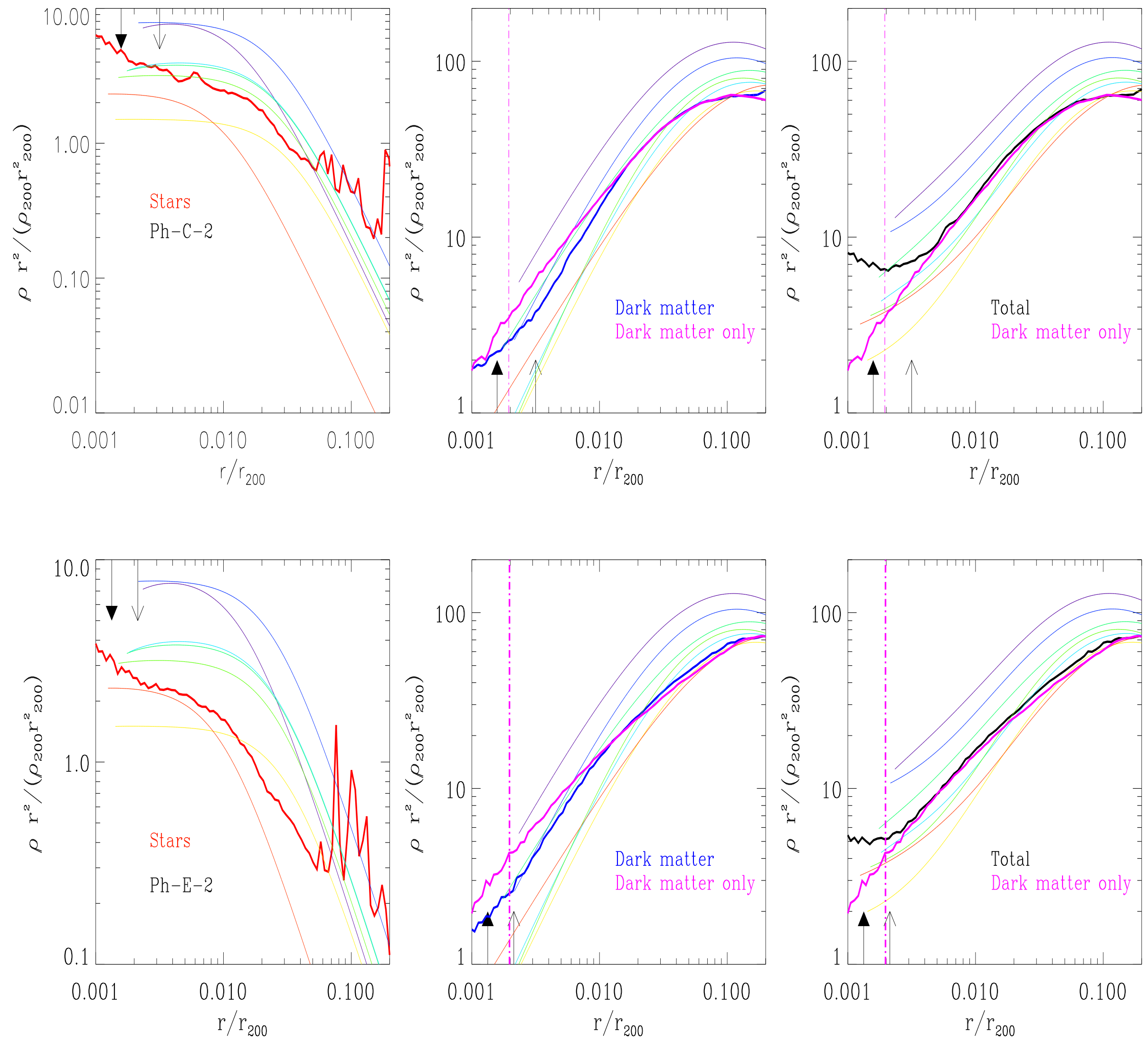

Figure 6.6: ρr^2 profiles for the clusters normalised by $\rho_{200} r_{200}^2$ as a function of normalised radius r/r_{200} for the stars (left panel in red), dark matter (middle panel in blue) and total matter (right panel in black) respectively. The coloured lines in the last two panels represent the profiles from Newman et al. (2013a,b). The magenta lines correspond to the dark matter density profile curves from the original dark matter runs (omitting baryonic loading). The inclusion of stars clearly caused the central dark matter to drop in the inner already within $r \sim 10\,\mathrm{kpc}$. When looking at the total mass profiles, the dark matter only and our re-simulation curves do not change much even within the half-light radii of the galaxies. This suggests an attractor solution that is validated already below the half-light radius of the final galaxy. The two black arrows mark the two radii where a mass deficit should be expected due to black hole mergers for our most conservative estimate and slightly more relaxed one (see discussion in section 6.4).

measured, except that there may be a systematic shift at lower radii $r/r_{200} < 0.002$. The slope of the dark matter density profiles in the from the re-simulations are systematically shallower than those of the dark matter only runs. The transition scale where these become shallower than the NFW asymptotic solution (represented by the horizontal dash-dotted line) occurs at $r/r_{200} \sim 0.01$ which is also coincident with that in observations $0.01 < r/r_{200} < 0.03$. Turning to the total density profiles, these also match those observed by Newman et al. (013a) and they follow closely the profiles from the dark matter only runs. It seems that the enough mixing has occured in the central region of the cluster to give rise to an attractor solution which extends further into the half-light radius of the BCGs.

6.4 Mergers, mass re-shuffling & dark matter heating

Ph-E-2 Make a new plot for the C halo taking the z=0 solution in too.

Ph-C-2

Between $z = 2$ and $z = 1.0$ the most massive progenitor is interacting with a number of galaxies which constantly reshape the slope of the dark matter density profile. At $z = 1.0$, one galaxy eventually mergers to the centre and the system is relaxed with a slope of a dark matter density profile which is already substantially shallow (see Figure 11). Between a few other galaxies orbits about the central 50 kpc of the most massive progenitor heating the dark matter until one eventually merges and relaxes preserving a shallower dark matter density profile. The final merger by $z = 0$ also preserves this shallow dark matter cusp and extends it further innerwards.

A number of important features should be noted. The identity of the particles making up the central stellar/dark matter density distribution changes during the merger processes. This is made clear by following the distribution of particles making the central stellar/dark matter distribution of the most massive progenitor of the galaxy cluster at $z = 2$ (shown by the black solid thick line). Through the subsequent mergers, this distribution gets pushed out to be replaced by the new incoming material associated with the infalling galaxies. We also show the associated slope of the dark matter density profile.

Moreover, the change in the slope of the dark matter is mostly related to mergers bringing a considerate amount of stellar material towards the centre of the cluster pushing against the existing central density distribution (this is shown further in FIgure YYY). We see that the BCG underwent numerous mergers (6 or 8 depending on the cluster re-simulation) and not all of them were effective enough in creating an appreciable change in slope of the dark matter. This is related to their initial density profile. We distinguished the mergers which pushed dark matter out and those which did not and tracked the structural information of the galaxies at z=2. The distinction between satellite and centrals is also made through the use of different line styles. Thus multiple mergers are not a sufficient condition to guarantee a change in the slope of the dark matter density profile. The origin of the shallow dark matter cusps is clearly related to the dynamical friction exerted by the infalling galaxies on the surrounding dark matter. However it is important to note that this process not only brings stars to the centre of the central galaxy, but also the dark matter

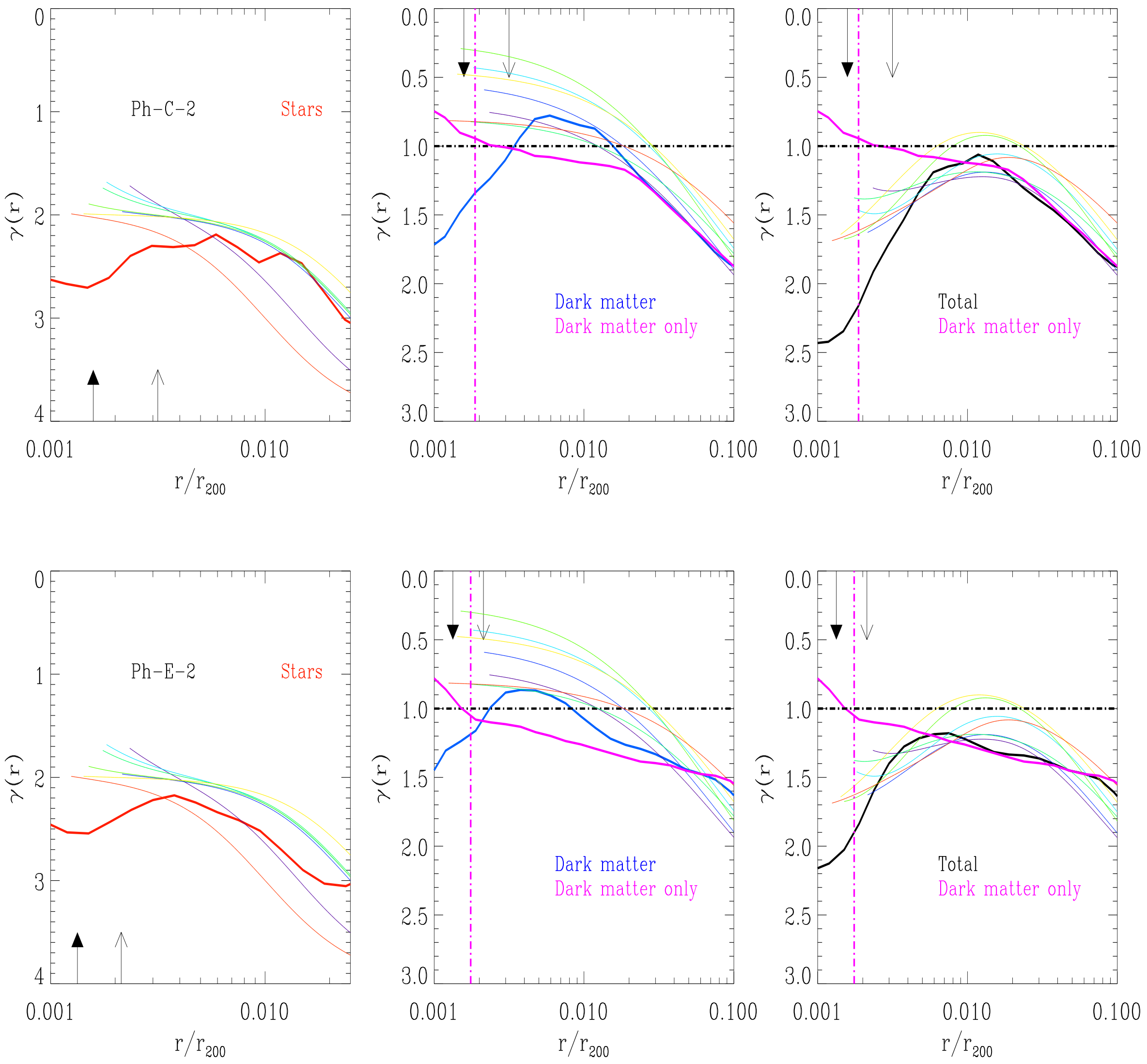

Figure 6.7: Slopes of the different components as a function of normalised radius r/r_{200}. The coloured lines are the slopes obtained from the analysis of Newman et al. (2013a,b). The agreement between the re-simulations and measured total matter slope is reasonable. The dark matter profile (blue line) is shallower than the dark matter only runs (magenta line) and the scale at which these become less than $\gamma = 1$ is coincident with the scale from Newman et al. (2013b), coincident with a physical radius of $r = 10$kpc while the stars are still as steeply cusped as found in Newman et al. (2013b). Given that the galaxies started with inner dark matter density profiles *steeper* than the original NFW solution from the dark matter only run, the effect seen here would be enhanced for galaxies in which a phase of contraction would have been avoided (due to baryonic processes). The two black arrows mark the two radii where a mass deficit should be expected due to black hole mergers for our most conservative estimate and slightly more relaxed one (see discussion in section 6.4).

associated with the cores of the merging galaxies. This interplay between accreted/expelled dark matter creates dark matter cusps which are not as shallow as reported by previous simplified studies. It is of interest to study the effect of early baryonic feedback on the structure of the galaxies at z=2 as the slopes reported in here would be shallower. This has as already been shown qualitatively in the study of Laporte et al. (2012). This will be explored in the future.

In a study on phase-mixing, ?) argued as an extension to mixing theorems that the steepest cusps always survive in mergers. This seems to be the case, however, when decomposing the system into dark and stellar matter, this of course cannot hold longer because of the mixing between species. This is because the stars are on higher binding energy orbits and have higher densities that the background and thus can efficiently exert dynamical friction on the surrounding dark matter leading to slopes that are *shallower* than the dark matter only runs. It must be stated there is nothing surprising in the slope of the dark matter to be shallower than the dark-matter only run in the run with baryonic loading (which also induced a steepening of the dark matter density profiles in the progenitor galaxies). Our experiment hints that there may be an attractor solution to collisionless systems however in order to test this rigorously one must show that the multiple merging of r^{-2} haloes should lead to a r^{-1} solution. This problem although trivial in its essence cannot be addressed properly with N-body simulations due to the inherent problems with softening leading to incorrect dynamics at the centre of the galaxies although stable models can be constructed (Barnes, 2012).

6.5 On the contribution of super-massive black-holes

Given the substantially high number of mergers occurring in the formation of BCGs in ΛCDM, it is worthwhile to further consider the effect of black-holes on the central distribution of dark and stellar matter in such objects. While this current experiment does not take into account the presence of supermassive black-holes in the progenitor galaxies, we can still use the information about galactic structure in the initial conditions and the subsequent merger events to make an estimate of their potential importance in re-distributing matter below 3kpc (omitting the complications of dynamics due to recoils and unstable situations like those of multiple black-hole systems). This calculation should only serve as an order of magnitude estimate.

The BCG in Ph-E has experienced 8 mergers, with 6 which have brought much stellar material to the centre of the galaxy. Given the progenitor galaxies' initial stellar masses we estimate their expected host blackhole masses. This is done through the relation published in Bennert et al. (2011): $\log(M_{BH}) = \alpha(\log(M_*) - 10) + \beta\log(1+z) + \gamma + \sigma + 8$, with $\alpha = 1.09$, $\beta = 1.96$, $\gamma = -0.48$, $\sigma = 0.36$. Merritt (2006) studied through N-body simulations the effect of the mass deficit impeded by binary supermassive black holes and further quantified the magnitude of such deficits in relation to the merger history of galaxies. He found that $M_{\rm def} \sim 0.5M_{12}$ with M_{12} the total mass of the binary and that this result depended weakly on the mass ratio $q = M_1/M2$ of the black holes or on the galaxies' nuclear density profiles. Assuming that after every each subsequent mergers with $M_2 << M_\bullet$ black holes coalesce to a new binary, he quantified the magnitude of the cumulative mass deficit finding that $M_{\rm def} = 0.5NM_\bullet$, where N is the number of mergers and $M_\bullet$ is the final mass of the black hole. We begin by summing the mass of all the black holes in the progenitor galaxies which merge to the centre of the BCG and compare it to the enclosed total mass within 3,2,1 kpc. If all black-holes were to merge the final black-hole mass for the BCG in Ph-E would be $M_{BH} = 6.0 \times 10^{10}\mathrm{M}_\odot$. We will assume that after the first merger, a binary blackhole is formed with mass $M_{12} = M_1 + M_2$. In this case $M_{12} = 2 \times 10^{10}\mathrm{M}_\odot$. We also note that the subsequent black-holes which will merge to the centre of the BCG have $M << M12$. So given that $N = 3-5$ mergers occured at the centre of the BCG, our estimated deficit mass would be $M_{def} \sim 0.5NM_\bullet \sim 6.4 - 15 \times 10^{10}\mathrm{M}_\odot$. This could easily account for a core radius up to 3kpc given that the structure of the merger remnant has $M(r < 3\mathrm{kpc}) = 1.4 \times 10^{11}\mathrm{M}_\odot$. Such large cores are visible in some BCGs (Postman et al., 2012) and such objects may be well accounted for in ΛCDM.

Proceeding in a similar way for Ph-C, we identify between 5 mergers (if more than a third galaxy mass is identified within 20kpc of the final merger remnant, if we relax this to a tenth then this number goes up to 8). For the initial conditions considered here this would amount to a final black hole mass of $M_\bullet \sim 5 - 7 \times 10^{10}\mathrm{M}_\odot$. This would amount to a mass deficit of $M_{def} \sim 0.5NM_\bullet \sim 12 - 28 \times 10^{10}\mathrm{M}_\odot$. Taking our most conservative estimate this is also enough to explain core sizes as large as 3kpc and based on our upper-limit, might also have some implications for the matter distribution out to 6 kpc, given that $M(r < 6\mathrm{kpc}) = 28 \times 10^{10}\mathrm{M}_\odot$. We show the radii where mass deficits can affect the distribution of matter in Figures 6.6 and 6.7 for both clusters.

We stress however, that although this estimate relies on a strong assumption, namely that the black holes coalesce before the next merger. This certainly may not be the case and one would expect a triple black-hole system which would get ejected by the gravitational slingshot Mikkola & Valtonen (1990) which would lead to smaller values of $M_\bullet$ but larger values of M_{def} because multiple black hole systems are more efficient than a binary to move stars around. Another possibility is that of the gravitational rocket effect which could give kicks to a coalescing binary up to ~ 250km/s which may give rise to mass deficits as large as $\sim M_\bullet$ (Merritt et al., 2004; Boylan-Kolchin et al., 2004). Gas which may be expected in some of the progenitor galaxies (given the constraints on the fraction of quiescent galaxies (Muzzin et al., 2013)) could however help coalescence of some binary black holes, but also promote the formation of stars: this would lead to smaller mass deficits. However, it could also be that such star-forming galaxies may be transformed into red dead ellipticals by the time of the merger, which would certainly lead to a cumulation of dissipationless mergers.

Given the results of our experiment and our back of the envelope calculations, black holes will play an important role in the re-distribution of matter already within 3 kpc of the BCGs (but also perhaps up to 6kpc). This will have important consequences for the distribution of matter within the inner-most regions of the cluster (both dark and stellar matter) and the expected dark matter annihilation signal. The inclusion of black-holes at the centre of galaxies will bring an additional source of dynamical friction affecting the inner dark matter and stellar distributions. This is beyond the current scope of this paper

Run	$M_{1\mathrm{kpc}}$ $\mathrm{M}_{\odot}$	$M_{2\mathrm{kpc}}$ $\mathrm{M}_{\odot}$	$M_{3\mathrm{kpc}}$ $\mathrm{M}_{\odot}$	$M_{4\mathrm{kpc}}$ $\mathrm{M}_{\odot}$	ΣM_{BH}
Ph-C-2	4.3×10^{10}	1.0×10^{10}	15.0×10^{10}	19.6×10^{10}	$(4.8 - 7.3) \times 10^{10}$
Ph-E-2	2.6×10^{10}	6.5×10^{10}	13.7×10^{10}	18.7×10^{10}	$(4.2 - 6.1) \times 10^{10}$

Table 6.2: Enclosed total masses within $r = 1, 2, 3, 4$kpc compared to the sum of all black holes in the BCG progenitor galaxies.

but will be addressed in a future paper where we update our initial conditions generator for creating stable (distribution function generated) N-body galaxy models with black holes (Laporte & White in prep).

6.6 Discussion

Previous studies have considered the effect of dynamical friction due to galaxies as they merge to the centre of galaxy clusters. However, these were highly unrealistic for several reasons and not able to address the problem robutsly as we will argue here. Massive point masses of $10^{11} M_{\odot}$ were used to represent galaxies, this is already a dangerous approximation because it completely ignores the fact that galaxies can get stripped El-Zant et al. (2004). Moreover, the numbers of such clump galaxies considered in such experiments had no physical motivation and arbitrary. Later experiments considering strippable galaxies would ignore the presence of dark matter haloes around them in the initial conditions thus already biasing heavily results towards efficient dark matter heating (Nipoti et al., 2004). Finally, previous cosmological N-body simulations have used initial conditions in very stark contradiction with observational constraints on the stellar mass function and mass-size relation of galaxies at high redshift (Ruszkowski & Springel, 2009). This meant that only qualitative behaviours could be studied (Laporte et al., 2012). Our current experiment does not suffer from any of those caveats or strong approximations and we are able to robustly test the importance of mixing processes at the centre of galaxy clusters in a cosmological context. Our results are based on the assumption that the later assembly at the centre of galaxy clusters is entirely orchestrated by collisionless mergers. This makes the problem well-posed and addressable through the N-body method. The fact that it reproduces observed structural trends from massive clusters which include both cool and non-cool core clusters hints that this may indeed be relevant for all galaxy clusters. Finally, our experiment also shows that all previous studies over-estimated the net effect of dynamical friction heating in galaxy clusters.

Lately there have been simulation attempts at incorporating the effect of AGN feedback to study its effect on the distribution of matter on the scale of clusters (Martizzi et al., 2012; Dubois et al., 2013). However, a number of outcomes are clearly problematic in those studies. As an example, the latest simulations of Martizzi et al. (2012) of a massive galaxy clusters which produced a cored dark matter density profile in their run with AGN feedback. However, it is important to note that the dark matter core size produced in their cosmological run coincides exactly with the core size produced in their stellar density profile. Such large stellar cores are clearly not present in the observations of Newman et al. (013a) (see Figure 6 top left panels). While AGN feedback activity may change the distribution of dark matter in the progenitor galaxies of BCG at $z = 2$, it cannot be responsible for setting the dark matter core sizes at later times. If AGN is indeed active at all times, both the stars and dark matter would behave similarly, which is exactly the result which was recovered in the cosmological run of Martizzi et al. (2012). The picture we are presenting here is consistent in the sense that the stars have much higher binding energy than the dark matter and this enables them to scour the central dark matter to produce shallow dark matter cusps of sizes $r \sim 10kpc$ while still preserving steep enough stellar density profiles within the $3 - 10kpc$ regions of the cluster profile as expected from observational constraints (Newman et al., 013b).

Our simulations manages to isolate the most relevant process shaping the central regions of galaxy clusters *at late times*: dissipationless mergers. The effect of these mergers is different on both the dark matter and the stellar matter content. Together with our study on the structural assembly of BCGs through galactic cannibalism (Laporte et al., 2013) motivated by predictions of semi-analytic models (implying an assembly mainly orchestrated by dissipationless mergers) we have presented a consistent picture for BCG formation which solidifies some of the early proposed scenarios for their formation (Ostriker & Tremaine, 1975; White, 1976). It remains to be seen whether hydrodynamical simulations will be capable to make robust predictions on the initial dark matter structure of the progenitor galaxies at $z = 2$ while reproducing similarly stellar properties consistent with the increasing $z = 2$ observational constraints. This would be a great subject of research for the coming years which will rely on observational advances in instrumentation to study resolved kinematics of $z = 2$ massive quiescent galaxies.

Our initial conditions were created through impulsively adding stars at the centres of dark matter haloes. This in effect causes a phase of re-virialisation resulting into a contracted dark matter halo. There are candidate mechanisms which may actually prevent the dark matter density profile to contract (supernova feedback or perhaps more relevant AGN feedback). We are however affected by our lack of understanding on the available energetics which forces us to only consider ad-hoc parameters to make the dark matter density profiles shallower in the progenitor galaxies. Nonetheless, it is clear that in those instances the effects seen in our simulations will be amplified and subsist all the way down to $5-4$kpc. The fact that we started with dark matter density profiles which were already steeper than their dark matter only simulation counter-parts adds much more credibility to the role of multiple dissipationless mergers in shaping the central dark matter distribution in galaxy clusters. This is why we have deliberately not tried to temper with the dark matter distribution in the initial conditions.

Below $r \sim 4kpc$ our simulations are most likely inadequate to predict the density structure of matter. However, we were able to estimate the expected amount of matter that could get evacuated due to black hole mergers. These would most probably scour out further the dark matter and stars below a scale coincident with $r \sim 3$kpc and influence perhaps larger radii ($r \sim 6$kpc). This would have important implication on the annihilation signal from dark matter at the centre of clusters Gao et al. (2012). The high-number of mergers identified in our simulations also suggest a natural explanation for the largest stellar core sizes observed in some BCGs Postman et al. (2012). It would be of interest to use such results from cosmological simulations to study the formation of stellar/dark cores in the inner-most regions of the Brightest Cluster Galaxies. This would have also important repercussions on the gravitational wave signal expected in those objects. This is currently being investigated (Laporte & White in prep). Finally, relating our observations to the phenomenology observed in cosmological hydrodynamical simulations would be of interest and is indeed under way (Schaeller et al. in prep).

6.7 Conclusion

We have presented a series of collisionless N-body simulations of the late assembly of galaxy clusters from $z = 2$ to $z = 0$. These simulations provide the first quantitative confirmation of an attractor-like solution in galaxy clusters as proposed by Loeb & Peebles (2003) down to scales of $r/r_{200} \sim 0.002 - 0.003$. It is yet to be seen whether supermassive black holes could provide another source for dynamical friction heating of the dark matter (and stars) further extending this range. Although some qualitative work has been carried in the past, it was not obvious whether upon baryon loading the total density profiles would go back to the dark matter only result (Gao et al., 2004). We show that dissipationless mergers are indeed able to produce shallow dark matter cusps in galaxy clusters consistent with the recent detailed study of Newman et al. (013b). The radius of transition below the NFW solution in our simulations occurs at $r/r_{200} \sim 0.1 - 0.2$ similar to that in observations.The difference in slopes achieved between the runs with and without initial baryonic loading are of the order $\Delta\gamma \sim 0.3 - 0.4$. Multiple dissipationless mergers can have a strong effect on the dark matter while still leaving stellar cusps intact making them ideal candidates to explain the observed distribution of matter in galaxy clusters. If baryonic physics at high redshifts is able to alter the density structure of dark matter to shallower density profiles, we expect greater depressions than those observed in the simulations. Early feedback may change the original structure of the dark matter density profile in the BCG progenitor galaxies (Dubois et al., 2013) but such processes cannot be relevant at later times because they would affect both the stars and dark matter in the same way, which observations suggest is not the case. Based on the high number of mergers occuring at the centre of the cluster we argued that black holes could play a major role in shaping the inner-distribution of matter below $3-4kpc$. In a future contribution, we shall address this problem to further study the inner-distribution of matter in clusters in relation to the observed mass-deficits in massive BCGs and the expected dark matter annihilation signal in galaxy clusters.

Chapter 7

Measuring the slopes of mass profiles for dwarf spheroidals in triaxial CDM potentials

We generate stellar distribution functions (DFs) in triaxial haloes in order to examine the reliability of slopes $\Gamma \equiv \Delta \log M / \Delta \log r$ inferred by applying mass estimators of the form $M \propto R_e \sigma^2$ (i.e. assuming spherical symmetry, where R_e and σ are luminous effective radius and global velocity dispersion, respectively) to two stellar sub-populations independently tracing the same gravitational potential. The DFs take the form $f(E)$, are dynamically stable, and are generated within triaxial potentials corresponding directly to subhaloes formed in cosmological dark-matter-only simulations of Milky Way and galaxy cluster haloes. Additionally, we consider the effect of different tracer number density profiles (cuspy and cored) on the inferred slopes of mass profiles. For the isotropic DFs considered here, we find that halo triaxiality tends to introduce an anti-correlation between R_e and σ when estimated for a variety of viewing angles. The net effect is a negligible contribution to the systematic error associated with the slope of the mass profile, which continues to be dominated by a bias toward greater overestimation of masses for more-concentrated tracer populations. We demonstrate that simple mass estimates for two distinct tracer populations can give reliable (and cosmologically meaningful) lower limits for Γ, irrespective of the degree of triaxiality or shape of the tracer number density profile.

7.1 Introduction

The Milky Way's dwarf spheroidal (dSph) satellites include the most dark-matter-dominated galaxies known, with dynamical mass-to-light ratios ranging from order ~ 10 to several hundreds in solar units (Mateo, 1998). This makes dSphs objects of prime interest for studying the distribution of dark matter in galaxies. dSphs lack atomic hydrogen; therefore methods for measuring dSph masses must rely on the kinematics of their pressure-supported stellar populations. In the past decade, many techniques have been developed with the goal of determining the internal mass distributions of dSphs: spherical Jeans modelling (okas & Mamon, 2001; Strigari et al., 2006, 2008; Koch et al., 2007; Battaglia et al., 2008; Walker et al., 2009; Wolf et al., 2010), phase-space modelling (Wilkinson et al., 2002; Amorisco & Evans, 2011), the multiple stellar populations method (Walker & Peñarrubia, 2011), the use of the virial theorem for spherical and constant flattened systems (Agnello & Evans, 2012) as well as axisymmetric Jeans modelling (Hayashi & Chiba, 2012) and Schwarzschild modelling (Jardel & Gebhardt, 2012; Breddels et al., 2012).

Complicating most analyses is the fact that the inferred dynamical mass is degenerate with the anisotropy of the velocity dispersion tensor and the latter is poorly constrained by available line-of-sight velocity data. While this degeneracy leaves the full mass profile underconstrained in a standard Jeans analysis (Strigari et al., 2006; Walker et al., 2009), its relative weakness near the halflight radius of the stellar tracer makes estimates $M(R_e) \propto \kappa R_e \sigma^2$ (where R_e and σ are luminous effective radius and global velocity dispersion, respectively, and κ is a constant) robust to various forms of anisotropy and/or even to the shape of the mass profile (Walker et al., 2009; Wolf et al., 2010).

The presence of at least two chemo-dynamically distinct stellar subpopulations in several dSphs (Tolstoy et al., 2004; Battaglia et al., 2011) then provides a unique opportunity to measure the slopes of dSph mass profiles, $\Gamma \equiv \Delta\log M/\Delta\log r$, directly by estimating $M(R_e)$ at two different effective radii. Walker & Peñarrubia (2011, 'WP11' hereafter) introduce a statistical method that uses estimates of stellar positions, velocities and metallicities to estimate R_e and σ for each of two stellar subpopulations within the Fornax and Sculptor dSphs, obtaining $\Gamma = 2.61^{+0.43}_{-0.37}$ and $\Gamma = 2.95^{+0.51}_{-0.39}$, respectively. Taken at face value, these measurements exclude, with significance $\sim 96\%$ and $\sim 99\%$, respectively, the Navarro, Frenk & White (1997, 'NFW' hereafter; $\Gamma \leq 2$ at all radii) profile that is often invoked to characterise density profiles of cold dark matter (CDM) halos formed in dissipationless cosmological simulations. WP11 tested their method against spherical dynamical models with various degrees of anisotropy and found that mass estimators of the form $M(R_e) \propto R_e \sigma^2$ systematically overestimate the enclosed mass more strongly for tracers that are more deeply embedded (i.e., more concentrated) in their host haloes. This bias implies that slopes $\Gamma \equiv \log M/\Delta\log r$ tend to be systematically *underestimated*, such that WP11's claim of their quoted levels of NFW exlcusion were conservative.

However, despite the assumption of spherical symmetry that is common to most dSph studies (exceptions include the axisymmetric Schwarzschild analyses of Jardel & Gebhardt 2012 and the flattened models considered by Agnello & Evans 2012), the composite stellar populations of real dSphs are clearly not spherical. The Milky Way's 'classical' dSph satellites have ellipticities ranging from $0.1\epsilon 0.6$ (Irwin & Hatzidimitriou, 1995). Furthermore, haloes formed in CDM cosmological simulations tend to be triaxial (Allgood et al., 2006; Vera-Ciro et al., 2011). Therefore, insofar as CDM represents the null hypothesis regarding cosmological structure formation, the relevance of inferences drawn from spherically-symmetric analyses depends critically on their robustness to axisymmetric and triaxial cases.

Here we test the slope measurements of WP11 for robustness against non-spherical symmetry. We exploit the fact that in a triaxial potential, the energy is an integral of the motion and thus we can construct isotropic stellar distribution functions (DF) of the form $f(E)$ even within triaxial N-body dark matter haloes. We use the prescription presented by Laporte et al. (2013) to build stellar DFs with various degrees of concentration within cosmological CDM haloes produced in the Aquarius (Springel et al., 2008) and Phoenix (Gao et al., 2012) runs to cover a wide range of triaxiality parameters from Milky Way to cluster type environments. Section 2 discusses the numerical simulations and method used to generate DFs. Section 3 describes our use of samples from these DFs (projected along various lines of sight) to examine systematic errors inherent to the WP11 method for various forms of the tracer number density profiles. We discuss results and conclude in section 4.

7.2 Numerical Methods

7.2.1 Dark matter haloes

For the modelling of dSph dark matter haloes, we use the Aquarius simulations (see Springel et al. (2008) for details). This is a set of six high-resolution dark matter only simulations of the formation of Milky Way mass dark matter haloes in ΛCDM. In the level-2 resolution the particle mass is $\sim 10^4 \mathrm{M}_\odot$ and the softening length is $\epsilon = 65$ pc comoving. We extract a number of dark matter haloes in the mass range $10^9 - 10^{10} h^{-1} \mathrm{M}_\odot$, where $h = 0.73$, using the subhalo finder SUBFIND (Springel et al., 2001). The shape of the Aquarius subhaloes have axis ratios which increase with radius and which are mildly triaxial with axis ratios $< b/a > \sim 0.75$ and $< c/a > \sim 0.6$ at 1 kpc (Vera-Ciro private communication). We also complement our sample with subhaloes drawn from cluster simulations (Gao et al., 2012) to bracket the range of possible triaxiality parameters for subhaloes in CDM and rescaled masses by a factor of 1000.

7.2.2 Generating Tracers

The weighting scheme used here was developed by Laporte et al. (2013) and is a generalisation of that of Bullock & Johnston (2005) to triaxial systems. For details see Laporte et al. (2013) In short, in order to generate a luminous stellar profile, we take each simulation particles of energy $E = \frac{1}{2}v^2 + \Phi$ to simultaneously represent dark matter and stars in diferent amounts through the weight function $\omega(E) = \frac{N_*(E)}{N(E)} = \frac{f_*(E)g(E)}{f(E)g(E)}$, where N is the differential energy distribution, g is the density of states and asterisks denote stellar quantities. One generates $f_*(E)$ through specifying the target number density profile $\nu = \nu(r)$ and using the Eddington formula with an additional approximation to deal with the multivalued behaviour of $\Phi = \Phi(r)$ with spherical radius. In this way, the method creates a stellar profile which retains contours of the flattening of the total potential.

Figure 1 displays projected number densities and line of sight velocity dispersion profiles obtained by sampling random projections of DFs (for two different stellar number density profiles and different concentrations) calculated using the machinery described above. We check for equilibrium by tracking the stellar DFs forward in time for a period of 150 Myr, during which the stellar density profiles remain stable.

WP11 originally tested their method using models in which stellar populations trace dark matter potentials characterised by generalised Hernquist (1990, see also Zhao 1996) profiles:

$$\nu_*(r) = \nu_0 \left(\frac{r}{R_e}\right)^{-\gamma_*} \left[1 + \left(\frac{r}{R_e}\right)^{\alpha_*}\right]^{(\gamma_* - \beta_*)/\alpha_*} \tag{7.1}$$

and

$$\rho_{dm}(r) = \rho_0 \left(\frac{r}{r_{dm}}\right)^{-\gamma_{dm}} \left[1 + \left(\frac{r}{r_{dm}}\right)^{\alpha_{dm}}\right]^{(\gamma_{dm} - \beta_{dm})/\alpha_{dm}} . \tag{7.2}$$

For the stellar number densities, WP11 considered Plummer profiles, $(\alpha_*, \beta_*, \gamma_*) = (2, 5, 0)$, which provide good fits to dSph surface brightness profiles (Irwin & Hatzidimitriou, 1995; McConnachie & Irwin, 2006) and has the virtue of depending on a single parameter, the projected halflight radius R_e. They also considered alternative profiles that retain a luminous core ($\gamma_* = 0$) but fall off more slowly/quickly at large radius than do Plummer profiles[1], with $(\alpha_*, \beta_*, \gamma_*) = (2, 4, 0)$ and $(2, 6, 0)$, respectively. Strigari et al. (2010) have shown that cuspy tracer number density profiles provide a good match to the observed surface brightness and velocity dispersion profiles of the composite stellar populations in dSphs. At a fixed half-light radius, a cuspy tracer component would have a lower velocity dispersion than would its cored counterpart. In order to test for sensitivity to the inner profile of the tracer components, here we consider models with stellar cusps $(\alpha_*, \beta_*, \gamma_*) = (4, 4.5, 1)$ as well as cored Plummer profiles with $(2, 5, 0)$.

7.3 Mass modelling: multi-component method

The presence of multiple stellar populations in some dSphs enables the observer to estimate enclosed masses at two different half-light radii in the same potential. Testing their method on DFs drawn from spherically-symmetric models with cored light profiles, WP11 find that masses tend to be over-estimated more strongly for more-concentrated stellar populations. As a result, the slope Γ tends to be underestimated, providing conservative lower limits on the true slope. We now use our models $f_*(E)$ to test whether this behavior holds for the case of triaxial haloes and/or when the tracer number density profiles are cusped instead of cored.

7.3.1 The bias in the WP mass-estimator: systematics

After calculating DFs as described above, we project each model along 100 random lines of sight uniformly sampled on a sphere. For each projection angle, we then calculate the

---

[1] They actually considered models with $\gamma_* = 0.1$ because models $\gamma = 0$ have $f(E) < 0$ in some regions. In the simulations the resolution limit already prevents this from happening for our models.

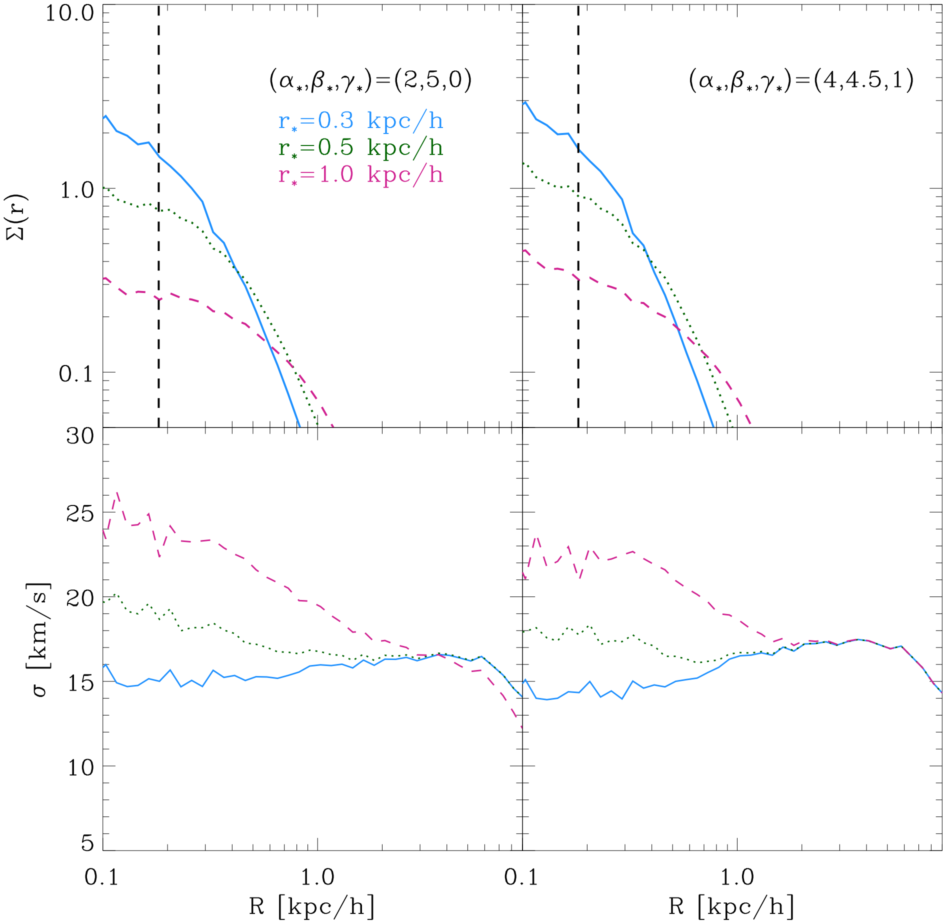

Figure 7.1: Projected number density and line of sigh velocity dispersion profiles for one Aquarius subhalo using the present weighting scheme. *Top left:* Plummer profiles with $r* = 0.3, 0.5, 1.0h^{-1}$kpc, Top right: $(\alpha_*, \beta_*, \gamma_*) = (4, 4.5, 1)$ profiles with $r_* = 0.3, 0.5, 1.0h^{-1}$kpc. The vertical dotted line marks the point where $r = 2.8\epsilon$.

half-light radius R_e of each population. In order to mimic the WP11 method, we estimate R_e by χ^2-fitting a Plummer profile to the tracers. The mass enclosed within R_e is then

$$M(R_e) \propto R_e \frac{\Sigma_{i=0}^{N} w_i (v_i - \bar{v})^2}{\Sigma_{i=0}^{N} w_i} \propto R_e \sigma^2, \tag{7.3}$$

where w_i are the N-body particle weights, and σ is the global velocity dispersion of the tracers. The slope is then calculated as $\Gamma = \frac{log(M_1/M_2)}{log(r_1/r_2)}$.

In order to check whether the WP11 method continues to give conservative limits, Figure 2 displays distributions of the bias $E[\Gamma] = \Gamma_{est} - \Gamma_{true}$ over all randomly-chosen viewing angles. In nearly all cases the estimated slope is smaller than the true slope, such that the estimated slopes continue to represent conservative lower limits. This behavior holds regardless of the degree of triaxiality and/or whether the light profile is cusped or cored.

We emphasise that the velocity dispersion that enters the WP11 mass estimator, $M \propto R_e \sigma^2$ refers to the global dispersion of all stars in a given stellar sub-population. Recently, Kowalczyk et al. (2013, 'K12' hereafter) have found that use of a different mass estimator - one that refers to the velocity dispersion only of stars inside the half-light radius - would give less reliable limits on Γ, particularly when triaxiality is present. We confirm this result using our own DFs (Figure 3): indeed, when velocity dispersions are estimated using only stars inside R_e of their respective subpopulation, the estimated slopes have large scatter about the true values and do not constitute reliable lower limits.

In addition to stellar number densities used in studying dwarf spheroidals, we also show results from additional tests for which we adopted the Jaffe profile, $(\alpha_*, \beta_*, \gamma_*) = (2, 0, 2)$, which can be used to model ellipticals and which has steep stellar cusp ($\gamma_* = 2$). In this case, we determine the half-light radius by fitting a de Vaucouleurs profile. For these cases with steep stellar cusps, we find that that WP11's method becomes unreliable when the stellar populations are highly concentrated (top panel in Fig. 2); however, for sufficiently extended stellar populations the method still recovers a conservative (i.e., biased towards low values) estimate of the slope of the underlying mass profile, albeit with a more prominent tail towards positive values.

7.3.2 Why triaxality does not matter so much?

We can understand the relative insensitivity of the WP11 method to triaxiality by considering the coupling of estimated quantities R_e and σ with respect to projection angle. Let us rotate an individual halo in the frame of its body axes (as evaluated at a radius of $1h^{-1}$kpc) such that the major axis lies on the x-axis and the minor axis lies on the y-axis. We then observe it along different polar angles in the $x-y$ plane and estimate the half-light radius and velocity dispersion via the same χ^2 fitting procedure used above. We notice that when the velocity dispersion is large (along the major axis) the estimated value of R_e is at its minimum value and vice versa (Figure 4). This anti-correlation of R_e and σ tends to cancel the effects of triaxiality on the mass estimator. Therefore the slope Γ will be less sensitive because at a fixed angle θ any bias in $M(R_e)$ will cancel out in the estimate of

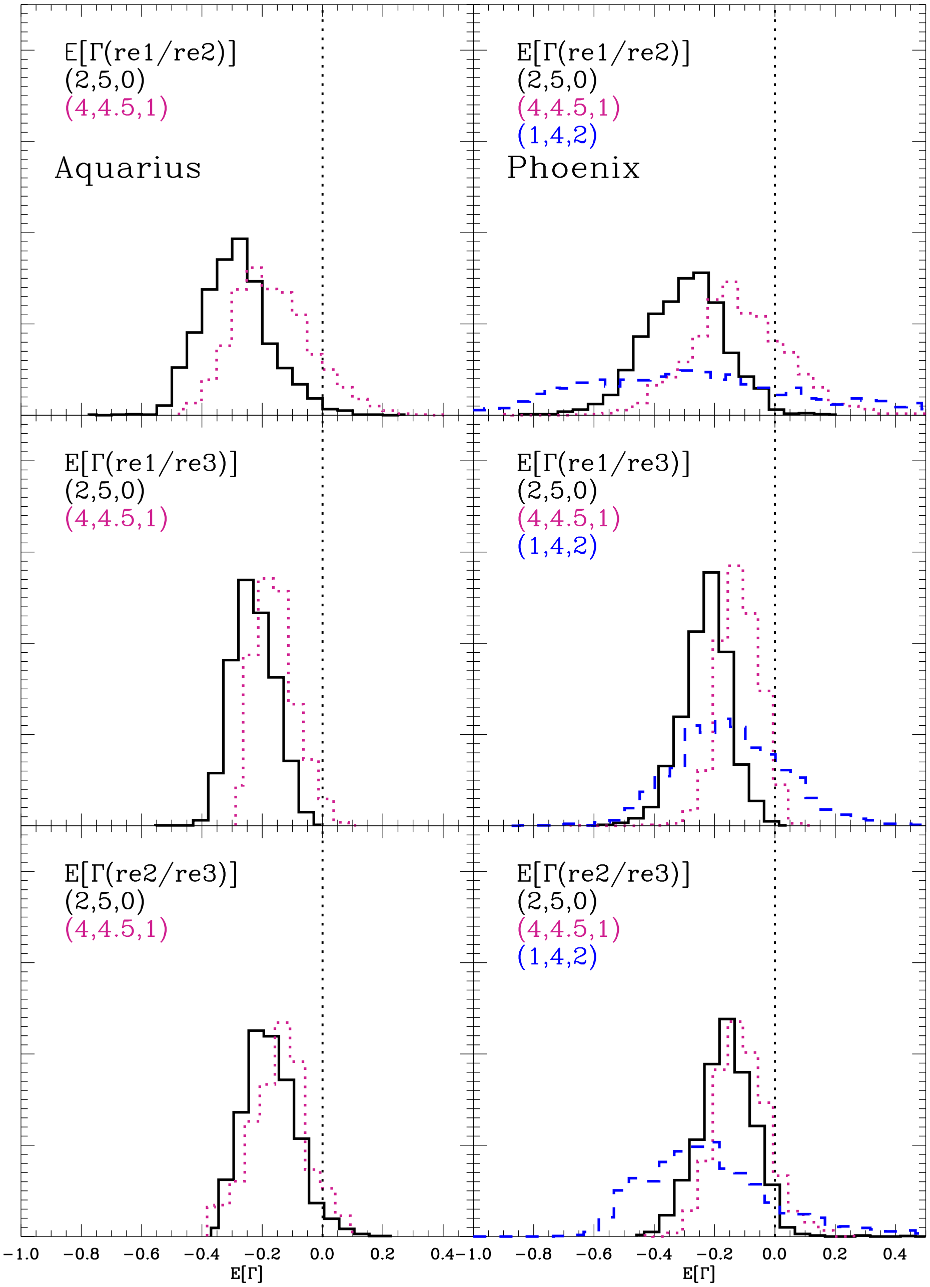

Figure 7.2: The stacked bias distribution in the slope determination of live N-body dark matter haloes (all observed through 100 different random lines of sights). The vertical line marks the point where $\Gamma_{est} - \Gamma_{true}$ is zero. *Left hand:* Results for Aquarius subhaloes for Plummer and $(4, 4.5, 1)$ profiles (in black and dotted magenta respectively) *Right Hand:*: Phoenix rescaled subhaloes for Plummer, $(4, 4.5, 1)$ and Jaffe profiles (in black, dotted magenta and dashed blue respectively). The half-light radii of the stellar populations are determined through fitting a Plummer profile to the number density profile (as assumed in WP11). $(r_{e1}, r_{e2}, r_{e3}) = (0.3, 0.5, 1.0)h^{-1}kpc$.

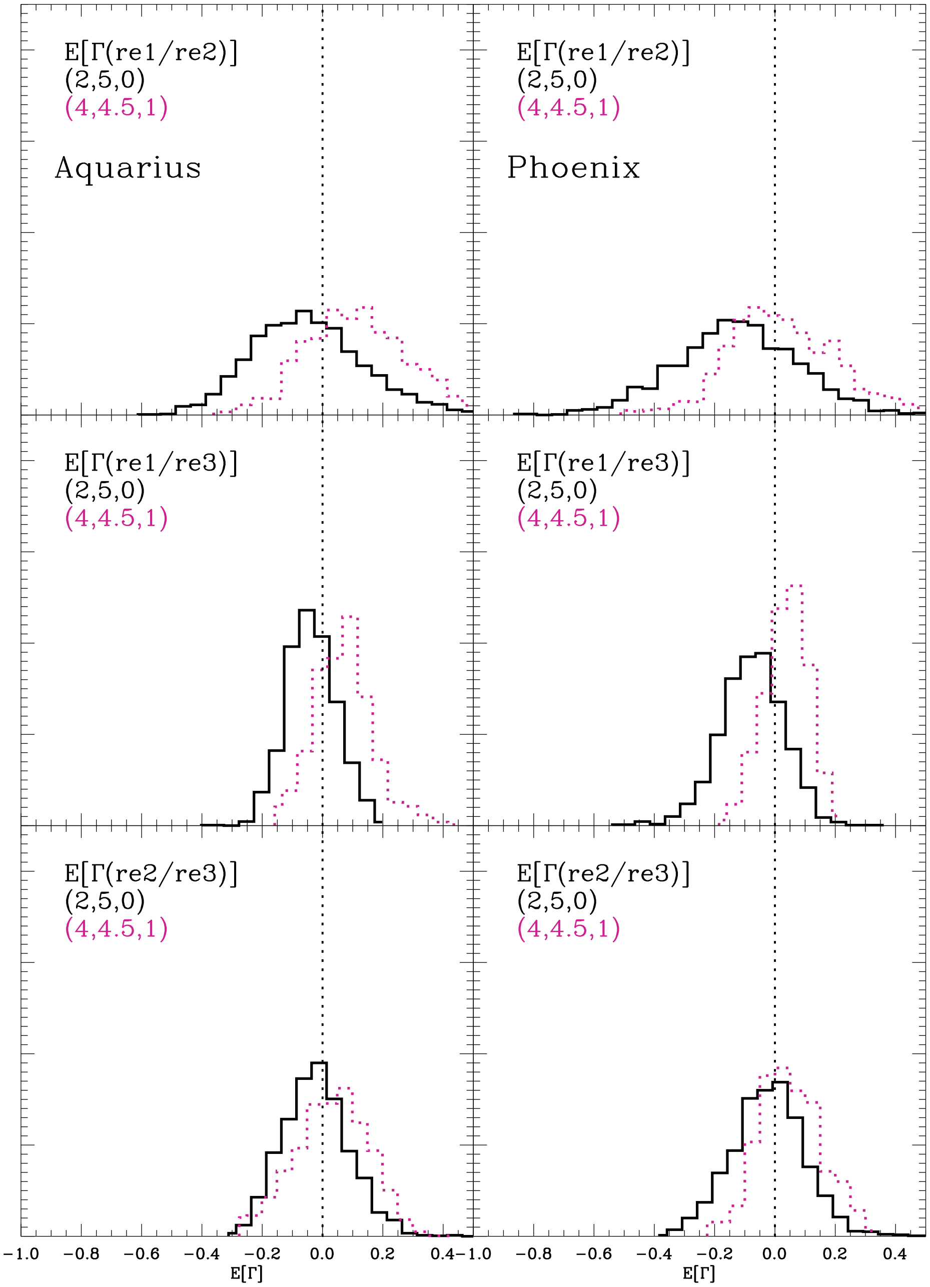

Figure 7.3: Same as figure 2 but showing results derived using the method used in Kowalczyk et al. 2012. Clearly losing the kinematic information outside the half-light radius of the tracer makes the estimator highly unreliable. This method is not that used in WP11.

Γ. This is why the biases we recover in Figure 2 are similar to those found by WP11 for spherically symmetric models. The fluctuations in the mass estimates due to triaxiality vary from 10 to 20 percent depending on the embededness of the tracer population.

7.4 Discussion and conclusions

We have presented families of isotropic distribution functions of the form $f(E)$ in triaxial potentials extracted from dark-matter-only simulations. These span a range of dark matter density profiles for which we have tested the method of Walker & Peñarrubia (2011). Our tests show that the method is generally able to place conservative limits on slopes of mass profiles, even when the light profiles have NFW-like cusps as advocated by Strigari et al. (2010). Thus, we conclude that triaxiality has little impact on published analyses of dSph stellar kinematics that assume spherical symmetry. The reason is that R_e and σ are anti-correlated over the range of projection angles, effectively cancelling the effects of triaxiality. However, we have found that the WP11 method can break down if the stellar tracers are highly concentrated and have steeply cusped number density profiles, e.g., the Jaffe profiles examined in Section 3.1. Some of the haloes which were identified by SUBFIND are strongly stripped and the tracer may not be entirely in equilibrium. However, using those models, we were still able to recover successful limits on the slope of the dark matter density profiles. This suggests that tidal stripping does not unduly impact the results of WP11.

Recently, a similar study on the same subject has been carried out by K12. Our work differs in three aspects:

1. We consider haloes which form within a ΛCDM cosmological context. K12 have considered spherical models which get tidally stirred under a static potential.

2. Our models do not have rotation. Many galaxies in K12 still retain rotation, which is not observed in dSphs.

3. K12 do not test the robustness of WP11 to triaxality, but show that a mass estimator based on the velocity dispersion within the half-light radius of a tracer can misinterpret the true value of the slope of the total mass profile. We confirm their result in Figure 3.

Finally, we note that given a density profile, there exists many possible velocity dispersion profiles which may be consistent with the observed data (allowing for anisotropy). However, WP11 showed this is not an issue for their method under anisotropic Ossipkov-Merritt models but also those with constant anisotropy. Combined with the results of our current study, the WP11 method seems to be robust to both anisotropy and halo triaxiality.

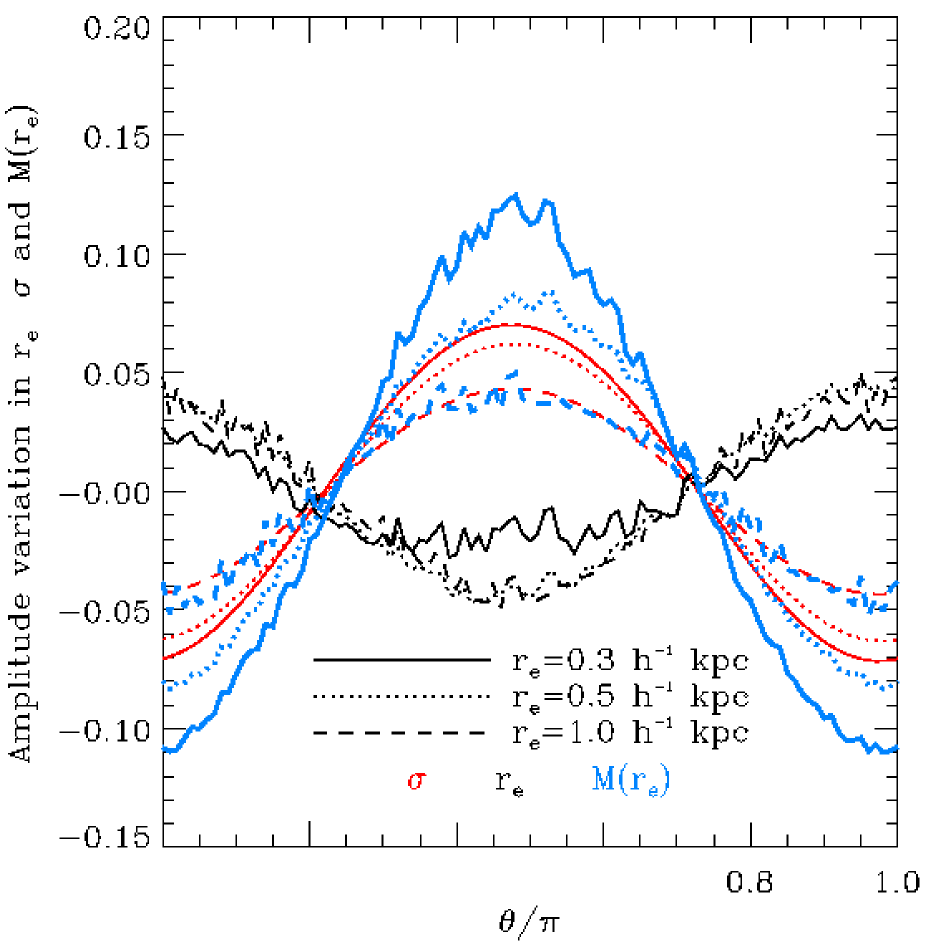

Figure 7.4: Amplitude of the variations in R_e (black), σ (red) and $M(r_e)$ (blue) for different stellar populations (different line styles) for an example halo from Aquarius as a function of angle θ, the polar angle in the plane of the major and minor axes of the halo evaluated at $1h^{-1}$kpc. The anti-correlation in the behaviour of R_e and σ creates almost a cancellation and weak variations in $M(R_e)$. We also see that variations are greater the more embedded the stellar system similarly to the mass bias observed in WP11. This in turn explains why the slopes estimates are still reliable under our $f(E)$ models in triaxial potentials.

Bibliography

Agnello A., Evans N. W., 2012, ApJL, 754, L39

Allgood B., Flores R. A., Primack J. R., Kravtsov A. V., Wechsler R. H., Faltenbacher A., Bullock J. S., 2006, MNRAS, 367, 1781

Amorisco N. C., Evans N. W., 2011, MNRAS, 411, 2118

Angulo R. E., Springel V., White S. D. M., Jenkins A., Baugh C. M., Frenk C. S., 2012, MNRAS, 426, 2046

Barnes J., Hut P., 1986, Nature, 324, 446

Barnes J. E., 2012, MNRAS, 425, 1104

Battaglia G., Helmi A., Tolstoy E., Irwin M., Hill V., Jablonka P., 2008, ApJL, 681, L13

Battaglia G., Tolstoy E., Helmi A., Irwin M., Parisi P., Hill V., Jablonka P., 2011, MNRAS, 411, 1013

Behroozi P. S., Conroy C., Wechsler R. H., 2010, ApJ, 717, 379

Behroozi P. S., Wechsler R. H., Conroy C., 2013, ApJ, 770, 57

Bennert V. N., Auger M. W., Treu T., Woo J.-H., Malkan M. A., 2011, ApJ, 742, 107

Bernardi M., 2009, MNRAS, 395, 1491

Bernardi M., Hyde J. B., Sheth R. K., Miller C. J., Nichol R. C., 2007, AJ, 133, 1741

Bezanson R., van Dokkum P. G., Tal T., Marchesini D., Kriek M., Franx M., Coppi P., 2009, ApJ, 697, 1290

Blumenthal G. R., Faber S. M., Flores R., Primack J. R., 1986, ApJ, 301, 27

Boylan-Kolchin M., Ma C.-P., Quataert E., 2004, ApJL, 613, L37

Boylan-Kolchin M., Springel V., White S. D. M., Jenkins A., Lemson G., 2009, MNRAS, 398, 1150

Breddels M. A., Helmi A., van den Bosch R. C. E., van de Ven G., Battaglia G., 2012, ArXiv e-prints

Brough S., Tran K.-V., Sharp R. G., von der Linden A., Couch W. J., 2011, MNRAS, 414, L80

Bullock J. S., Johnston K. V., 2005, ApJ, 635, 931

Collins C. A., Stott J. P., Hilton M., Kay S. T., Stanford S. A., Davidson M., Hosmer M., Hoyle B., Liddle A., Lloyd-Davies E., Mann R. G., Mehrtens N., Miller C. J., Nichol R. C., Romer A. K., Sahlén M., Viana P. T. P., West M. J., 2009, Nature, 458, 603

Croton D. J., Springel V., White S. D. M., De Lucia G., Frenk C. S., Gao L., Jenkins A., Kauffmann G., Navarro J. F., Yoshida N., 2006, MNRAS, 365, 11

Daddi E., Renzini A., Pirzkal N., Cimatti A., Malhotra S., Stiavelli M., Xu C., Pasquali A., Rhoads J. E., Brusa M., di Serego Alighieri S., Ferguson H. C., Koekemoer A. M., Moustakas L. A., Panagia N., Windhorst R. A., 2005, ApJ, 626, 680

Davis M., Efstathiou G., Frenk C. S., White S. D. M., 1985, ApJ, 292, 371

De Lucia G., Blaizot J., 2007, MNRAS, 375, 2

Diemand J., Kuhlen M., Madau P., 2007, ApJ, 657, 262

Dubinski J., 1998, ApJ, 502, 141

Dubois Y., Pichon C., Devriendt J., Silk J., Haehnelt M., Kimm T., Slyz A., 2013, MNRAS, 428, 2885

Duffy A. R., Schaye J., Kay S. T., Dalla Vecchia C., Battye R. A., Booth C. M., 2010, MNRAS, 405, 2161

Edwards L. O. V., Patton D. R., 2012, MNRAS, 425, 287

Efstathiou G., Davis M., White S. D. M., Frenk C. S., 1985, ApJS, 57, 241

El-Zant A. A., Hoffman Y., Primack J., Combes F., Shlosman I., 2004, ApJL, 607, L75

Faber S. M., Jackson R. E., 1976, ApJ, 204, 668

Fabian A. C., 1994, ARAA, 32, 277

Fabian A. C., Mushotzky R. F., Nulsen P. E. J., Peterson J. R., 2001, MNRAS, 321, L20

Feldmann R., Carollo C. M., Mayer L., 2011, ApJ, 736, 88

Gao L., Frenk C. S., Jenkins A., Springel V., White S. D. M., 2012, MNRAS, 419, 1721

Gao L., Loeb A., Peebles P. J. E., White S. D. M., Jenkins A., 2004, ApJ, 614, 17

Gao L., Navarro J. F., Frenk C. S., Jenkins A., Springel V., White S. D. M., 2012, MNRAS, 425, 2169

Gnedin O. Y., Ceverino D., Gnedin N. Y., Klypin A. A., Kravtsov A. V., Levine R., Nagai D., Yepes G., 2011, ArXiv e-prints, 1108.5736

Gnedin O. Y., Kravtsov A. V., Klypin A. A., Nagai D., 2004, ApJ, 616, 16

Gonzalez A. H., Zabludoff A. I., Zaritsky D., 2005, ApJ, 618, 195

Guo Q., White S., Li C., Boylan-Kolchin M., 2010, MNRAS, 404, 1111

Hausman M. A., Ostriker J. P., 1978, ApJ, 224, 320

Hayashi K., Chiba M., 2012, ApJ, 755, 145

Hernquist L., 1990, ApJ, 356, 359

Hernquist L., Bouchet F. R., Suto Y., 1991, ApJS, 75, 231

Hilz M., Naab T., Ostriker J. P., 2013, MNRAS, 429, 2924

Hilz M., Naab T., Ostriker J. P., Thomas J., Burkert A., Jesseit R., 2012, MNRAS, 425, 3119

Huchra J., Davis M., Latham D., Tonry J., 1983, ApJS, 52, 89

Hyde J. B., Bernardi M., 2009, MNRAS, 394, 1978

Irwin M., Hatzidimitriou D., 1995, MNRAS, 277, 1354

Jardel J. R., Gebhardt K., 2012, ApJ, 746, 89

Johansson P. H., Naab T., Ostriker J. P., 2009, ApJL, 697, L38

Kazantzidis S., Magorrian J., Moore B., 2004, ApJ, 601, 37

Khochfar S., Silk J., 2006, MNRAS, 370, 902

Koch A., Wilkinson M. I., Kleyna J. T., Gilmore G. F., Grebel E. K., Mackey A. D., Evans N. W., Wyse R. F. G., 2007, ApJ, 657, 241

Kolb E. W., Turner M. S., 1990, The early universe.

Kormendy J., 1977, ApJ, 218, 333

Kowalczyk K., okas E. L., Kazantzidis S., Mayer L., 2013, MNRAS, 431, 2796

Kravtsov A. V., Berlind A. A., Wechsler R. H., Klypin A. A., Gottlöber S., Allgood B., Primack J. R., 2004, ApJ, 609, 35

Kuijken K., Dubinski J., 1994, MNRAS, 269, 13

Laporte C. F. P., White S. D. M., Naab T., Gao L., 2013, ArXiv e-prints

Laporte C. F. P., White S. D. M., Naab T., Ruszkowski M., Springel V., 2012, MNRAS, 424, 747

Lauer T. R., Faber S. M., Richstone D., Gebhardt K., Tremaine S., Postman M., Dressler A., Aller M. C., Filippenko A. V., Green R., Ho L. C., Kormendy J., Magorrian J., Pinkney J., 2007, ApJ, 662, 808

Lewis A., Challinor A., Lasenby A., 2000, ApJ, 538, 473

Liddle A. R., Lyth D. H., 2000, Cosmological Inflation and Large-Scale Structure

Lidman C., Suherli J., Muzzin A., Wilson G., Demarco R., Brough S., Rettura A., Cox J., DeGroot A., Yee H. K. C., Gilbank D., Hoekstra H., Balogh M., Ellingson E., Hicks A., Nantais J., Noble A., Lacy M., Surace J., Webb T., 2012, MNRAS, 427, 550

Liu F. S., Mao S., Deng Z. G., Xia X. Y., Wen Z. L., 2009, MNRAS, 396, 2003

Loeb A., Peebles P. J. E., 2003, ApJ, 589, 29

okas E. L., Mamon G. A., 2001, MNRAS, 321, 155

Ma C.-P., Bertschinger E., 1995, ApJ, 455, 7

Maraston C., 2005, MNRAS, 362, 799

Martinez-Manso J., Guzman R., Barro G., Cenarro J., Perez-Gonzalez P., Sanchez-Blazquez P., Trujillo I., Balcells M., Cardiel N., Gallego J., Hempel A., Prieto M., 2011, ApJL, 738, L22

Martizzi D., Teyssier R., Moore B., Wentz T., 2012, MNRAS, 422, 3081

Mateo M. L., 1998, ARAA, 36, 435

McConnachie A. W., Irwin M. J., 2006, MNRAS, 365, 1263

McNamara B. R., Wise M., Nulsen P. E. J., David L. P., Sarazin C. L., Bautz M., Markevitch M., Vikhlinin A., Forman W. R., Jones C., Harris D. E., 2000, ApJL, 534, L135

McWilliams S. T., Ostriker J. P., Pretorius F., 2012, ArXiv e-prints

Merritt D., 2006, ApJ, 648, 976

Merritt D., Milosavljević M., Favata M., Hughes S. A., Holz D. E., 2004, ApJL, 607, L9

Mikkola S., Valtonen M. J., 1990, ApJ, 348, 412

Moster B. P., Naab T., White S. D. M., 2013, MNRAS, 428, 3121

Moster B. P., Somerville R. S., Maulbetsch C., van den Bosch F. C., Macciò A. V., Naab T., Oser L., 2010, ApJ, 710, 903

Mukhanov V., 2005, Physical Foundations of Cosmology

Muzzin A., Marchesini D., Stefanon M., Franx M., McCracken H. J., Milvang-Jensen B., Dunlop J. S., Fynbo J. P. U., Brammer G., Labbé I., van Dokkum P. G., 2013, ApJ, 777, 18

Naab T., Johansson P. H., Ostriker J. P., 2009, ApJL, 699, L178

Natarajan P., Hjorth J., van Kampen E., 1997, MNRAS, 286, 329

Navarro J. F., Eke V. R., Frenk C. S., 1996, MNRAS, 283, L72

Navarro J. F., Frenk C. S., White S. D. M., 1997, ApJ, 490, 493

Navarro J. F., Ludlow A., Springel V., Wang J., Vogelsberger M., White S. D. M., Jenkins A., Frenk C. S., Helmi A., 2010, MNRAS, 402, 21

Navarro J. F., White S. D. M., 1994, MNRAS, 267, 401

Newman A. B., Ellis R. S., Bundy K., Treu T., 2012, ApJ, 746, 162

Newman A. B., Treu T., Ellis R. S., Sand D. J., 2011, ApJL, 728, L39

Newman A. B., Treu T., Ellis R. S., Sand D. J., 2013a, ApJ, 765, 25

Newman A. B., Treu T., Ellis R. S., Sand D. J., Nipoti C., Richard J., Jullo E., 2013b, ApJ, 765, 24

Newman A. B., Treu T., Ellis R. S., Sand D. J., Richard J., Marshall P. J., Capak P., Miyazaki S., 2009, ApJ, 706, 1078

Nipoti C., Treu T., Bolton A. S., 2009, ApJ, 703, 1531

Nipoti C., Treu T., Ciotti L., Stiavelli M., 2004, MNRAS, 355, 1119

Oser L., Naab T., Ostriker J. P., Johansson P. H., 2012a, ApJ, 744, 63

Oser L., Naab T., Ostriker J. P., Johansson P. H., 2012b, ApJ, 744, 63

Oser L., Ostriker J. P., Naab T., Johansson P. H., Burkert A., 2010, ApJ, 725, 2312

Ostriker J. P., Hausman M. A., 1977, ApJL, 217, L125

Ostriker J. P., Tremaine S. D., 1975, ApJL, 202, L113

Paranjape A., Sheth R. K., 2012, MNRAS, p. 2994

Patel S. G., van Dokkum P. G., Franx M., Quadri R. F., Muzzin A., Marchesini D., Williams R. J., Holden B. P., Stefanon M., 2013, ApJ, 766, 15

Peacock J. A., Cole S., Norberg P., Baugh C. M., Bland-Hawthorn J., Bridges T., Cannon R. D., Colless M., Collins C., Couch W., Dalton G., Deeley K., De Propris R., Driver S. P., Efstathiou G. e., 2001, Nature, 410, 169

Planck Collaboration Ade P. A. R., Aghanim N., Armitage-Caplan C., Arnaud M., Ashdown M., Atrio-Barandela F., Aumont J., Baccigalupi C., Banday A. J., et al. 2013, ArXiv e-prints

Pontzen A., Governato F., 2012, MNRAS, 421, 3464

Pontzen A., Governato F., 2013, MNRAS, 430, 121

Postman M., Lauer T. R., Donahue M., Graves G., Coe D., Moustakas J., Koekemoer A., Bradley L., Ford H. C., Grillo C., Zitrin A., Lemze D., Broadhurst T., Moustakas L., Ascaso B., Medezinski E., Kelson D., 2012, ApJ, 756, 159

Puchwein E., Springel V., Sijacki D., Dolag K., 2010, MNRAS, 406, 936

Rubin V. C., Ford Jr. W. K., 1970, ApJ, 159, 379

Rudick C. S., Mihos J. C., McBride C., 2006, ApJ, 648, 936

Rudick C. S., Mihos J. C., McBride C. K., 2011, ApJ, 732, 48

Ruszkowski M., Springel V., 2009, ApJ, 696, 1094

Sand D. J., Treu T., Ellis R. S., 2002, ApJL, 574, L129

Sand D. J., Treu T., Ellis R. S., Smith G. P., Kneib J., 2008, ApJ, 674, 711

Sand D. J., Treu T., Smith G. P., Ellis R. S., 2004, ApJ, 604, 88

Seljak U., Zaldarriaga M., 1996, ApJ, 469, 437

Shankar F., Marulli F., Bernardi M., Mei S., Meert A., Vikram V., 2011, ArXiv e-prints

Shen S., Mo H. J., White S. D. M., Blanton M. R., Kauffmann G., Voges W., Brinkmann J., Csabai I., 2003, MNRAS, 343, 978

Sijacki D., Springel V., 2006, MNRAS, 366, 397

Smoot G. F., Bennett C. L., Kogut A., Wright E. L., Aymon J., Boggess N. W., Cheng E. S., de Amici G., Gulkis S., Hauser M. G., Hinshaw G., Jackson P. D., Janssen M., Kaita E., Kelsall T., Keegstra P. a., 1992, ApJL, 396, L1

Sommer-Larsen J., Limousin M., 2010, MNRAS, 408, 1998

Springel V., 2005, MNRAS, 364, 1105

Springel V., Wang J., Vogelsberger M., Ludlow A., Jenkins A., Helmi A., Navarro J. F., Frenk C. S., White S. D. M., 2008, MNRAS, 391, 1685

Springel V., White S. D. M., Jenkins A., Frenk C. S., Yoshida N., Gao L., Navarro J., Thacker R., Croton D., Helly J., Peacock J. A., Cole S., Thomas P., Couchman H., Evrard A., Colberg J., Pearce F., 2005, Nature, 435, 629

Springel V., White S. D. M., Tormen G., Kauffmann G., 2001, MNRAS, 328, 726

Stott J. P., Collins C. A., Burke C., Hamilton-Morris V., Smith G. P., 2011, MNRAS, 414, 445

Strigari L. E., Bullock J. S., Kaplinghat M., Kravtsov A. V., Gnedin O. Y., Abazajian K., Klypin A. A., 2006, ApJ, 652, 306

Strigari L. E., Frenk C. S., White S. D. M., 2010, MNRAS, 408, 2364

Strigari L. E., Koushiappas S. M., Bullock J. S., Kaplinghat M., Simon J. D., Geha M., Willman B., 2008, ApJ, 678, 614

Syer D., White S. D. M., 1998, MNRAS, 293, 337

Szomoru D., Franx M., van Dokkum P. G., 2012, ApJ, 749, 121

Tolstoy E., Irwin M. J., Helmi A., Battaglia G., Jablonka P., Hill V., Venn K. A., Shetrone M. D., Letarte B., Cole A. A., Primas F., Francois P., Arimoto N., Sadakane K., Kaufer A., Szeifert T., Abel T., 2004, ApJL, 617, L119

Tonini C., Bernyk M., Croton D., Maraston C., Thomas D., 2012, ApJ, 759, 43

Trujillo I., Conselice C. J., Bundy K., Cooper M. C., Eisenhardt P., Ellis R. S., 2007, MNRAS, 382, 109

Vale A., Ostriker J. P., 2004, MNRAS, 353, 189

van Dokkum P. G., Franx M., Kriek M., Holden B., Illingworth G. D., Magee D., Bouwens R., Marchesini D., Quadri R., Rudnick G., Taylor E. N., Toft S., 2008, ApJL, 677, L5

van Dokkum P. G., Whitaker K. E., Brammer G., Franx M., Kriek M., Labbé I., Marchesini D., Quadri R., Bezanson R., Illingworth G. D., Muzzin A., Rudnick G., Tal T., Wake D., 2010, ApJ, 709, 1018

Vera-Ciro C. A., Sales L. V., Helmi A., Frenk C. S., Navarro J. F., Springel V., Vogelsberger M., White S. D. M., 2011, MNRAS, 416, 1377

von der Linden A., Best P. N., Kauffmann G., White S. D. M., 2007, MNRAS, 379, 867

Wake D. A., Whitaker K. E., Labbé I., van Dokkum P. G., Franx M., Quadri R., Brammer G., Kriek M., Lundgren B. F., Marchesini D., Muzzin A., 2011, ApJ, 728, 46

Walker M. G., Mateo M., Olszewski E. W., Peñarrubia J., Wyn Evans N., Gilmore G., 2009, ApJ, 704, 1274

Walker M. G., Peñarrubia J., 2011, ApJ, 742, 20

White S. D. M., 1976, MNRAS, 174, 19

White S. D. M. in Schaeffer R., Silk J., Spiro M., Zinn-Justin J., eds, 1996, Cosmology and large scale structure

Wilkinson M. I., Kleyna J., Evans N. W., Gilmore G., 2002, MNRAS, 330, 778

Williams R. J., Quadri R. F., Franx M., van Dokkum P., Toft S., Kriek M., Labbé I., 2010, ApJ, 713, 738

Wolf J., Martinez G. D., Bullock J. S., Kaplinghat M., Geha M., Muñoz R. R., Simon J. D., Avedo F. F., 2010, MNRAS, 406, 1220

Zel'dovich Y. B., 1970, AAP, 5, 84

Zhao H., 1996, MNRAS, 278, 488

Zibetti S., White S. D. M., Schneider D. P., Brinkmann J., 2005, MNRAS, 358, 949

Zwicky F., 1933, Helvetica Physica Acta, 6, 110

Zwicky F., 1937, ApJ, 86, 217

Danksagung

Most thanks go to my supervisor Simon White. I have enjoyed and benefitted from your total freedom in carrying my projects. Out of the whole of MPA, I will miss you the most. I found a home in this institute and I hope to come and visit regularly in the future. Thank you for always making time for me to discuss my science with you no matter how busy you were. I enjoyed all the conversations, arguments (no matter how heated these could turn into), discussions and friendly moments. Thank you for letting me go to so many conferences, an East Coast tour in the winter of 2012 and the winter school on galaxy formation in Israel. I was lucky to be able to discuss my work within the VIRGO Consortium and have the opportunity to discuss ideas in a relaxed atmosphere. In this regard, I also thank Carlos Frenk and Julio Navarro who have been fully supportive and interested in my latest projects. I certainly hope to continue some work in this open and friendly scientific environment. I just feel that this thesis is just the beginning of more things to come. There is no better feeling than this and I thank you for this. Merci et à très bientôt.

Second, I would like to thank Thorsten Naab for being supportive with me right from the beginning and throughout the PhD. We still have more things to do in the future! I will miss our Biergarten trips to Garching. Third, I would like to thank Volker Springel because I regained my rusty skills in C-programming through reading his lines of comprehensive code and this helped me write my own stuff. I also thank some of the postdocs who sometimes gave me snipets of useful code (Ben, Laura, Michal). I want to thank Scott Tremaine for pointing me out the fellowship programme in NYC last summer. I would also like to thank him and James Binney for writing the *Galactic Dynamics* book which convinced me to do a PhD in the first place when I was an undergraduate at Cambridge. Thanks to my friends from Cambridge who have been supportive in difficult times: Vasily Belokurov, Matthew Walker, Jorge Peñarrubia, Monica Relaño, John Eldridge and Guy Pooley.

Thank you Maria, Kate, Gabi, Sonja and Cornelia for always being there to help me with my well-being in the office, landlady issues, financial problems or a point of contact to see what Simon is up to when not around at the institute. My thanks also go to many of the MPA staff members with whom I have shared a lot of interesting conversations: Rashid Sunyaev, Marat Gilfanov, Eugene Churazov, Fabian Schmidt, Eiichiro Komatsu, Benedetta Ciardi,Torsten Ensslin, Guinevere Kauffmann. Thanks to the MPA

postdocs: Laura Sales, Simona Vegetti, Andreas Pawlik, Christian Wagner, Raul Angulo, Silvia Bonoli, Bruno Henriques, Ben Moster, Diederik Kruijssen, Thomas Greif, Mark Dijkstra, Robert Smith, Stefan Hilbert, Michal Maciejewski, Steffi Walsch, Chiara Spiniello. Thanks to IMPRS/MPA PhD students: Bhaskar Agarwal, Marcel van Daalen, Jonny Elliott, Alessia Longobardi, Rob Yates, Stefan Rau, Andrew Chung, Ludwig Oser, Karl Simon, Michael Hilz, Katarina Markovic, Francesca Iannuzzi, Silvia Fabello.
I thank Stephan Weiser for taking me as his student. I have learned a great deal about musical improvisation and had many great discussions about the art of listening and creating music of the moment. Most importantly I thank my friends and new acquaintances from Munich and outside astronomy which have helped me find a balance throughout the PhD: Adriano Prestel, Andre Schwager, Sam Dick, Ines, Steffi, Marta, Ferdi and Nanjing, Ning, Felix, Eva, Matthieu, Tom Betsalel, Sebastian, Robin, Tilman, Thomas, Achim, Aron, Stefan Pfeiffer, Ruben, Phairuz, Gregor, Manu, Marco, Anna, Nati and Sandrina. I will miss you all.

Thanks to my close friends from abroad for their support: Marc Smonig, Bianca Argimon, Sabine Crevoisier, Edmund Fokschaner, Georg Lugert, Rani Noakes, Rafael Maldonado, Darryl Walters and Shirin Saedi. Thanks to Laura, Bhaskar and Hannah (who also corrected my horrible German grammar for the Zusammenfassung) who have been there for me during the good and bad times. Et enfin, je remercie mes parents et grands-parents pour leur amour.

Lebenslauf

Chervin Laporte

Geburtsdatum	Geburt in Geburtsort
10 March 1988	Versailles, France
Schulzeit	Besuch der Schule in Ort
1994-2006	European School of Brussels II, Woluwe, Belgium
2006-2010	University of Cambridge, United Kingdom
2010-2014	MPA & LMU, Munich, Germany